Laboratory experiments recreating icy moons' geysers

Thom Verhoeff

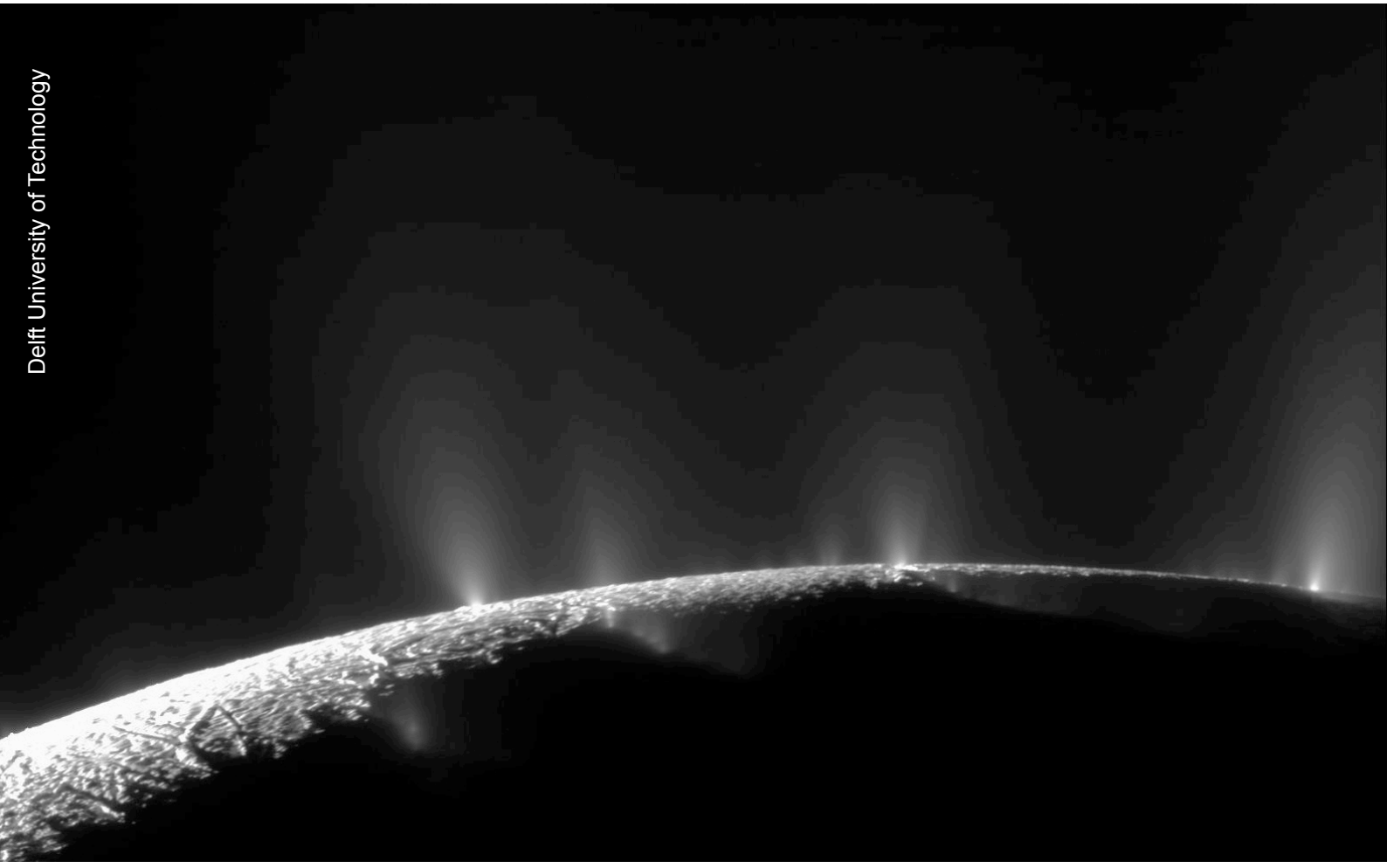

Delft University of Technology

TU Delft

Laboratory experiments recreating icy moons' geysers

by

Thom Verhoeff

to obtain the degree of Master of Science
at the Delft University of Technology,
to be defended publicly on February 16, 2023 at 14:00

Student number:	4627180
Supervisors:	S.M. Cazaux, F.F.J. Schrijer
Assessment committee:	S.M. Cazaux - TU Delft - Chair
	F.F.J. Schrijer - TU Delft - Responsible thesis supervisor
	R.P. Dwight - TU Delft - Examiner
	A. Cervone - TU Delft - Examiner
Institution:	Delft University of Technology
	Faculty of Aerospace Engineering
Duration:	April 2022 - February 2023

Cover Image: Enceladus, bursting at the seams
Credit: NASA/JPL-Caltech/Space Science Institute.
Published February 23, 2010

TU Delft

Preface

With the finalisation of this report also comes the realisation that these are my last days as a Master's student at the TU Delft. I would like to take this opportunity to thank all those who helped me through this challenging period. Starting with my thesis supervisors Stéphanie Cazaux and Ferry Schrijer, for their support and their never-ending enthusiasm for the project. Their advice, given during our bi-weekly meeting of the "plume team", has really helped in taking this project to the next level. I would also like to thank the other members of the plume team, for their contributions and cooperation, and the interesting topics of discussion which sometimes made us leave the meeting more confused than when we started. I'd also like to thank Tara Bründl for her guidance and commitment, Stavros Sklavenitis, my predecessor, for always being helpful and involved even after finishing his studies, and Tomás Fontes, who made the numerical simulations of this project, for the collaboration and helpful discussions. I'm also grateful to Friso Hartog, Wouter van der Sluis and Olaf van Campenhout from Dimple technologies for introducing me to the world of 3D printing and providing most of the models used in this study. The same applies to Eugene Kersjes and Mark Dickin from Ricoh, for providing the 3D printed polypropylene model, for which I am thankful. And last but definitely not least, I'd like to thank my parents, girlfriend Pauline, sister, friends and family for their invaluable support throughout my studies. It has been a long and tough journey, but I can finally say that I can start my career as an Aerospace Engineer.

Thom Verhoeff
Amsterdam, February 2023

Abstract

This study is part of an ongoing research project, which aims to increase the physical understanding of the plume formation on Saturn's icy moon Enceladus. The experimental setup presented in this study is the third iteration of the physical models aiming to recreate the main plume characteristics, where in this study the effects of the channel length, width, type (straight, converging/diverging or diverging), temperature and material are explored and linked to Enceladus' crevasses. This is done by conducting experiments with 7 different models, where the temperature and pressure are measured along the channels. The models are placed on top of a water-filled reservoir, where the reservoir conditions can be controlled to a limited extent by varying the heating power supplied to the reservoir water. The experimental setup is placed in the test section of the *Hypersonic Test Facility Delft (HTFD)*, which functions as a vacuum chamber.

It is shown that the varying geometry of the channel imposes constraints on the maximum expansion angle before flow separation occurs, the sonic point location and the length/width combination in order to achieve a certain vent Mach number and mass flow rate, although this is also decided by the reservoir and ambient conditions. However, besides the physical properties of the model, there is evidence that the flow properties are dominated by the thermal processes occurring inside the setup. Condensation occurs only in the reservoir, releasing latent heat and making the isentropic flow assumption invalid by definition. It is demonstrated that it is likely that the thermal radiation from the test section of the HTFD onto the model is sufficient to thermally choke the flow. It is unlikely that the flows become choked due to the effects of friction alone. Cooling the models by 10-15°C did not result in significant changes in flow properties, and to have noticeable effects on the flow, the models would have to be cooled to much lower temperatures so that condensation occurs in the channel instead of the reservoir. Although the vapor remains unsaturated in the channels, there are signs of local temperature spikes in the expanding sections of the channels, near the vent, when either no or low heating power is supplied to the reservoir water and the pressure in the channel is reduced. This implies that either the temperature at the center of the channel is lower than what could be expected from the temperature measurements and heat is thus released by the deposition of the vapor, or the particles that condensed in the reservoir partially evaporate after the throat of the channel, after which the evaporative cooling freezes the remainder of the particles, with the accompanying latent heat release. It is also not expected that a pressurized reservoir is necessary to create the plumes on Enceladus, nor is the presence of a geometrical throat, due to the combined effects of friction and condensing vapor. The results of one physical model are compared to a computational fluid dynamics model using the same geometry, and the main difference between the physical and numerical model is that the vent pressure of the numerical model is approximately half the vent pressure of the physical model, and the temperature of the numerical model dropped to about -50°C at the expanding section of the channel where the temperature only increased throughout the channel for the physical model. This, and the small heat spike near the vent under low-power conditions, has questioned the accuracy of the temperature measurement method and further research would be required to improve this accuracy.

Contents

Nomenclature

Abbreviations and acronyms

Abbreviation/Acronym	Definition
CAD	Computer-aided Design
CDA	Cosmic Dust Analyzer
CHNOPS	Carbon, Hydrogen, Nitrogen, Oxygen, Phosphorus and Sulfur
FDM	Fused Deposition Modelling
HMOC	High-Mass Organic Cations
HTFD	Hypersonic Test Facility Delft
INMS	Ion and Neutral Mass Spectrometer
ISS	Imaging Science Subsystem
NI	National Instruments
PLA	Polylactic acid
PP	Polypropylene
SLS	Selective Laser Sintering
UVIS	Ultraviolet Imaging Spectrograph
VIMS	Visual and Infrared Mapping Spectrometer

Symbols

Symbol	Definition	Unit
A	(Cross-sectional) area	[m^2]
A^*	Sonic throat area	[m^2]
c_p	Specific heat capacity at constant pressure	[J/kgK]
D	Diameter of the channel	[m]
f	Solid fraction of the mass flow *or*	[-]
	Shear stress coefficient	[-]
f_{max}	Solid fraction required to choke the flow	
H	(total) Enthalpy	[J]
h	Specific enthalpy	[J/kg]
h_{vap}	Enthalphy of vaporization	
I	(Electric) current	[A]
L	Length of the channel	[m]
L^*	Choking point of the channel	
M	Mach number	[-]
$\dot{m}$	Mass flow rate through a channel	[kg/s]
m	Mass	[kg]
P	Pressure	[Pa] or [bar]

Symbol	Definition	Unit
P_0	Pressure at stagnation point	
P_0^*	Stagnation pressure at choking point	
P_{diff}	Differential pressure	
$P_{diff,max}$	Maximum operating differential pressure	
$P_{eq}^{(s.g.)}$	Saturated vapor pressure (for solid-gas equilibrium, l.g. for liquid-gas)	
P_{res}	Reservoir pressure	
$\mathcal{P}$	(Electric) power	[W]
q	Specific heat addition	[J/kg]
q_{max}	Critical specific heat addition	
q_{vac}	Heat radiated from vacuum chamber walls	
R	(Electric) resistance *or*	[Ω]
	Gas constant	[J/kgK]
s	(Super-)saturation degree	[-]
T	Temperature	[K]
T_0	Temperature at stagnation point	
T_0^*	Stagnation temperature at choking point	
T_{noise}	Thermocouple noise	
T_{off}	Thermocouple offset	
T_{res}	Reservoir temperature	
U	Total internal energy *or*	[J]
	Voltage	[V]
$U_{chamber}$	Vacuum chamber voltage	
U_{ideal}	Reference or calibration voltage	
U_{max}	Maximum voltage	
U_{off}	Voltage offset	
U_{out}	Voltage output	
U_{real}	Measured or actual voltage	
U_{supply}	Voltage output of the power supply	
V	Velocity	[m/s]
V^*	Velocity at choking point	
γ	Specific heat ratio	[-]
ϵ	Mean height of roughness in a channel (or absolute roughness)	[mm]
ν	Specific volume	[m^3/kg]
ρ	Density	[kg/m^3]
σ	Stefan-Boltzmann constant	[W/m^2K^4]

List of Figures

List of Tables

1

Introduction

Back in 1997, the Cassini-Huygens mission was launched by NASA. The primary mission of the Cassini spacecraft was to gather information about Saturn, its rings, moons and magnetic environments. In 2005, the data acquired by Cassini's magnetometer made scientists want to take a closer look at Enceladus with a targeted fly-by [1], because the disturbed magnetic field could indicate the presence of a sub-surface ocean [2]. Enceladus is a small, icy moon of Saturn, with a diameter of only about 500 km. The disturbed magnetic field is caused by the plumes emanating from Enceladus' south pole, and Cassini's mass spectrometers observed salty and organic particles in these plumes. The plumes are ejected into space with velocities of around 350-950 m/s, and even up to 1.25 km/s [3, 4]. During the many flybys that followed, Cassini's instruments analyzed Enceladus' plumes, the radiative environment, surface temperatures and structures, and much more. Until this day, it is not yet certain which mechanism drives the plumes and how the observed plume composition relates to the sub-surface ocean composition, of which the findings of Cassini imply that the ocean might even harbor the conditions required for the existence of microbial life [5].

With this project, we aim to enhance the understanding of the data acquired by Cassini by conducting laboratory experiments, where the goal is to reproduce the plumes of Enceladus. The plumes are mimicked by using an experimental setup, and the objective is to conduct experiments with different models in order to retrieve the required physical and thermodynamic properties of an experimental setup to recreate Enceladus' plumes. The experimental setup contains a reservoir, filled with distilled water, which is heated at the bottom of the reservoir. On top of the reservoir are interchangeable models, each with different materials and/or channel geometries. The models are equipped with a set of sensors, which monitor the temperature and pressure. The sensors are connected to a computer, which produces timeline plots of the measurements. The experimental setup is placed in the test section of the *Hypersonic Testing Facility Delft* at the faculty of Aerospace Engineering. The observations and measurements are assessed with analytical and numerical models, to identify the connection between the physical and thermodynamic properties of the channel and the plume characteristics of Enceladus. The results contribute to a better understanding on the plume formation on Enceladus.

This study is part of an ongoing project, where the models used in this study are the third iteration of the physical model(s). The first iteration was made by T.J. Becx in 2019, and the second iteration by S. Sklavenitis in 2022. This project runs in parallel with a similar project, where the focus is on creating a numerical model of these plumes rather than a physical model. The numerical model supports the observations and behavior of the physical model. The first iteration of the numerical model was made by N.J. van der Hijden in 2021, and is continued by T. Fontés in 2022-2023. The physical characteristics of the new iteration are based on the conclusions and recommendations of the previous iterations.

1.1. Research questions

The main research question of this study is formulated as follows:

How can the thermodynamic processes and physical properties of an experimental setup be linked to the plumes of Enceladus?

The main research question is supported by the following subquestions, where a distinction is made between between the physical properties (the nozzle geometry) and the thermodynamic processes (the heat exchanges in the channel and cooling of the setup):

- **What is the effect of the geometry of a channel on plume formation?**
- **Which heat exchanges occur along the flow and how do these affect the flow properties?**
- **What are the effects on the flow properties when the experimental setup is cooled?**

1.2. Report outline

This report consists of 8 chapters, including this introductory chapter. The next chapter, Chapter 2, provides general information about the icy moon Enceladus, where the chapter is split into the general background information, and the current knowledge about the plume mechanisms. Chapter 3 provides information about the relevant gas dynamics, different flow types and thermal processes. In Chapter 4, the equipment and tools used to conduct the experiments are described. In Chapter 5, the first and second design iterations of this project are detailed in the prior designs section, and the design choices for the new model iteration, the manufacturing processes and the theoretical performance analysis of these models are subsequently described. The different experiments and results are detailed in Chapter 6, followed by the implications for Enceladus in Chapter 7. The conclusion and recommendations for future work are listed in Chapter 8.

2

Enceladus

In this chapter, the general information about Enceladus is given in Section 2.1, and the information about the plumes of Enceladus is given in Section 2.2.

2.1. The icy moon of Saturn

The section is divided into the discovery (Section 2.1.1), interior (Section 2.1.2) and surface (Section 2.1.3) of Enceladus.

2.1.1. Discovery

Enceladus, one of Saturn's icy moons with a subsurface ocean, was discovered by Friedrich Wilhelm (William) Herschel on August 28, 1789 and named after Greek mythology [6]. Enceladus is the 6^{th} largest moon of Saturn, and orbits between Mimas and Tethys. It has the highest albedo of the solar system, with a geometric albedo of 1.375 [7]. This makes it look like a bright, small (its radius is only 252 km) ball of ice orbiting Saturn. In the past, Voyager 1 and 2 (both launched in 1977) were the first to have a closer look at Enceladus. Cassini-Huygens (launched in 1997) was the first to target Enceladus. Cassini's primary mission was to gather information about Saturn, its rings, moons and magnetic environments. In 2005, the data acquired by Cassini's magnetometer made scientists want to take a closer look at Enceladus with a targeted fly-by [8], because the disturbed magnetic field could indicate the presence of a sub-surface (salty) ocean [1]. The disturbance is caused by the ejecta of the geysers, which becomes ionized (i.e., plasma), and bends Saturn's magnetic field near Enceladus, which is observed by Cassini. The bending of Saturn's magnetic field lines was the first evidence for active geysers on Enceladus [2]. On October 28, 2015, Cassini made the deepest dive through the plumes of Enceladus, which was only 25 km above the surface [7]. During these flybys, plumes' particles and gases were directly sampled by using its on-board Ion and Neutral Mass Spectrometer Subsystem (INMS) and Cosmic Dust Analyzer (CDA). Cassini was not designed to find life on Enceladus, but its instruments were able to look for conditions suitable for life, such as the presence of molecules from the 'CHNOPS' group in the plumes - which are carbon, hydrogen, nitrogen, oxygen, phosphorus and sulfur molecules. Cassini flew by Enceladus 147 times, of which 23 were close encounters. Cassini plunged into Saturn on September 15, 2017, after spending 20 years in space, 13 of those exploring Saturn. The data acquired by Cassini is still being investigated today. The Cassini mission is the only mission so far which headed towards Enceladus and as of yet, no other mission proposals have been approved to further investigate Enceladus.

The basic characteristics of Enceladus can be found in Table 2.1, where the dimensions, orbital parameters and more are summarized. The characteristics of the interior and surface are described in the following sections.

Table 2.1: Basic characteristics of Enceladus [7, 9].

Mean radius (km)	252.10 $\pm$ 0.2
a* (equatorial) (km)	256.6 $\pm$ 0.3
b* (equatorial (km)	251.4 $\pm$ 0.2
c* (polar) (km)	248.3 $\pm$ 0.2
GM (or μ) (km^{3}s^{-2})	7.2027 $\pm$ 0.0125
Density (kg m^{-3})	1609 $\pm$ 5
Heat flow estimates (discrete features**) (mW m^{-2})	60-220
Central pressure (MPa)	$\sim$23
Rotation period (days)	1.370 (synchronous)
Semimajor axis (km)	238042
Orbital period (days)	1.370
Eccentricity	0.0047
Obliquity (deg.)	0.003
Geometric albedo	1.375 $\pm$ 0.008
Core radius (km)	$\pm$190
Core density (kg m^{-3})	$\pm$2400
Average icy crust thickness (km)	$\pm$60

$[*]$ The a,b,c radii refer to the ellipsoidal shape axes.
$[**]$ The heat flux range is based on estimates for the south polar region, and are uncertain by a factor of 3.

2.1.2. Interior

Enceladus is estimated to have a rocky core with a radius of $\pm$190 km, and with a density of $\pm$2400 kg/m^3 [7]. This rocky core is expected to be surrounded by a liquid ocean/ice crust with an average thickness of 60 km, where the ratio of ocean/crust varies with latitude (deeper ocean and thinner ice crust near the south pole). There are however different interior structure models available, which show a significant difference in the division between the core, ocean and ice shell. Most of the possible interiors are determined on the basis of Cassini's measurements, combined with mathematical models (e.g. hydrostatic terms from equilibrium figure theory, elasticity, isostatic compensation, etc.). The difference between the interior models mainly comes from the different types of measurements being used (topography, gravity, librations), along with the different aforementioned mathematical models and assumptions being made. It is almost certain that Enceladus is a fully differentiated body. The south polar region has the thinnest ice shell and deepest part of the ocean, because most of the heat convection of the core/crust is occurring at the south pole [7]. This is because it is expected that Enceladus has a slightly aspherical core, which directs most of the generated heat towards the south pole. A possible interior structure of Enceladus can be seen in Figure 2.1.

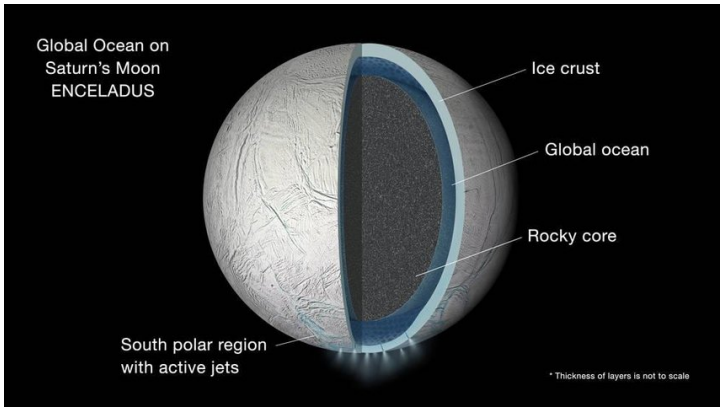

Figure 2.1: Possible interior of Enceladus with a global subsurface ocean [10].

2.1.3. Surface

Some parts of Enceladus' surface are heavily cratered by impacts, while other parts show no signs of craters. This is mainly caused by the plumes on Enceladus' south pole, from which icy material emanates, along with many other gas phase molecules, see Section 2.2.2. Part of the icy material falls back on Enceladus, when the particles cannot escape Enceladus' gravity (which is only 0.113 m/s^2, so roughly 1% of Earth's gravity). This makes the surface look 'new' and uncratered. The fresh, uncontaminated surface ice causes the high reflectivity, and thus the high albedo [9]. The icy material which does escape Enceladus' gravity is ejected into space, and is the main contributor to Saturn's E ring.

The most interesting feature can be found at the south polar region, from which the plumes emanate. There are four large crevasses, which are named tiger stripes, from which over 100 active geysers-like jets permanently eject 150-300 kg/sec (on average) of predominantly water vapor and icy particles (see Figure 2.2) [11, 12]. The current orientation of the tiger stripes maximizes the normal extensional tidal stresses, which suggests they began as tension cracks [13].

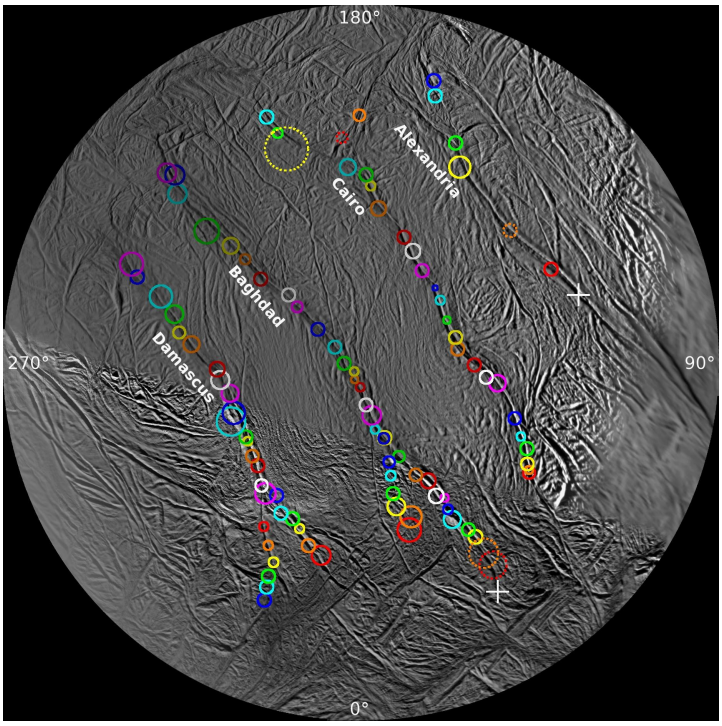

Figure 2.2: All 101 determined geysers. The circles indicate the uncertainty attached to each location. The different colors help distinguish between individual jets. NASA/JPL-Caltech/Space Science Institute.

Near the south pole, the surface is composed of water ice (in amorphous and crystalline form), CO_2 (trapped in the ice), NH_3, aliphatic hydrocarbons and sodium salts (less than 1%), while the rest of Enceladus' surface is composed mostly of just pure water ice [15, 16]. A 2016 study based on using Cassini's Visual and Infrared Mapping Spectrometer (VIMS) dataset combined with a model based on the spectral properties of water ice, showed a maximum south polar surface temperature of 128 K during daytime [17]. The derived surface temperature is much higher than the 72 K background temperature on other places around the south pole. A heat map of Enceladus' south pole can be seen in Figure 2.3.

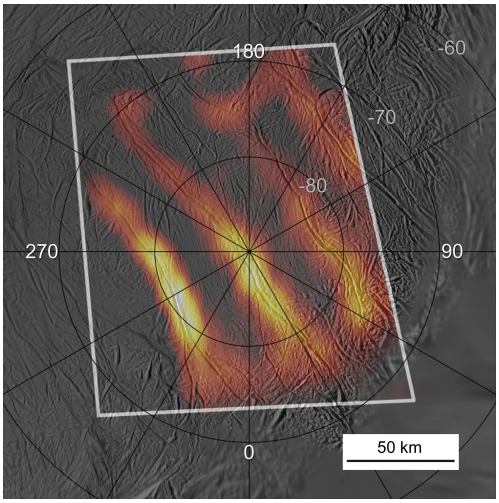

Figure 2.3: Heat map of Enceladus' south pole. The infrared radiation was mapped at wavelengths between 12 and 16 microns, and is superimposed on an image of the south pole, taken by Cassini and shown in false color [14].

2.2. The plumes of Enceladus

This sections focuses on the plumes of Enceladus. First, the different possible plume mechanisms driving the plumes are described in Section 2.2.1. Then, the characteristics and composition of the plumes are described in Section 2.2.2. Lastly, the effect and the importance of the tides are described in Section 2.2.3.

2.2.1. Plume mechanisms

Studies following the earliest (2005-2008) plume composition measurements by Cassini resulted in a broad range of possible plume mechanism models, since at that point it was not yet certain whether Enceladus had a subsurface ocean or not. The detection of sodium and potassium salts in the plume and the E-ring during later observations, especially in the slower and larger particles near the vent, are strong evidence for a liquid subsurface water source [18]. Besides, if particles were formed by condensation from the vapor, which had sublimated from ice, they would be practically salt-free [19]. Plume mechanism theories not requiring a subsurface ocean as a source of the plumes cannot justify the salt-bearing plume particles observed by Cassini and are therefore ruled out. The silicon-rich particles (most likely SiO_2) observed by the CDA also suggest formation in a hydrothermal system within Enceladus, adding to the evidence of a liquid water source [19]. This section focuses on 5 models where the source of the plumes is a subsurface water reservoir, with either a direct connection to space by means of a conduit, or via pressurized vapor chambers.

The open model

The first model is a model where the tiger stripes are tidally flexed, open slots that puncture the ice shell and directly connect the environment with the ocean. The open model can explain the total power output of the south polar terrain, the persistence of the eruptions through the tidal cycle and the phase lag [20]. Here, the phase lag is the delay between the peak plume flux and the peak tidal extension. A schematic overview of this model can be seen in Figure 2.4. The blue arrows indicate the flow of the vapor and ice particles, of which the flow intensity varies depending on the size of the opening of the crevasses, indicated by the dashed lines. The size of the opening in turn depends on the tidal stresses exerted by Saturn on Enceladus, which are indicated by the horizontal lines. This also drives the water level in the crevasse, indicated by the vertical arrow. The vertical water flow generates heat through viscous dissipation, which helps to prevent the crevasse from freezing despite the evaporative cooling of vapor escaping from the surface (indicated by the small, white triangle) [20]. The ejected vapor provides heat via condensation, which creates a relatively warm layer of surface material near the exit of the crevasse. This heat is conducted through the ice shell and explains the thermal emissions from the surface. The orange arrows and ”IR” indicate the infrared cooling of this warmer surface material.

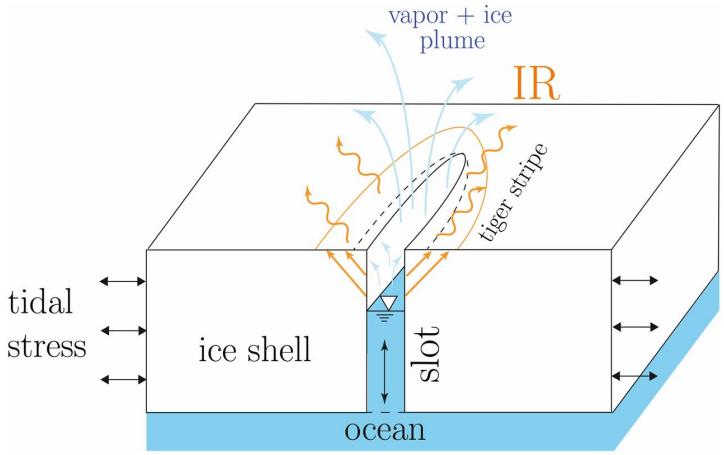

Figure 2.4: The open model [20].

The crevasse opening (the stress-free half width) is in the order of 1 meter, much wider and much narrower slots (from ’rest’) cannot be sustained. A wider crevasse opening allows a stronger erup-

tion because the flow is supersonic and choked, where a narrower opening increases the water level, flushes the slot and weakens the eruptions. This model, with open connections to the oceans, can sustain long-lived eruptions. The open connection is the simplest explanation for the composition of the plume as observed by Cassini, as it provides direct access to the materials of the ocean, and the water slots drive a volcano-tectonic feedback cycle that can be sustained on million-year timescales [20].

The cryovolcanic model

The second model is the cryovolcanic model. It is supposedly an answer to Cassini's observations of the thermal emissions near the tiger stripes, the tidal stresses and the geysers themselves [21]. The size of the hot spots is consistent with the condensation of the erupted vapor and liquid close to the surface, and its release of latent heat. A deep sea is the source of the eruption materials and heat. The mass production rates of the individual jets depend on tides, but not by how the tidal stresses directly influence the intensity of the plumes, as in the open model. Instead, the crevasses are choked by the process that also heats them: the near-surface condensation of the ejected vapor and ice, which turns the jets "on and off". To some degree, bulk viscous heating by tidal flexing of the ice shell underneath the south polar terrain is expected. The ice shell near the south polar terrain is likely the only place where convection occurs. A schematic overview of the cryovolcanic model can be seen in Figure 2.5.

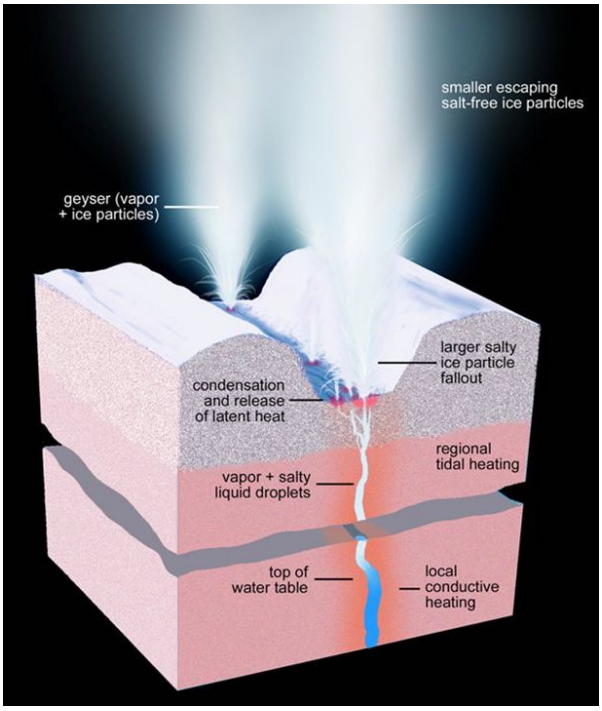

Figure 2.5: The cryovolcanic model [21]. The figure shows the geysering activity of Enceladus. Pressure builds up in crevasses which extend from the ocean to the surface, bringing seawater towards the surface, where it condenses and expels into space.

The cracks extend from the ocean to the surface, and pressurized liquid water fills the cracks and keeps them open. The water levels in the crevasses are within a few kilometers from the surface, water levels may (in small quantities) even rise all the way up to the surface. The ice shell is brittle near the surface, and becomes ductile at greater depths. The liquid water is brought to the surface and expelled by processes such as the exsolution of gases, essentially meaning that the particles dissolved in the ocean turn into their gas phase when the temperature drops near the surface and become bubbles, lowering the overall water pressure [22, 23]. The bubbles burst when the surface is reached, releasing the gas into the conduit. Also, the pressure due to topographic variations [24], or the pressurization of the ocean due to freezing and ice shell thickening drives particles upwards [25].

The water circulation model

The next model is a model with a water table below the surface, and above the ocean, as shown in Figure 2.6 [26]. In the figure, number 1 depicts the ocean, where the seawater rises through the crust (number 2) where the exsolution of gases occurs, due to the lower (near-) surface temperatures. The gas is mainly CO_2 gas, which produces bubbles when exsolved which lowers the overall density. The gas continues to rise to the water table. Because of the extra gas in the water table, the table builds up in pressure and 'pushes' the gas towards the plume chambers (number 5). The water in the water table is relatively warm (0 degrees Celsius, which is 2 degrees above the freezing point of salty water), and its heat is conducted through the upper ice shell, number 3. The surface heat is lost via radiation (number 4), explaining the temperature profiles observed by Cassini. The water from the water table supplies the plume chambers with heat, CO_2 and other chemicals observed in the plumes [26]. When the heat is conducted through the ice and the gas is 'stored' in the plume chamber, the water becomes colder and more dense, and thus recirculates back into the ocean through small cracks in the ice shell (number 6). CO_2 gas and clathrate hydrates come from subsurface gas pockets (number 7). The upper ice cap cannot be perfectly smooth, and the exsolved CO_2 bubbles gather in recesses in the bottom of the upper ice cap. The CO_2 builds up and the pressure increases, and subsequently the CO_2 is released to the surface either by slowly seeping through newly created cracks towards the surface or by blowout - fast venting of the CO_2 [26]. The expelled CO_2 forms frost deposits near the vent (number 8).

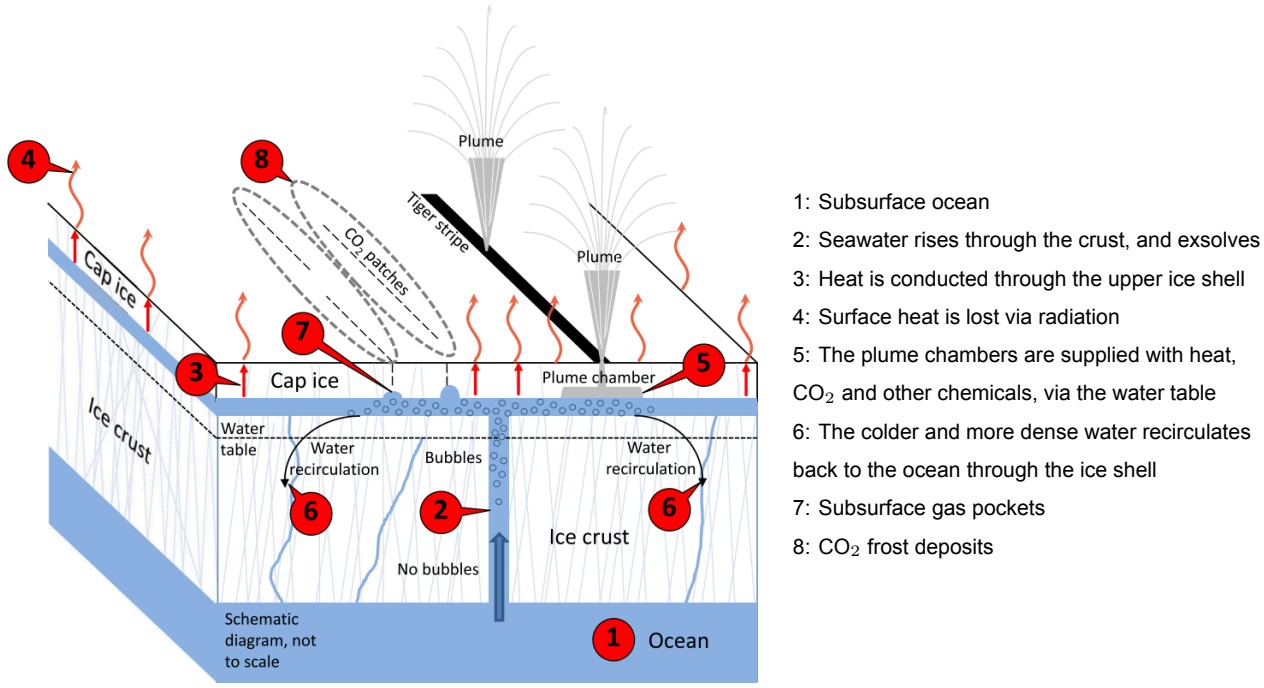

Figure 2.6: The water circulation model, with the inclusion of CO_2 patches [26].

The pressurized chamber and the controlled boiling model

The open model and the cryovolcanic model assumed narrow conduits, where the radius of the evaporating area is approximately equal to the area of the opening of the vent, see the right figure in Figure 2.7. The left figure, however, where the evaporation area of the liquid-gas interface is much larger than the area of the opening of the vent, is also plausible according to different articles by Postberg and others [27, 28].

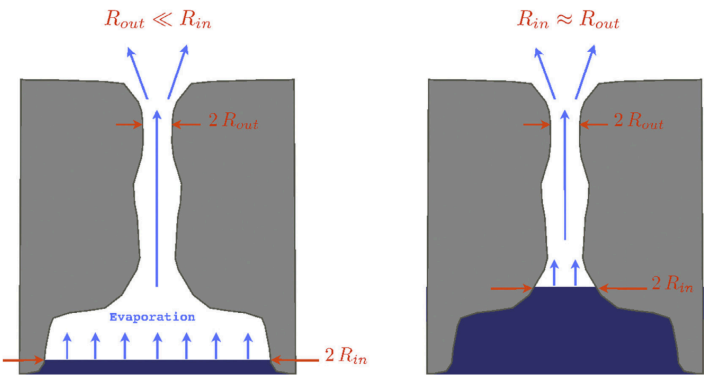

Figure 2.7: A large evaporating surface (left) and evaporation in a narrow conduit (right) [27, Supp. info]

These articles claim that using heat-flow arguments, it can be shown that the liquid-gas interface area is orders of magnitudes greater than the crevasse itself, which requires a large vapor chamber above the liquid, that narrows to the vent channel, as depicted in Figure 2.8 [27]. The article also shows that in the case of a small liquid-gas interface (i.e., no pressurized vapor chamber), an ”implausibly large temperature gradient in the liquid is needed to maintain a heat flux required to support the steady state gas evaporation” [27, Supp. info]. It is also stated that the composition and dynamics in the solid phase of the plume, and the low concentration of insoluble gases such as N_2, CO and CH_4 in the gas phase, strongly imply that there are large evaporation surfaces at a salt water reservoir (or more reservoirs in case of non-contiguous evaporation surfaces) that provide all the constituents of the plume [28].

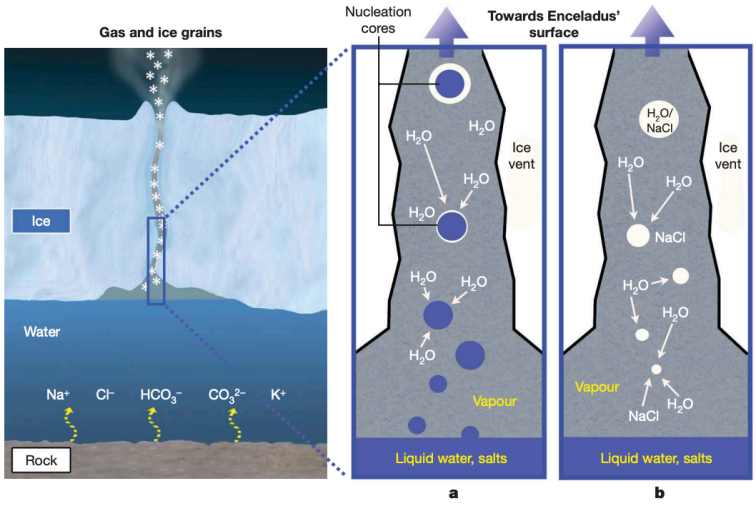

Figure 2.8: A large evaporation chamber. a) depicts the Na-rich grains, b) the Na-poor grains [27].

However, evidence against the hypothesis of the pressurized chamber model is stated in a more recent (coupled) article by Ingersoll and Nakajima, which led to the introduction of the concept of controlled boiling [29, 30]. A schematic overview of the controlled boiling model can be seen in Figure 2.9.

Controlled boiling arises from the backpressure due to wall friction when the gas flows upwards in the crevasse [30]. In long and narrow crevasses, the backpressure increases such that the liquid approaches the saturation vapor pressure, which greatly reduces the evaporation rate. The heat released into the walls by the freezing of the liquid is conducted through the ice shell, and radiated into space from the surface. The liquid-gas interface is about 2 km below the surface. To prevent the crevasses from freezing, the salinity of the ocean has to be greater than 20 g/kg, and the crevasse width should be at least one meter [30]. Since boiling already occurs 10s of centimeters below the liquid-gas interface, the bubbles eliminate the thermal boundary layer.

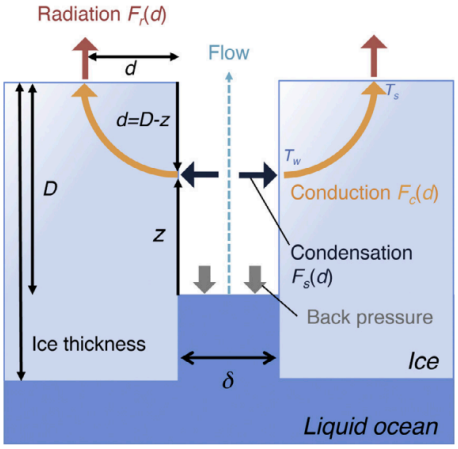

Figure 2.9: The controlled boiling model [29].

After reviewing the models presented earlier, it can be concluded that the actual plume mechanism cannot be fully determined based on the observations by Cassini. Many models are not in agreement on the channel shape, the mechanism driving the plumes and whether a reservoir is present. Additional observations during a future visit of the icy moon, preferably both plume and ice-penetrating, are required to determine the actual plume mechanism of Enceladus. Performing laboratory experiments where the thermodynamic conditions of Enceladus are recreated, could give more insight into the required crevasse properties and thermodynamic conditions.

2.2.2. Characteristics

The hydrothermal material from Enceladus' core is brought to the surface by both convection and the exsolution of gases, of which the latter creates bubbles. It is expected that an organic rich film at the liquid-gas interface exists, where there is a high concentration of poorly soluble material [31]. The bubbles moving upwards through this organic-rich film become aerosolised organics moving upwards in the crevasse, and the detected HMOC (High-Mass Organic Cations) are suggested to originate from this film. As briefly mentioned in the previous section, if icy moons are to have plumes, a lower boundary on the salinity of the (subsurface) ocean is introduced in order to prevent freezing of the liquid-gas interface [30]. The salt rich water ice grains are so called 'type 3' grains. Beside the type 3 grains, there are also type 1 and type 2 grains. The different ice grain types are created in different sections of the crevasse, see Figure 2.10 [31]. The different ice grain types can be described as follows:

- **Type 1 grains** - These grains represent grains of almost pure water ice.
- **Type 2 grains** - These grains show features consistent with grains containing significant amounts of organic material. The compositional range is more diverse, in contrast to type 1 and 3. We can divide the type 2 grains in subclasses:
  - **Type 2N** - Nitrogen-bearing
  - **Type 2O** - Oxygen-bearing
  - **Type 2A** - Aromatic-bearing [1]
  - **Type 2M** - Mixed-type (a combination of any of the above)
  - **HMOC** - High-Mass Organic Cations, with specific spectral features: repetitive peaks separated by molecular mass: 12-13 u, and ranging from 80 u until at least 200 u (the approximate limit of CDA).
- **Type 3 grains** - These grains are indicative of salt-rich water ice grains.

[1] Aromatic compounds are compounds with a cyclic structure. The compounds contain double bonds, so that they have a planar three-dimensional structure [32].

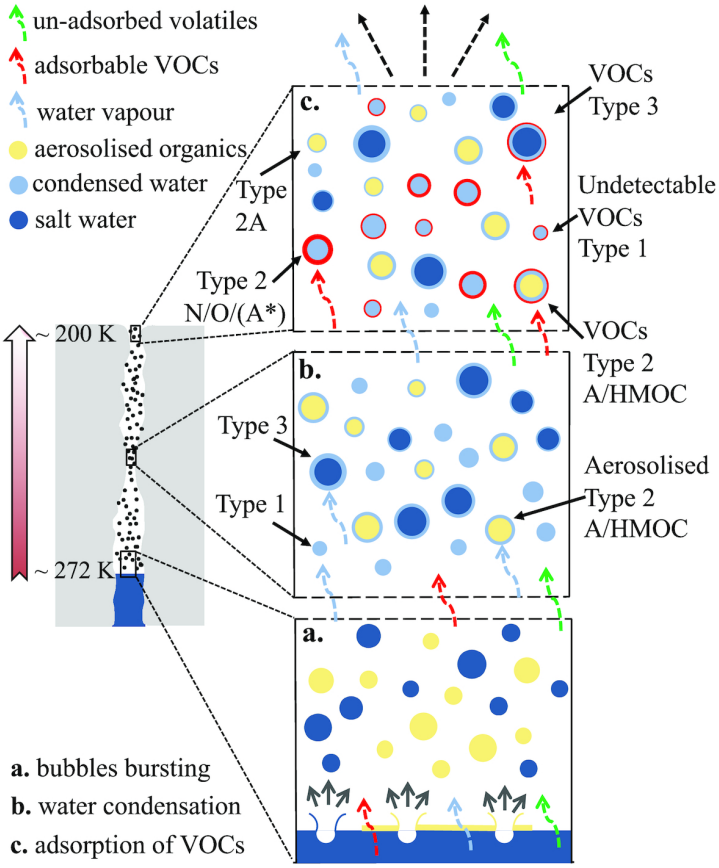

Figure 2.10: Overview of the formation of ice grains inside the crevasse [31].

The figure shows a schematic overview of the formation of the different ice grain types throughout the crevasse, for temperatures gradually decreasing from approximately 272 K at the liquid-gas interface until approximately 200 K near the vent. The VOCs stand for Volatile Organic Compounds: low-mass soluble organics. At Fig. 5.1a, the water vapor and gas bubbles exsolve and move towards the surface, where they burst. The bursting of the bubbles creates a spray of both salt-water aerosols and droplets of organic material, which is, as mentioned before, expected to cover the liquid-gas interface. The dashed arrows indicate the volatile species which make up the gaseous part of the plume. A summary of the composition of the gaseous part of the plume can be seen in Table 2.2. At Fig. 5.1b, about halfway through the crevasse, the crevasse becomes narrower in this model. The water vapor becomes super-saturated (see Section 3.2). Water vapor (light blue dashed arrows) condenses and forms type 1 ice grains, being almost pure water ice. The vapor also condenses on the aerosolised organics and the salt water aerosols, which act as nucleation cores which form type 2A/HMOC grains and salt-rich type 3 grains [31]. Some of the VOCs are also adsorbed here, but the adsorption is more efficient at Fig. 5.1c, closer to the vent, where the temperatures are colder. The grains formed at Fig. 5.1b are smaller than the grains from the freezing of ocean spray at Fig. 5.1a, and are therefore accelerated to higher speeds than the grains from Fig. 5.1a. [16]. At Fig. 5.1c, VOCs (type 2N/2O) that condense below 200 K and have high binding energies, can adsorb onto all previously mentioned ice grains from Fig. 5.1a and Fig. 5.1b. If a sufficient amount of volatile organics are adsorbed onto a type 1 grain, it can be converted to a type 2N/2O grain. The 'sufficient amount' is determined by the detectability of Cassini: if the INMS cannot detect aromatic compounds (and thus still classify the particle as a type 1 grain), it cannot be completely ruled out that this particle is in fact a type 2A ice grain (indicated as A*) [31].

Table 2.2: Summary of Enceladus' volatile plume compositions as measured by Cassini's INMS [33].

Major species	Minor species I			Minor species II		
No ambiguity	Moderate ambiguity			High ambiguity		
>0.1%	<0.2% and >100 ppm			<100 ppm		
		Hydrocarbons	N-bearing	O-bearing	NO-bearing	Others
H_2O (96-99%)	CO	C_3H_4	CH_5N	O_2	C_2H_7NO	Ar
	C_2H_2	C_3H_6	C_2H_3N	CH_3OH	$C_2H_5NO_2$	H_2S
	C_2H_4	C_3H_8	C_2H_7N	C_2H_2O	$C_3H_7NO_2$	PH_3
CO_2 (0.3-0.8%)	C_2H_6	C_4H_8	$C_2H_6N_2$	C_2H_4O		C_3H_5Cl
	N_2	C_4H_{10}	C_4H_9N	C_2H_6O		
CH_4 (0.1-0.3%)	HCN	C_5H_{10}	$C_4H_8N_2$	C_3H_6O		
	CH_2O	C_5H_{12}	$C_6H_{12}N_4$	C_3H_8O		
	NO	C_8H_{18}		$C_2H_4O_2$		
NH_3 (0.4-1.3%)				$C_2H_6O_2$		
				$C_4H_{10}O$		
H_2 (0.4-1.4%)				$C_4H_6O_2$		

The plumes are ejected into space with velocities of around 350-950 m/s, and even up to 1.25 km/s [3, 4]. This estimation is based on numerical models combining Cassini's Ultraviolet Imaging Spectrograph (UVIS) and (the aforementioned) INMS measurements. The solid fraction of the plumes is estimated to be around 10-20% [34]. It is estimated that the average source rate for the water molecules is 300 kg/s [12].

2.2.3. Tides

For the previously discussed plume mechanisms, it is evident that the tidal interactions play a key role in creating and maintaining the plumes. Besides the generation of heat in the interior of Enceladus, the slightly eccentric orbit of Enceladus also leads to a periodic, diurnal variation in the mass and velocity of the plume particles [35]. The 2:1 orbital resonance with Dione also leads to periodic decadal variations, inducing tidal stresses.

During the 33 hour orbital period of Enceladus, the distance to Saturn and the orbital velocity slightly oscillates. This oscillation causes changes in the surface stresses and water levels in the crevasse, which influence the plume activity. Both the Imaging Science Subsystem (ISS) and VIMS instruments observed a clear correlation between the plume activity and Enceladus' position along the eccentric orbit, as shown in Figure 2.11 [36]. When Enceladus is closest to Saturn (at periapse), the tidal stresses are the highest and the plume intensity diminishes, due to closure of the crevasses. The peak in the plume mass flux is when Enceladus is furthest away from Saturn (at apoapse), where the cracks are the most open and the evaporating area is the largest [35]. Due to the filling and flushing of the crevasses, there is a delay between the peak tidal extension and the peak plume flux. This delay is about 1 rad in the orbit, or $\pm$5.1 hours [20]. The intensity and density of the plumes can vary spatially (so along the same crevasse) by a factor up to 10, depending on the time-variable tidal stress fields and subsurface interactions, and the overall plume source rate (of all plumes combined) can vary by a factor of $\sim$5 [37].

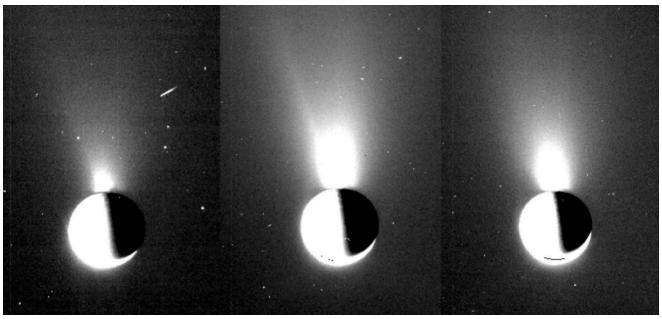

Figure 2.11: The time variability of an isolated jet [35]. The picture on the left is from June 18, 2017, the picture in the center from August 2, 2017, and the picture on the right is from August 28, 2017. This individual jet contributes about 3% of the slab density at 100 km altitude, meaning that this is an intense plume considering the other 97% comes from the other 100 geysers.

3

Gas dynamics and theory

In this chapter, the theoretical background of the gas dynamics and thermal processes in this study are described. First, the general concepts of flows through nozzles are described in Section 3.1. Then, the thermal processes in the channel and phase changes of water are described in Section 3.2. Lastly, the different flow types and used equations in this study are described in Section 3.3.

3.1. General concepts

On Enceladus, the water vapor is expected to flow through one or more constrictions (narrowings) in the crevasse. These constrictions act as a throat: the section with the smallest cross-sectional area. The flow is sonic at this area, after which it will continue to expand and accelerate due to the increase in cross-sectional area. The sonic condition means that the gas flow is equal to the local speed of sound, or $\sqrt{\gamma RT}$ with γ being the ratio of specific heats (γ = 1.33 for water vapor, used in the remainder of this study[1]), and R being the gas constant (R = 461.5 J/kgK for water vapor, used in the remainder of this study[1]), and T the local temperature in Kelvin. The flow can only become sonic at the throat if the critical pressure ratio is reached. This is the pressure ratio between the downstream (vent) and upstream (reservoir) pressure, and its value depends on the specific heat ratio and is 0.54 for γ = 1.33. Based on the narrowness of the crevasses, the crevasses act as a nozzle through which the gas flow expands and is accelerated to supersonic speeds. A channel with a converging and diverging section is called a *de Laval* nozzle. Since the critical pressure ratio must be reached for the flow to become supersonic, the pressure distribution in a channel thus has a large effect on the behavior of the flow. The typical flow patterns with corresponding pressure distributions for a de Laval nozzle can be seen in Figure 3.1.

[1] https://www.ohio.edu/mechanical/thermo/property_tables/gas/idealGas.html

Number (a) in Figure 3.1 is what happens if the critical pressure ratio is not reached [38]. The flow accelerates in the converging part, and decelerates in the diverging part, but the flow remains subsonic throughout the channel. If the pressure in the chamber is increased, or the ambient pressure is reduced, eventually the flow will become choked, which is the case of (b). In this case, the exit pressure is still too low for the flow to become supersonic after the throat, so it exits the channel subsonically. The Mach number at the throat is now 1, and any increase in chamber pressure will not change the downstream conditions of the flow. The mass flow rate of the flow is highest when the flow is choked.

If the ambient pressure is now reduced further, a supersonic region is formed after the throat (number (c)). The ambient pressure in this case is not sufficiently low to maintain a supersonic region all the way to the vent, and a normal shockwave occurs somewhere between the throat and the vent. The normal shock causes a sudden increase in temperature, pressure and density and will make the flow subsonic again. If the ambient pressure is reduced further, the shockwave will shift towards the vent, in the case of number (d). The flow will have a higher velocity due to the longer accelerating section, but will still leave the channel subsonically because of the shockwave.

Further decreasing the ambient pressure will bend the shockwave outwards and cause a complicated sub- and supersonic flow pattern outside the channel. This case (number (e)) is referred to as an overexpanded flow, and is achieved when the pressure at the vent is lower than the ambient pressure. When the ambient pressure is reduced further, the shockwaves will disappear and the flow will be supersonic throughout. This is the preferred condition when designing a nozzle, and is called the design condition (number (f)). Finally, if the ambient pressure is reduced even more, the pressure at the vent will be higher than the ambient pressure (number (g)). In this case, the flow is underexpanded, and introduces expansion waves at the vent, bending the flow outwards and creating a complex wave pattern.

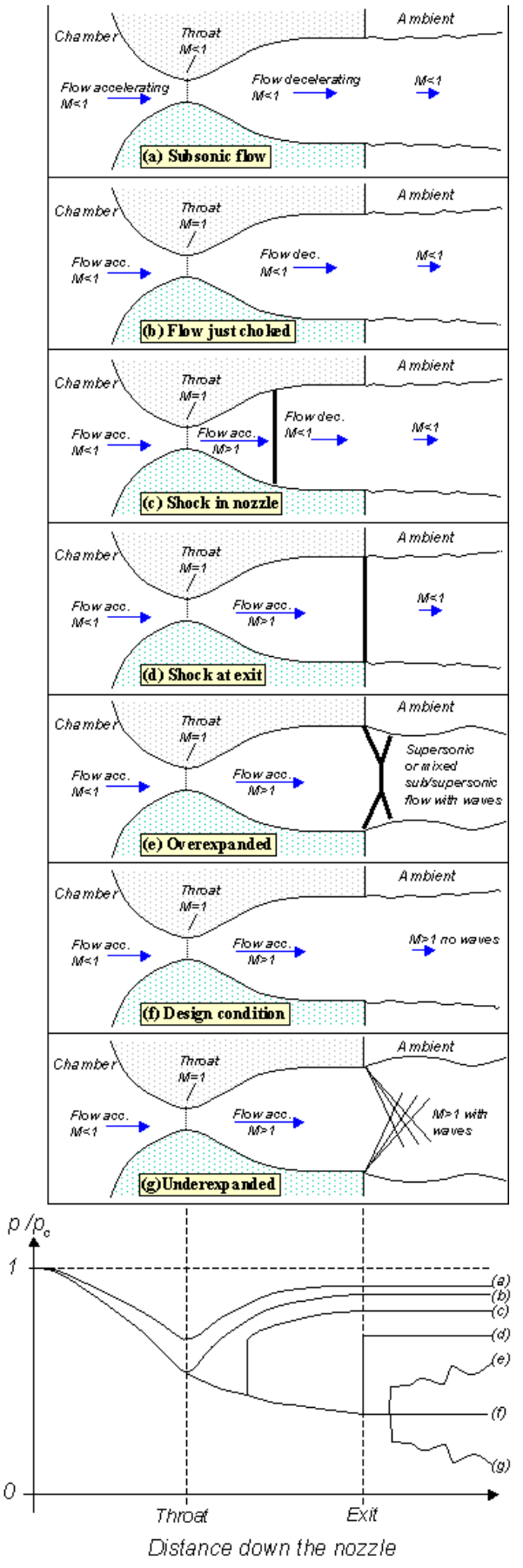

Figure 3.1: Different flow patterns through a converging-diverging nozzle [38]. The pressure distributions on the bottom figure refer to the flow regimes of the figure above.

The decompression from the ocean into an erupting plume is assumed to be adiabatic and reversible. An adiabatic flow means that there are no heat exchanges with the environment and no phase changes in the channel, and the exchange in mass between the walls near the vent and the exiting gas is negligible [36]. Adiabatic and reversible are the two main conditions for an *isentropic flow*. For an isentropic flow, the entropy does not change (hence isentropic), but the density, pressure and temperature can. The entropy is a quantitative measure of microscopic disorder for a system [39]. These assumptions allow (first order) semiquantitative analysis of the fluid dynamics along the crevasse [34], although it cannot be assumed that every section of the actual crevasses on Enceladus are isentropic, due to the presence of viscous losses and heat exchanges. If the nozzle is not considered as ideal, i.e. the viscous losses of the flow momentum are taken into account, there may be flow separation from the walls, condensation and shock waves [36]. The crevasses on Enceladus are presumably not ideal.

For that reason, 3 different flow types are considered in this study: the isentropic flow mentioned before, the Rayleigh flow (which considers only heat addition) and the Fanno flow (which considers only friction). The different flow types will be described in more detail in Section 3.3, as the heat exchanges and friction have significant effects on the flow. Besides their direct effects on the flow parameters, the presence of solid particles which have formed in the channel lower the local speed of sound. To quantify: if the mass fraction is about 10% (where 10-20% is typical for Enceladus' plumes [34]), and there is an equilibrium between the gas and the particles, the speed of sound is reduced by about 8% [36]. This is possibly due to the combination of a liquid and solid having a higher entropy than a solid alone under the same conditions [34]. The analytical treatment of the Rayleigh and Fanno flows used this study assume a constant cross-sectional area of the channel, whereas this channel area can change for an isentropic flow. For the isentropic flow, the exit-plane velocity and Mach number are determined by the throat-to-exit area ratio.

An overview of the flow velocity, temperature, density and condensed mass fraction along the crevasse of Enceladus can be seen in Figure 3.2 [40]. It can be seen that the flow velocity is zero at the reservoir, subsonic (M<1) from the reservoir to the throat, sonic at the throat (M=1, the green line in subfigure c), and supersonic (M>1) from the throat to the vent. The vapor starts condensing after the throat, and what this physically means is explained in Section 3.2.

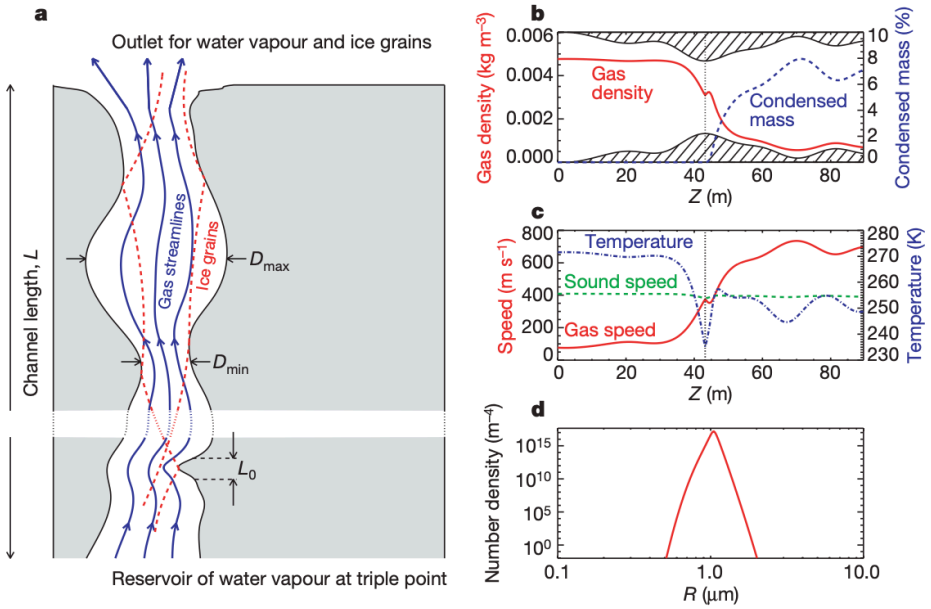

Figure 3.2: Schematic overview of the flow of gas and ice grains in a crevasse model [40]. b) shows the gas density and condensed mass along the channel, c) the temperature, speed of sound and speed of the gas flow along the channel, and d) the particle number density per radius increment, for a single channel.

All the different flow types assume an ideal gas. For an ideal gas, there are no interparticle interactions, and so the ideal gas law applies. At standard temperature and pressure, many gases (such as nitrogen, oxygen and hydrogen) can be treated as ideal gases with reasonable tolerances, but water vapor cannot, as the water can still change phases at the considered pressure and temperature [39]. However, at low pressures (below 10 kPa), water vapor can be treated as an ideal gas, regardless of the temperature [39].

Besides the adiabatic expansion after the throat in the channel, there is also adiabatic cooling/expansion when the vapor exits the vent and is ejected into space [16]. The gas becomes collisionless after being ejected, at altitudes that are between 10-100 times the vent diameter [16]. If the gas is sufficiently collisional at the vent, the adiabatic expansion into the vacuum of space almost completely converts the thermal motion to directed motion, giving the gas an ultimate speed of $\sqrt{2\gamma RT_0/(\gamma-1)}$, where T_0 is the stagnation temperature of the gas [K], when it was in thermal equilibrium with the liquid or walls of the crevasse [36]. At the altitudes where Cassini made its observations (at least 25 km altitude), the ejected gas and particles were already decoupled.

3.2. Thermal processes

At the liquid-gas interface of Enceladus' crevasses, there is water in its liquid and gaseous state, as the name suggests. It is surrounded by water in its solid form: walls of solid water ice. Each phase, solid, liquid or gas, has a different molecular structure. For a solid, the distance between the molecules is small and the attractive forces between the molecules is large, keeping the molecules fixed. The molecules oscillate at their equilibrium position. This oscillation depends on the temperature, and if the temperature is increased, the oscillation increases. At a given (higher) temperature, the momentum created by the oscillation has become too large for the molecules to stay together, and they will break apart. This is the melting process, and the solid has turned into the liquid phase. Except for water (since ice is less dense than liquid water), the distance between molecules has become larger in the liquid phase and molecules can move freely, as the inter-molecular forces are weaker and they are no longer in fixed positions. For a gas, there is no inter-molecular order, and the molecules are far apart. They move in random directions and the only molecular interactions are due to the collisions of the molecules. The overall energy of a gas is larger than in a solid or a liquid, and this energy must be released before the gas can condense or deposit [39].

Whether a substance is in its solid, gas or liquid phase, depends on the local pressure and temperature. An equilibrium between multiple phases can also exist: for a certain temperature and pressure, a substance can be in an equilibrium between all its three phases, this point is called the triple point. A diagram for the phases of water where the pressure is plotted against the temperature, can be seen in Figure 3.3. For high pressures and temperatures, the critical point can be seen: this is the point where the saturated liquid and saturated vapor states are identical [39]. What a saturated state physically means, is detailed in the next paragraph. The negative slope of the freezing point with decreasing pressure (until the triple point, indicated by the blue line between ice and water), is due to the fact that water expands when it freezes. The pressure-temperature or P-T diagrams are available for practically all substances. The addition of a certain substance to another substance can change its triple point, e.g. when salts are dissolved in liquid water.

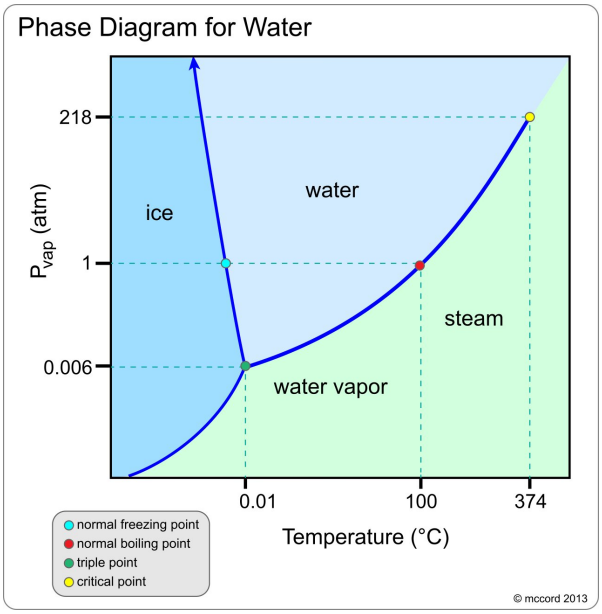

Figure 3.3: Phase diagram of water. University of Texas - Chemistry 302.

A substance that is about to change phase is called saturated. So a saturated liquid is a liquid that is about to vaporize, and a saturated vapor is a vapor that is about to condense. For a given temperature, the pressure at which this phase change occurs is the saturation pressure. Vice versa for a given pressure, then the phase change occurs at the saturation temperature. The amount of energy released or absorbed during this phase change is the latent heat. The latent heat of vaporization can be referred to as the enthalpy of vaporization, which is the amount of energy required to vaporize a certain mass of a saturated liquid for a given temperature and pressure. The total enthalpy H is defined as the total internal energy (U) plus the product of the pressure (P) and the specific volume (ν), or H = U + Pν [J]. A phase change that releases energy (condensation/freezing/deposition) is called exothermic, and a phase change that requires/takes energy (vaporization/melting/sublimation) is called endothermic.

In a nozzle, a vapor can also become supersaturated. Due to the adiabatic expansion after the throat, the pressure and temperature drop. Normally, the vapor will start to condense but because of the large velocity of the vapor inside the nozzle, it may not spend enough time in the nozzle to transfer the necessary heat and change phases. The condensation will then be delayed, which is known as supersaturation. If the temperature is sufficiently cooled below the saturation temperature (for a given pressure), condensation will take place, regardless of the initial temperature and pressure at the entrance of the nozzle. This is also referred to as the Wilson point. If a liquid is heated beyond its saturation temperature (at constant pressure), the liquid will still remain at its saturation temperature until it is fully evaporated, before the vapor can increase in temperature again if continuous heat is supplied.

Something similar happens when the local pressure is reduced to a vacuum, e.g. in space or in a vacuum chamber. It can be seen in Figure 3.3 that below the triple point pressure, water only exists in its solid or gaseous form. So if liquid water is placed inside a vacuum chamber, the boiling point will be much lower, so it immediately starts to boil. During the boiling, the temperature of the water will drop due to the evaporative cooling, an endothermic process. This means that the latent heat of the vaporization is absorbed from the liquid water and surrounding vapor. Because the surrounding vapor is being continuously pumped out by the vacuum pumps, the liquid cools rapidly. The liquid will freeze when the local temperature is below its freezing point, and will then slowly sublimate.

When vapor becomes supersaturated in a channel, there will first be a region of non-equilibrium condensation, as can be seen in Figure 3.4. The non-equilibrium condensation zone is where nucleation occurs, and the pressure increases [41]. There are two types of nucleation: heterogeneous nucleation and homogeneous nucleation. The main difference between the two is that for homogeneous nucle-

ation, there are no foreign nuclei (i.e. other molecules) present and the vapor condenses on itself, while for heterogeneous nucleation there are foreign nuclei present, and the water molecules nucleate on these foreign nuclei [42]. The heterogeneous nucleation case is said to be fully isentropic, while for the homogeneous nucleation case there is a big increase in entropy. A combination of both cases is also possible. The growing process of the nuclei is in the equilibrium condensation zone, and the pressure starts to decrease again. If the pressure in the non-equilibrium condensation is increased such that the pressure becomes higher than the pressure at the geometrical throat, a thermal throat is generated, which is the case in Figure 3.4b. This phenomenon is called thermal choking, and is accompanied by a condensation shock wave. The flow becomes subsonic again after the shock wave, although it can still be accelerated to supersonic velocities in the channel section after the shock wave.

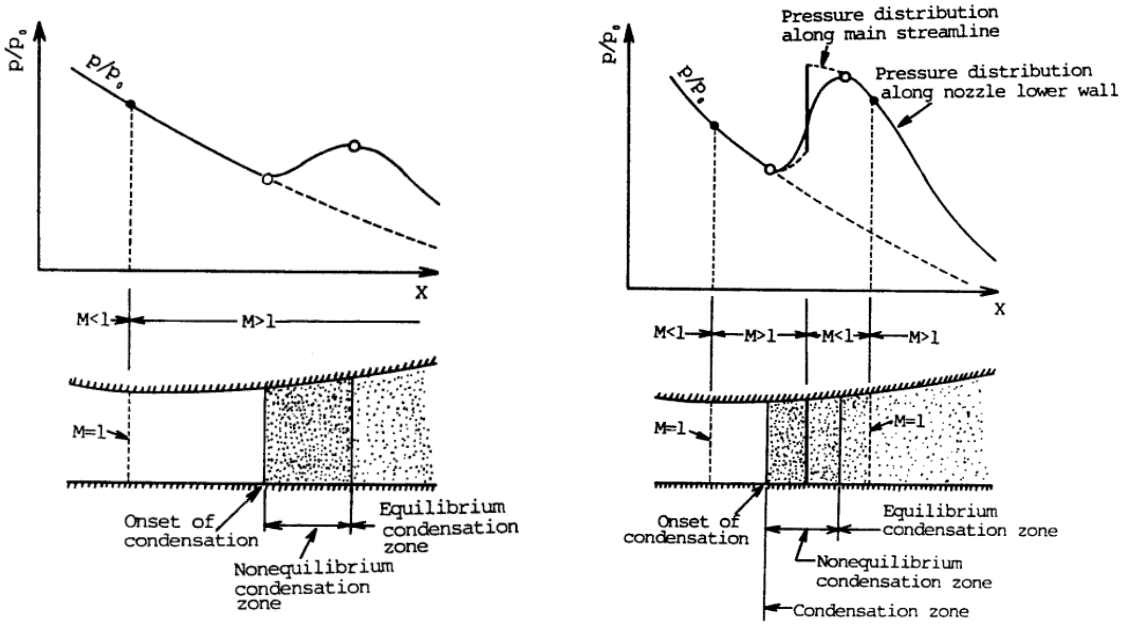

(a) Pressure distribution without a condensation shock wave.

(b) Pressure distribution with a condensation shock wave.

Figure 3.4: Mechanism of flow with condensation, with and without a condensation shock wave[41].

3.3. Flows and equations

In this section, the three different flow types and their corresponding equations are described. First, the general, governing equations are described in Section 3.3.1. Then, the isentropic flow is described in Section 3.3.2. The Rayleigh and Fanno flows are described in Section 3.3.3 and Section 3.3.4, respectively.

3.3.1. Governing equations

If a flow consists of gases which can be considered as ideal, the ideal gas law applies [43]. This law (Equation 3.1) relates the pressure P $[Pa]$ to the density ρ $[kg/m^3]$ and the temperature T $[K]$, and is also referred to as the equation of state. R is the specific gas constant in $[J/kgK]$.

$$P = \rho RT \tag{3.1}$$

If the flow is uniform at any given cross section, the flow can be considered as a quasi-one-dimensional flow, which assumes conservation of mass, momentum and energy. The continuity equation (Equation 3.2) relates the density, velocity V $[m/s]$ and cross-sectional area A $[m^2]$ along the duct, and is also referred to as the conservation of mass [43]. The subscripts 1 and 2 indicate different locations in a channel, meaning that the product of the density, velocity and flow area remains constant in the channel.

$$\rho_1 V_1 A_1 = \rho_2 V_2 A_2 \tag{3.2}$$

The momentum equation for a steady quasi-one-dimensional flow can be expressed as Equation 3.3 [44]. The integral term is the pressure force acting perpendicular to the flow direction, within the control volume of location 1 and 2 (indicated by the subscripts).

$$p_1 A_1 + \rho_1 V_1^2 A_1 + \int_{A_1}^{A_2} p dA = p_2 A_2 + \rho_2 V_2^2 A_2 \tag{3.3}$$

The energy equation can be expressed as Equation 3.3 [44]. The energy equation states that the total enthalpy H of the flow is constant.

$$H_1 + \frac{V_1^2}{2} = H_2 + \frac{V_2^2}{2} \tag{3.4}$$

The degree of saturation of the flow is determined by the following equation (Equation 3.5):

$$S = \frac{p_{gas}}{p_{eq}^{(l.g.)}(T_{gas})} \tag{3.5}$$

which means that the saturation degree depends on the ratio of the local pressure of the gas and the saturated vapor pressure, at the temperature of this gas. The liquid-gas equilibrium pressure is subsequently determined as follows (Equation 3.6), where the liquid-gas equilibrium pressure only depends on the gas temperature in an exponent term [45]:

$$p_{eq}^{(l.g.)}(T_{gas}) = 610.8\,\mathsf{exp}[-5.1421\,\mathsf{ln}(T_{gas}/273.15) - 6828.77(1/T_{gas} - 1/273.15)] \tag{3.6}$$

The solid-gas equilibrium pressure is given by Equation 3.7:

$$p_{eq}^{(s.g.)}(T_{gas}) = \mathsf{exp}[-2663.5/T_{gas} + 12.537)\,\mathsf{ln}(10)] \tag{3.7}$$

where the solid-gas equilibrium pressure also only depends on the gas temperature in an exponent term. The solid-gas and liquid-gas equilibrium equations are combined to produce the phase diagram of water.

3.3.2. Isentropic flow

The first flow type is the isentropic flow, where there is no change in entropy along the flow. The flow is considered adiabatic, inviscid and reversible. This is a 'simple' representation of a flow, as it disregards thermal and frictional processes in the channel. The isentropic conditions allow the analysis of a flow through a varying cross-sectional area channel. The typical progression of a subsonic isentropic flow in a converging-diverging channel can be seen in Figure 3.5a, and a supersonic flow in Figure 3.5b.

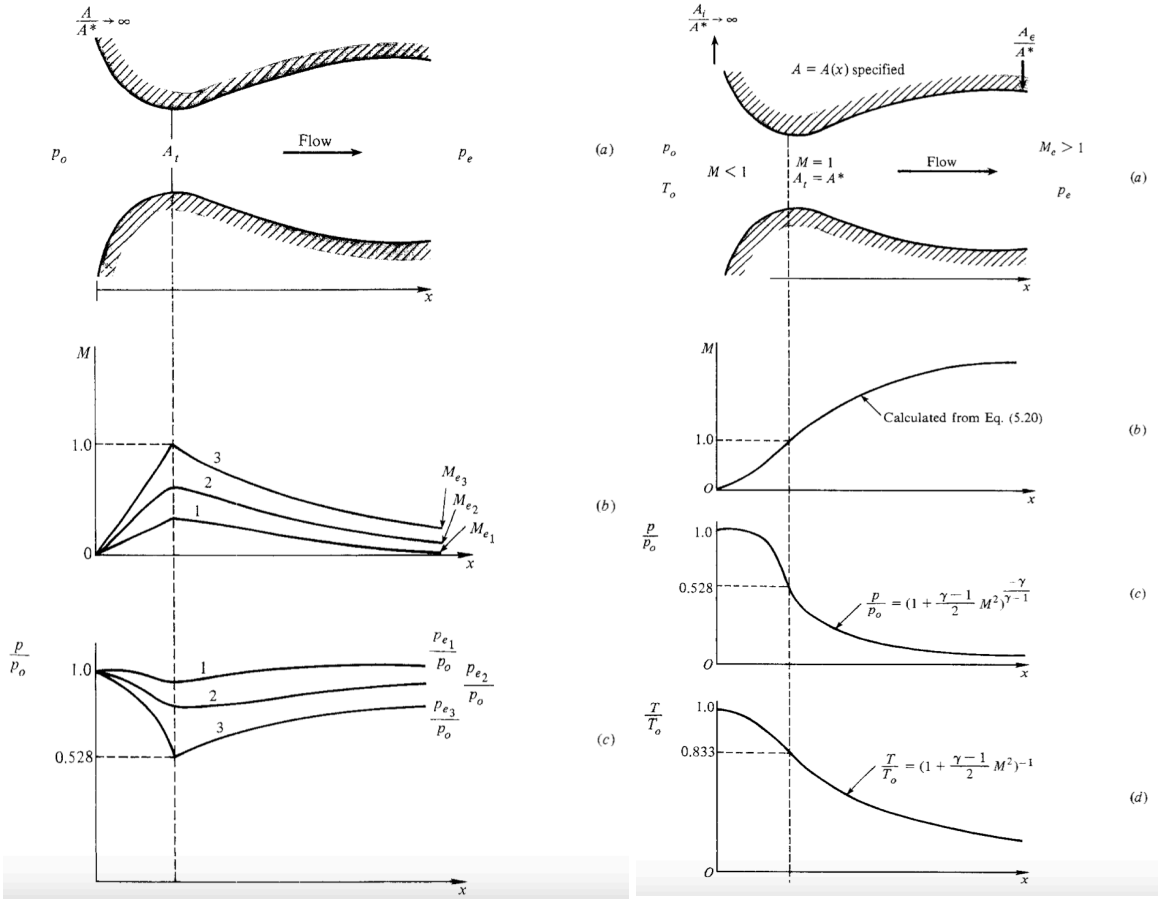

(a) Progression of the subsonic isentropic flow. Note that the critical pressure ratio is 0.528 instead of 0.54, since the flow of air is assumed instead of water vapor.

(b) Progression of the supersonic isentropic flow. The flow starts subsonic and becomes sonic at the throat, if the critical pressure ratio is reached.

Figure 3.5: Subsonic and supersonic isentropic flow [44].

In the figure, the cross-sectional area is related to the velocity of the flow. The area-velocity relation relates the change in area to the change in velocity, and its behavior for subsonic and supersonic flow. The area-velocity relation tells us that sonic flow can only occur at a throat, and to accelerate a subsonic flow, the area must decrease (and vice-versa) and to accelerate a supersonic flow, the area must increase (and vice-versa). It is given by Equation 3.8 [43], where M is the Mach number $[-]$:

$$\frac{dA}{A} = \left(M^2 - 1\right) \frac{dV}{V} \tag{3.8}$$

The isentropic flow relation of an ideal gas through a nozzle is the area-Mach number relation seen in Equation 3.9, where the Mach number is a function of the local duct/sonic throat area, at any location along the duct [43]. The isentropic flow equation tells us that the Mach number is related to the ratio of the vent area to the throat area, and that there is both a subsonic (infinite number of solutions) and supersonic (one solution) value for the Mach number to satisfy the equation. The equation is as follows, with A^* being the sonic throat area $[m^2]$ and γ being the specific heat ratio $[-]$:

$$\left(\frac{A}{A^*}\right)^2 = \frac{1}{M^2}\left[\frac{2}{\gamma+1}\left(1 + \frac{\gamma-1}{2}M^2\right)\right]^{(\gamma+1)/(\gamma-1)} \tag{3.9}$$

The Mach number of the flow can be derived from the pressure-, density- and temperature ratio. This study uses the pressure- and temperature ratios, where the Mach number calculation by using the pressure ratio is given by Equation 3.10 and by using the temperature ratio by Equation 3.11 [46]. These equations can be used to determine the Mach number at any location in the channel. P_{res} is the

pressure in the reservoir, and T_{res} is the temperature in the reservoir.

$$M = \sqrt{\left(\frac{2}{\gamma - 1}\right)\left[\left(\frac{P_{res}}{P}\right)^{(\gamma-1)/\gamma} - 1\right]} \tag{3.10}$$

$$M = \sqrt{\left(\frac{2}{\gamma - 1}\right)\left[\left(\frac{T_{res}}{T}\right) - 1\right]} \tag{3.11}$$

By rearranging, the equations for the pressure- and temperature ratio can then be written as Equation 3.12 and Equation 3.13, respectively.

$$\frac{P}{P_{res}} = \left(1 + \frac{\gamma - 1}{2}M^2\right)^{\frac{-\gamma}{\gamma-1}} \tag{3.12}$$

$$\frac{T}{T_{res}} = \left(1 + \frac{\gamma - 1}{2}M^2\right)^{-1} \tag{3.13}$$

The conservation of mass of the flow implies that the mass flow rate at location 1 should be equal to the mass flow rate at location 2, being: $\dot{m} = \rho V A$, in [kg/s]. By using the conservation of mass, the isentropic flow relations and the equations of state, the mass flow rate can be written in the form of Equation 3.14 [46].

$$\dot{m} = \frac{AP_{res}}{\sqrt{T_{res}}}\sqrt{\frac{\gamma}{R}}M\left(1 + \frac{\gamma - 1}{2}M^2\right)^{-\frac{\gamma+1}{2(\gamma-1)}} \tag{3.14}$$

When the Mach number becomes one, the flow is choked and M drops out of the equation, and the choked mass flow can be written as Equation 3.15.

$$\dot{m} = \frac{AP_{res}}{\sqrt{T_{res}}}\sqrt{\frac{\gamma}{R}}\left(\frac{\gamma + 1}{2}\right)^{-\frac{\gamma+1}{2(\gamma-1)}} \tag{3.15}$$

The solid fraction at the vent can be calculated by using Equation 3.16 [47]. However, this equation is based on the conservation of enthalpy rather than the conservation of entropy, and is therefore not isentropic. It is a theoretical function where the change in temperature between the reservoir and the vent is converted to the solid fraction, based on the latent heat of vaporization h_{vap} [J/kg]. c_p is the specific heat capacity at constant pressure, in [J/kgK].

$$f_{vent} = \left(1 + \frac{\Delta h_{vap}}{\frac{1}{2}\cdot V_{vent}^2 + c_{p,vent}\cdot T_{vent} - c_{p,res}\cdot T_{res}}\right)^{-1} \tag{3.16}$$

3.3.3. Rayleigh flow

The Rayleigh flow is a flow type where only heat addition and removal is considered. There is no change in cross-sectional area (so a straight channel), and there are no frictional losses. Due to the heat addition, there is a change in stagnation temperature and pressure, and the Rayleigh flow is therefore not adiabatic. It is also irreversible. The concept of the Rayleigh flow can be described by the Rayleigh line, depicted in Figure 3.6. The Rayleigh line is plotted in a temperature-entropy diagram, and is only valid for a straight channel. It can be seen that heating the flow accelerates subsonic flow, and decelerates supersonic flow. Cooling does the opposite: decelerate subsonic flow and accelerate supersonic flow. So a subsonic flow can be accelerated until it is choked at Mach 1 when heat is added, and accelerate to supersonic speeds if heat is removed after the choking point. The maximum entropy is achieved when M = 1, and the maximum enthalpy is achieved at $M = 1/\sqrt{\gamma}$.

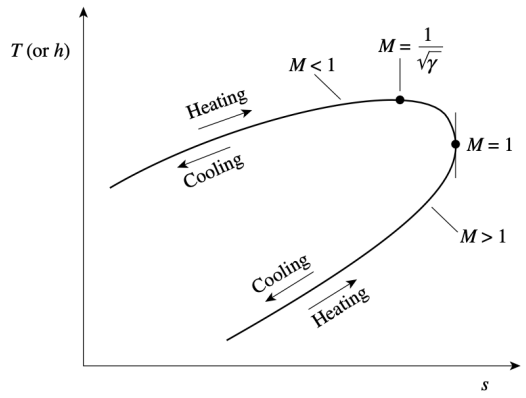

Figure 3.6: The Rayleigh line [46]. Heating and cooling in a constant area channel.

The Rayleigh flow relations are summarized below [48]. The pressure and temperature ratios are defined as Equation 3.17 and Equation 3.18, respectively. P^* and T^* indicate the temperature and pressure at the sonic point, where the flow becomes choked.

$$\frac{P}{P^*} = \frac{\gamma + 1}{1 + \gamma M^2} \tag{3.17}$$

$$\frac{T}{T^*} = \left(\frac{(\gamma + 1)\, M}{1 + \gamma M^2} \right)^2 \tag{3.18}$$

The velocity ratio of the flow is given by Equation 3.19. It is equal to the inverse of the density ratio, being ρ^* / ρ.

$$\frac{V}{V^*} = \frac{(\gamma + 1)\, M^2}{1 + \gamma M^2} \tag{3.19}$$

The stagnation pressure and temperature ratios (specified by P_0 and T_0) are given by Equation 3.20 and Equation 3.21.

$$\frac{P_0}{P_0^*} = \frac{\gamma + 1}{1 + \gamma M^2} \left(\frac{2\left(1 + \frac{\gamma - 1}{2} M^2\right)}{\gamma + 1} \right)^{\frac{\gamma}{\gamma - 1}} \tag{3.20}$$

$$\frac{T_0}{T_0^*} = \frac{2\,(\gamma + 1)\, M^2 \left(1 + \frac{\gamma - 1}{2} M^2\right)}{\left(1 + \gamma M^2\right)^2} \tag{3.21}$$

3.3.4. Fanno flow

The Fanno flow is the adiabatic, irreversible flow through a constant cross-sectional area channel, without shock waves. The flow is irreversible because for the Fanno flow, the viscous losses are taken into account, i.e., friction. The flow is therefore also not isentropic. The friction generates a boundary layer at the walls of the channel, because of the shear stresses working in opposite direction of the flow [44]. The generated boundary layer essentially squeezes the flow, accelerating subsonic flow and decelerating supersonic flow towards Mach 1. For a subsonic flow in a straight channel, the Mach number can theoretically never exceed 1 due to friction alone. If the conditions are such that the flow would exceed Mach 1 in the channel before the channel exit, pressure waves are propagated upstream so that the flow is 'adjusted' and the sonic point is shifted towards the vent. For the Fanno flow, similar (stagnation) pressure, temperature and velocity relations exist as the Rayleigh flow, but in this study we are only interested in the choked flow duct length L^*, which can be calculated using Equation 3.22 [48]. L^* is thus the point along the channel where the flow becomes choked, in [m]. f is the friction or shear stress coefficient [-] and D is the diameter of the channel [m]. By doing experiments, all parameters are known except for the friction coefficient, which can then be calculated.

$$\frac{4 f L^*}{D} = \frac{1 - M^2}{\gamma M^2} + \frac{(\gamma + 1)}{2\gamma} \ln \left(\frac{(\gamma + 1) M^2}{2 + (\gamma - 1) M^2} \right) \tag{3.22}$$

In general, the effects of friction are negligible for 'slow' (M<1) flows through large diameter pipes. The effects become more serious if the channel diameter is small and/or Mach numbers are high. In practice, the flow is turbulent in almost all cases, and the friction coefficient must be determined empirically [44].

When the Fanno and Rayleigh equations approach their limits at sonic conditions, so at M = 1, it can be shown that with the addition of heat and/or friction, the sonic point is no longer at the throat [46]. The location of the sonic point in case of heat transfer depends on whether heat is added or removed from the flow, or in mathematical terms: a positive or negative sign of the heat transfer term. In case of heat removal, as could be the case on Enceladus due to the icy walls, the sonic point can be before a throat. On the other hand, if heat is added to the flow the sonic point is shifted downstream of the throat, at a diverging section of the channel. It is more likely that there is heat addition when working with an experimental setup at room temperature, unless the setup is cooled. Since this differs from the case on Enceladus, the effects are tested and evaluated in Chapter 6. Friction also tends to push the sonic point downstream of a throat.

4

Equipment and tools

This chapter focuses on the used equipment and tools in order to retrieve and analyze the data from the experimental setup. The setup consists of a heated reservoir, and on top of this reservoir a model is placed which simulates the flow through a channel (see Chapter 5). The setup is placed inside a vacuum chamber, which is described in Section 4.1. The reservoir is heated by using heating foils that are connected to a power supply (Section 4.2). The signals from the temperature and pressure sensors (of which the working is described in Section 4.3) are then converted into meaningful temperature and pressure measurements by using signal processing modules and software, which is described in Section 4.4.

4.1. Vacuum chamber

In order to mimic the environment of Enceladus, the experimental setup is placed in a vacuum chamber. The vacuum chamber used in this study is the Hypersonic Test Facility Delft (HTFD). A schematic overview of the windtunnel can be seen in Figure 4.1. The windtunnel is located at the High-Speed Laboratory of the Aerospace Engineering faculty of TU Delft.

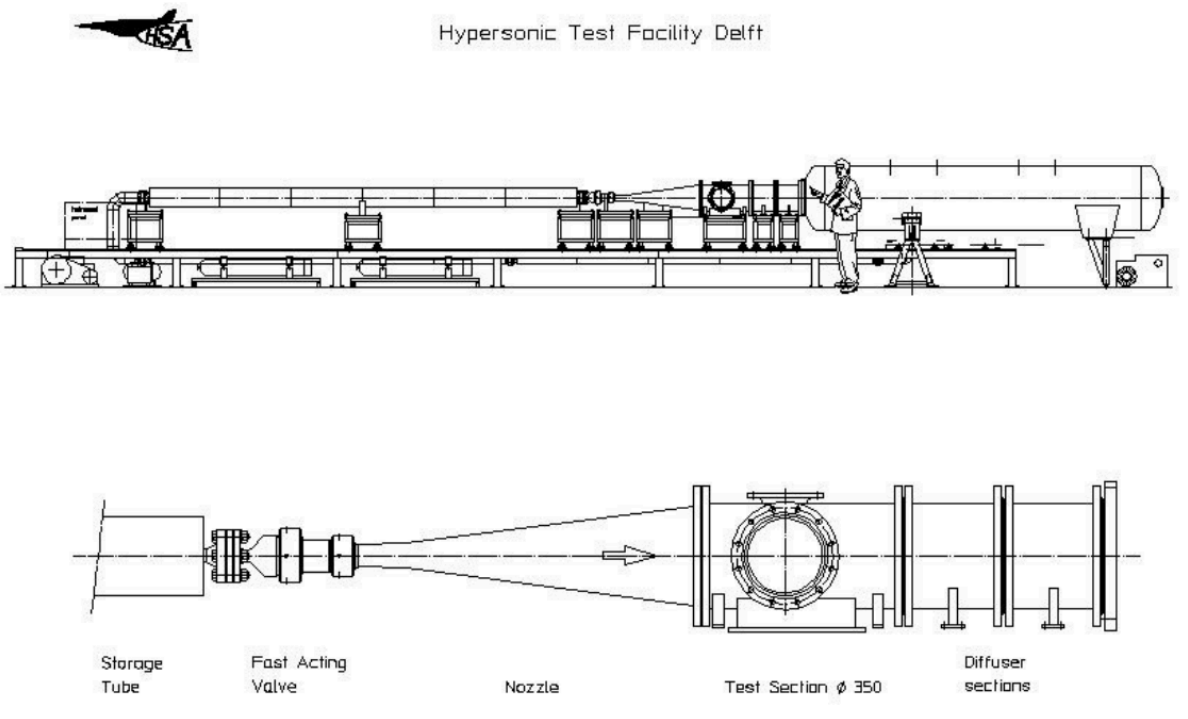

Figure 4.1: Schematic overview of the HTFD [49]

The windtunnel uses the Ludwieg tube principle - and consists of a heated expansion tube (the large tube on the left side of Figure 4.1), a nozzle (in the middle of the figure), a test section and a discharge tank, which are located on the right side of the figure. For this study, the nozzle and 29 meter long tube are detached from the test section, in order to increase the efficiency of the vacuum pumps by reducing the volume of the chamber, and to reduce air leaks. The test section, discharge tank and vacuum pumps simply act as a vacuum chamber when detached, so we are only interested in the test section (see Figure 4.2a), and will not dive into the details of the working of the windtunnel.

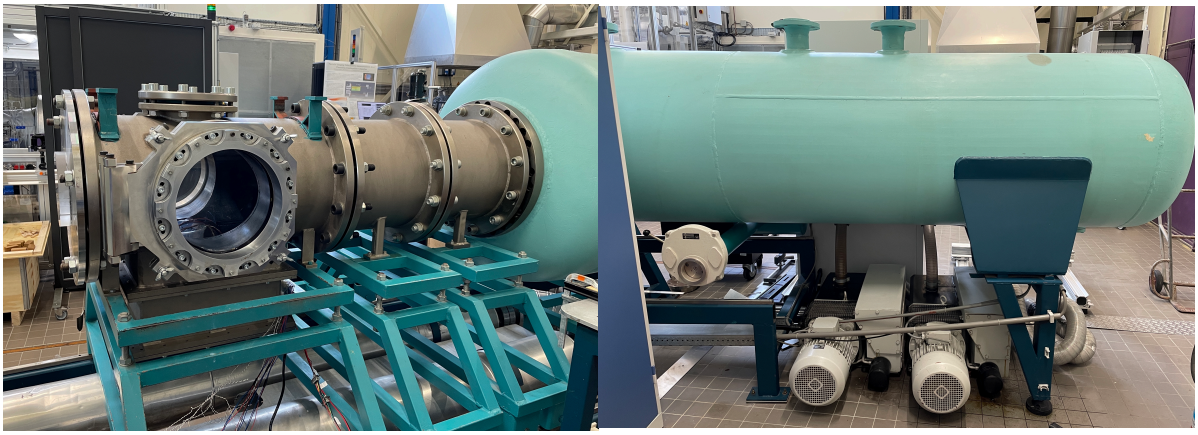

(a) Overview of the test section of the HTFD.

(b) Vacuum discharge tank, with the two vacuum pumps underneath.

Figure 4.2: In the left figure, the test section of the vacuum chamber can be seen. In the figure on the right are the vacuum pumps and the vacuum discharge tank.

The test section (Figure 4.2a) has a heavy lid as an opening, with a window through which the experiments can be observed. The opening has an inner diameter of 260 mm, thus the experimental setup needs to fit through this opening and has to be placed in the test section. The total height of the test section, so from the bottom to the top window, is 640 mm. The length and width are 350 mm and 250 mm, respectively. The discharge tank and test section are being evacuated by two vacuum pumps, which can be seen in Figure 4.2b.
The pressure inside the vacuum chamber is measured using a *Leybold Thermovac TR 211* pressure sensor, which is connected to a *Leybold Thermovac TM 20* controller. The controller has a built-in screen to see the current pressure inside the chamber, but also has an output channel to log the pressure measurements. The pressure sensor has an operating range of $5{\cdot}10^{-4}$mbar to 1000 mbar[1], and has an output given in volts. This means that a conversion from Volt to (milli)bar is required to process the measurements (see Section 4.4.2). The chamber has an idle voltage of about 10.017 V at atmospheric pressure, and the voltage is typically between 5-6 V during the experiments, which translates to between about 1 and 5 mbar. The controller has a relative uncertainty of $\pm$20% between $1.0{\cdot}10^{-3}$ and $9.9{\cdot}10^{-3}$ mbar, $\pm$15% between $1.0{\cdot}10^{-2}$ and $9.9{\cdot}10^{1}$ mbar and $\pm$50% between $1.0{\cdot}10^{2}$ and $1.0{\cdot}10^{3}$ mbar [2]. Because the controller is designed to operate with low pressures, the uncertainty is lower when the pressure is lower.

The test section has a side panel, through which holes can be drilled for cables to pass through. This is done for the temperature control (Section 4.2) and the measuring equipment (Section 4.3). The cables are sealed using hot glue, to minimize the leaks from the side panel. To determine the warm-up time of the vacuum pumps before an experiment, the chamber was evacuated without a setup inside. The results can be seen in Figure 4.3, where the room temperature was 24.5 °C.

[1] https://www.leyboldproducts.nl/en/products/measuring-and-analysis-instruments/pressure-measurement/passive-sensors/thermovac-sensors/1824/thermovac-tr-211?number=15785

[2] http://www.hvg-verwertung.de/ebay/dokumentation/leybold/Messtechnik/TM20_PV20.pdf

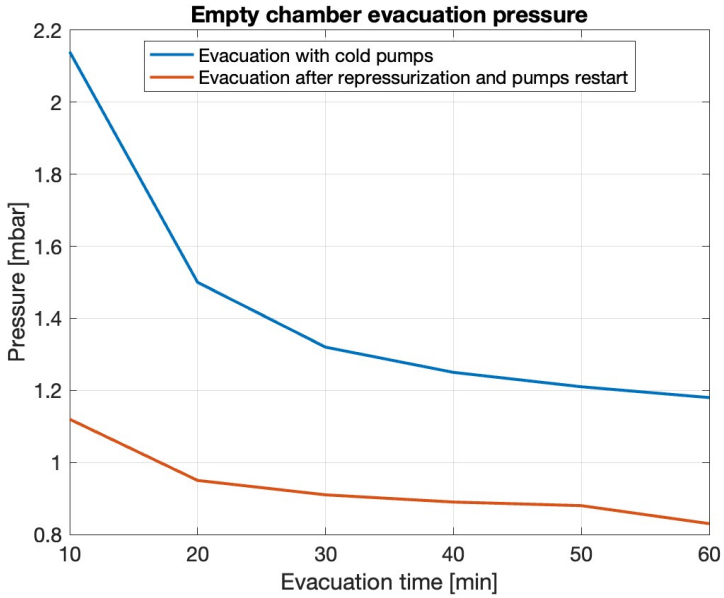

Figure 4.3: Evacuation with an empty test section.

The room temperature was 26.5 °C after the tests, which was caused by the heat released by the vacuum pumps and the weather conditions: it was a hot, sunny day. The significant increase in room temperature will be taken into account throughout the experiments, as it can affect the temperature of the experimental setup (which is discussed in Section 6.7.3).
The vacuum pumps will warm-up 30 minutes with an empty chamber before the first experiment of the day, because after 30 minutes the reduction in pressure becomes negligible. The chamber will then be re-pressurized and re-started with the setup inside. The chamber pressure with the setup inside is much higher than the values above, as will be explained in Chapter 6.

4.2. Temperature control

During the evacuation of the vacuum chamber, the only variable that can be controlled during an experiment is the amount of heating power being supplied to the reservoir water. This requires a power supply, of which the characteristics are explained in Section 4.2.1. The power supply is connected to multiple heating foils which warm up the reservoir water from below, as will be explained in Section 4.2.2.

4.2.1. Power supply

The heating foils are powered by the *Geti GLPS 3003E* laboratory DC power supply. The power supply has two output channels, of which the voltage and current of both channels are continuously adjustable. Each channel has a voltage range of 0-30 V and a current range of 0-3 A. The voltage and current output of the channels can be seen on a display on the device. The voltage is displayed with 1 decimal1 accuracy, and the current with 2 decimals. This means that for this study, the uncertainty in the supplied voltage is $\Delta U = 0.05$ V and $\Delta I = 0.005$ A for the supplied current. The ripple and noise under constant voltage is less than 1 mV, and is neglected for this study. The specifications of the power supply can be retrieved from the manufacturer [3].

4.2.2. Heating foils

The power supply is used to power the heating foils. A heating foil is essentially an electric resistor, sealed in a waterproof film. When the electric power is turned on, the heating foil converts this power into heat. The foils are placed at the bottom of the reservoir, and are submerged with water during the experiments. By adjusting the power output, the temperature of the reservoir water can be controlled to some extent, which in turn (partially) determines the pressure inside the reservoir. The flow properties can therefore be adjusted by controlling the power supply. The heating foils are necessary to prevent

[3] https://www.geti.eu/en/products/workshop/laboratory-power-supplies/laboratory-power-supply-geti-glps-3003e-2x0-30v-0-3a-5v-3a

the water in the reservoir from freezing.

The two channels of the power supply are both used for this study: one channel is connected to a larger, single heating foil (hereafter referred to as the large foil), and the second channel is connected to a series of 12 smaller heating foils (hereafter referred to as the small foils). The specifications of the heating foils can be found in Table 4.1, of which the specifications of the small foils are retrieved from the manufacturer [4] and the specifications of the large foil are determined by measurements in the laboratory in the previous work of S. Sklavenitis [47].

Table 4.1: The heating foils used in this study.

	Large foil	Small foils
Brand	Minco	Telemeter Electronic
Type	Custom	KP20x20R24L500
Dimensions (length x width)	122 x 26 mm	20 x 20 mm
Heating power per foil*	28.56 W at 24 V	6 W at 12 V
Resistance	24 Ω	20.17 Ω
Amount of foils used	1	12

* = *Heating capacity for the given (calibration) voltage, not the maximum power output.*

The power is simply calculated using Joule's law: $\mathcal{P}$ [W] = U [V] * I [A], where U [V] = I [A] * R [Ω], which is used to derive the resistance. The uncertainty in the heating power provided by the heating foils originates from the uncertainty in the supplied voltage and current by the power supply. Calculating the uncertainty of the heating power is done by using Equation 4.1 [47].

$$\Delta\mathcal{P} = |U \cdot I| \cdot \sqrt{\left(\frac{\Delta U}{U}\right)^2 + \left(\frac{\Delta I}{I}\right)^2} \tag{4.1}$$

The large foil with the maximum power supplied by the power supply has a voltage of 32.1 V and current of 1.61 A, as will be elaborated on further in Section 6.1.1. This results in a maximum heating capacity of 51.68 W. The small foils have a maximum voltage of 27 V, and maximum current of 3.26 A, which results in a heating capacity of 88.02 W. So their combined heating power is 139.7 W. Filling in the voltage and electric current values for both the large foil and the small foils in Equation 4.1 results in a $\Delta\mathcal{P}$ of 0.1796 W for the large foil, and a $\Delta\mathcal{P}$ of 0.2116 W for the small foils. The total uncertainty of the heating power can then be calculated using Equation 4.2.

$$\Delta\mathcal{P} = \sqrt{0.1796^2 + 0.2116^2} = 0.2775W \tag{4.2}$$

4.3. Measuring equipment

To determine the parameters of the flow inside the channel of the model and of the reservoir, measuring equipment will have to be installed. For this experiment, thermocouples (Section 4.3.1) are used to measure the temperature, and pressure sensors (Section 4.3.2) are used to measure the differential pressures. This section explains how the equipment functions.

4.3.1. Thermocouple

The temperature along the channel and of the reservoir is measured by using 5 T-type thermocouples. A thermocouple is a pair of two conducting metal wires, where for a T-type thermocouple the positive wire consists of copper and the negative wire is an alloy of copper and nickel. The wires are joined at one end, and they operate using the Seebeck effect. This means that a thermoelectric voltage is generated between the two wires of different composition, proportional to the temperature difference between the ends of the wires [5]. The other end of the wires is connected to a module which can translate this voltage into a temperature reading in degrees Celsius (see Section 4.4.1). The thermocouple

[4] https://telemeter.info/media/productattachments/files/b/r/brochure_flexible_heaters_web.pdf
[5] https://web.archive.org/web/20080216165303/http://www.temperatures.com/tcs.html

has a short term operating temperature range between -250 °C and 400 °C, and a continuous operating temperature between -185 °C and 300 °C [6], which is a much wider range than used in this study.

There are however uncertainties in the thermocouple measurements. The acquired data from the thermocouples is prone to statistical noise, both from the thermocouples themselves as well as all the electronics the thermocouples are connected to. The noise is the same for each thermocouple, and is determined to be ΔT_{noise} = 0.25 °C [47]. Besides noise, the individual thermocouples have a certain offset. The offset can be different for each thermocouple, but prior analysis has shown that these are equal for each thermocouple. The offset is determined to be 0.03 °C for an individual thermocouple, so the total offset for 5 thermocouples can be calculated using Equation 4.3 [47].

$$\Delta T_{off} = \sqrt{0.03^2 + 0.03^2 + 0.03^2 + 0.03^2 + 0.03^2} = 0.0671°C \tag{4.3}$$

The total uncertainty of the thermocouples can be acquired by combining the noise and the offset, by using Equation 4.4:

$$\Delta T = \sqrt{\Delta T_{off}^2 + \Delta T_{noise}^2} = 0.2588°C \tag{4.4}$$

This is the total uncertainty for each individual thermocouple reading, assuming that there is no correlation between the noise and the offset.

4.3.2. Pressure sensor

The pressure sensors are used to measure the pressure along the channel. The sensors used in this study are differential pressure sensors, except for the absolute chamber pressure sensor. The differential pressure sensor consists of a high-pressure port and a low-pressure port, and the output of the sensor is the difference in pressure between these ports. The output is given in volt, so a conversion from volt to (milli)bar is required to process the measurements (see Section 4.4.2). The high pressure port is connected to the channel of the model, while the low pressure port is not connected to anything, i.e., equal to the pressure inside the vacuum chamber. So in order to retrieve the local pressure, the chamber pressure has to be added to the differential pressure of a sensor. An overview of the specifications of the sensors is given in Table 4.2.

Table 4.2: The pressure sensors used in this study.

Brand	First Sensor	All Sensors	Honeywell
Type	HCLA12X5EU	ELVRL10D1RTINA5F	NSCDJJN005NDUNV
Amount used	1x (P1)	1x (P2)	3x (P3, P4, P5)
$P_{diff,max}$	12.5 mbar	25 mbar	$\pm$ 5 inH_2O (≈12.45 mbar)
$V_{supply,ideal}$	5.0 V	5.0 V	Not provided
V_{off}	0.278 V*	2.336 V*	2.556, 2.5625, 2.5655 V*
$V_{out,max,ideal}$	4.25 V	4.25 V	2.5355, 2.541, 2.544 V*
$V_{out,max,real}$	4.96 V*	5.02 V*	3.07, 3.04, 3.06 V*

** = Measured/determined in the lab.*

Where:

- P_{diff} is the differential pressure measured by the sensor. It is defined as the difference between the high- and the low pressure port.
- $P_{diff,max}$ is the maximum operating differential pressure of the sensor. The sensor is designed to measure differential pressures up to this value.
- U_{out} is the voltage output of the sensor, which is converted to mbar.
- U_{off} is the voltage offset of the sensor, defined as the voltage output when P_{diff} = 0.
- $U_{supply,ideal}$ is the voltage output of the power supply of the manufacturer, used to calibrate the sensor.

[6] `https://tempsens.com/blog/type-t-thermocouple`

- $U_{supply,real}$ is the measured (actual) voltage output of the power supply.
- $U_{out,max,ideal}$ is the voltage output of the sensor when P_{diff} = $P_{diff,max}$ and $U_{supply,real}$ = $U_{supply,ideal}$.
- $U_{out,max,real}$ is the maximum voltage output of the sensor using $U_{supply,real}$. The differential pressure associated with this voltage typically exceeds $P_{diff,max}$.

From these definitions, the $P_{diff,max}$, $U_{supply,ideal}$ and $U_{out,max,ideal}$ are provided by the manufacturer. An approximation of the offset of a sensor is also provided by the manufacturer, and usually a range (minimum, typical, maximum) is given. In practice, there are several factors that have an effect on the offset. The most notable are the warm-up shift ($\pm$ 5 mV), position sensitivity (orientation of the sensor, $\pm$ 5 mV) and long-term drift (material degradation, $\pm$ 5 mV). The magnitude of the offset uncertainty is different for each sensor. Because of this, the U_{off} is measured in the lab, as well as the $U_{supply,real}$, $U_{out,max,real}$ and the U_{out} during the experiments. The values can be acquired by applying pressure on the sensors, and calibrating the results with the other sensors. $U_{supply,real}$ is fixed at 5.1809 V on average. The uncertainties in the voltage outputs of the sensors are in the order of 10^{-3} V, so this will not have a significant effect on the results for the purpose of this study.

4.4. Data processing

The temperature control and measuring equipment are connected, controlled and processed by a combination of hardware (Section 4.4.1) and software (Section 4.4.2), which is elaborated on in this section.

4.4.1. Hardware

To process the signals from the thermocouples and the pressure sensors, the sensors are wired to several modules. For the thermocouples, the plus and minus wires are connected directly to a National Instruments (NI) 9214 module. The pressure sensors are connected to two NI 9215 modules, where the voltage output of the sensor is connected to the plus of the module, the ground output of the sensor is connected to the minus of the power supply, and the voltage supply of the sensor is connected to the plus of the power supply. The minus of the connections on the module is subsequently connected to the minus of the power supply. The minus of the power supply is grounded. The pressure sensor of the vacuum chamber is also connected to one of the slots of the NI 9215 module. The modules are plugged into the NI cDAQ 9178 chassis, which is connected to a computer to process the data read by the modules. The data is stored on the hard drive on the computer.

A complete overview of the setup and its wiring, can be found in the wiring diagram in appendix A.

4.4.2. Software

On the computer, the LabVIEW 2018 software is installed. In this software, a block diagram is created and the program stores the readings of the modules. During the experiments, a live visualization of the temperatures, voltages and differential pressures is provided. The stored data (as an Excel sheet in its final form) is then further processed using MATLAB R2022a, and can be provided by the author on request. MATLAB is used to convert the voltages, apply corrections to the data where necessary and subsequently visualize the data by plotting.

Voltage conversion

As mentioned in Section 4.1 and Section 4.3.2, the pressure sensors have an output in volt, so the voltage needs to be converted to (milli)bar in order to have meaningful data. The conversion of the vacuum chamber pressure is given by Equation 4.5 and is retrieved from the operating manual [7].

$$U_{chamber} = \frac{10}{6}(\log P + 3) \tag{4.5}$$

Where $U_{chamber}$ is in volt and P in mbar. Rewriting for pressure gives:

$$P = 10^{((U_{chamber}(\frac{6}{10}))-3)} \tag{4.6}$$

[7] http://www.hvg-verwertung.de/ebay/dokumentation/leybold/Messtechnik/TM20_PV20.pdf

The conversion of the pressure sensor output is given by Equation 4.7 and is determined and verified in the previous work by S. Sklavenitis [47]. $U_{out,max,ideal}$ and U_{off} were (re-)determined for this study. The parameters are explained in Section 4.3.2, and the uncertainty is discussed in Section 6.1.2.

$$P_{diff} = P_{diff,max} \frac{U_{out} - U_{off}}{U_{out,max,ideal} \frac{U_{supply,real}}{U_{supply,ideal}} - U_{off}} \tag{4.7}$$

Data manipulation
There are several causes for fluctuations of the data readings, namely:

- For the temperature sensors near the vent there can be a sudden, large decrease in temperature because of the ejected icy particles through the channel. These particles can touch the sensor, or accumulate and build up a channel of ice towards the top of the vacuum chamber (see Figure 4.4). Ice on top of the model can lower the overall temperature of the top of the model, but could also block the pressure sensor tubes. This behaviour can be easily seen in the acquired data, and could resolve itself without requiring manipulation with software in case the flow blow the ice from the sensor again. If this does not happen, the readings have become invalid.
- Sudden (very) large deviations in sensor readings could be caused by poor wire connections somewhere between the module and the model. A full disconnection (e.g. cable break) of the thermocouple results in extreme negative temperature values, which can be filtered with MATLAB. A poor connection between the thermocouple connectors (dirt, water) can result in unusually high temperatures, and the corresponding data reading have to be removed. When a pressure sensor tube is disconnected, the pressure sensor simply returns zero, so the readings have to be discarded. If there is a cable break of the sensor itself, the sensor returns strange voltage outputs and the wires will have to be re-soldered and tested.
- Inside the reservoir, the boiling and splashing of the water causes a periodic fluctuation of the sensor readings, for both temperature and pressure. The frequency is usually related to the bursting of the bubbles. These readings are not smoothed out, but taken into account: the temporary peaks have an effect on the flow inside the channel of the model, as will be explained in Chapter 6. When determining the readings in this case, the maximum and minimum value of the fluctuations are considered, and an average value is registered.
- Another cause is due to the sensor sensitivity. The pressure sensors from *All Sensors* and *First Sensor* have a large voltage output range for their measurements, and thus have a more stable output for the pressure ranges achieved in this study. The sensors from *Honeywell* have a smaller voltage output range, and operate close to their offset voltage, which results in larger fluctuations of the output data. This output is smoothed out in MATLAB.
- The last possible cause is liquid water being trapped inside pressure sensor tubes. If the liquid water is trapped in a water trap (see Chapter 6) and the tubes from the model to the water trap, and from the water trap to the sensor are clear, the vapor can move freely and the output of the pressure sensor is useful. But if this is not the case, the measurements are unreliable and the experiment will have to be redone. The readings are only slightly different from what they are supposed to be, but this cannot be manipulated with software because the exact deviation is not known.

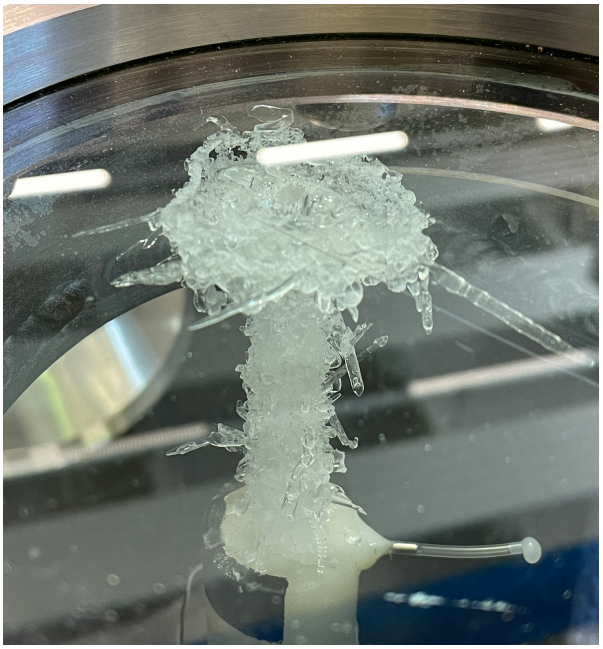

Figure 4.4: The buildup of an 'ice tunnel', when there is no decent splash screen present.

The data is smoothed using the standard settings of the *smoothdata* function in MATLAB. This function calculates the average of a certain subset of measurements, and this is repeated for the complete set of measurements. The amount of measurements taken for each subset is determined heuristically, and the function can handle large variations in data values. The function then returns a plot of the new, averaged data points. The data points are connected using a piecewise cubic hermite interpolating polynomial. The filtering of the statistical measurement outliers is done manually, by observing the individual readings of each sensor for each experiment.

5

Designing the new models

The first section describes the prior designs of this project, and the lessons learned from these designs along with their recommendations for further research (Section 5.1). The design choices for the new models are subsequently described in Section 5.2.1. How these models are made, and from what material, is explained in Section 5.3. A preliminary analysis of their performance is provided in Section 5.4.

5.1. Prior designs

Before coming up with a design for a new model to mimic the plumes of Enceladus, first the results of the previous design iterations will be thoroughly examined. The laboratory experiments recreating the icy moon's geysers can be seen as an ongoing project where the first design was made by T.J. Becx in 2018-2019, which will hereafter be called the ice model since it was made out of ice [50], see Section 5.1.1. The second and newest model was designed by T.M. Bründl and extended by S. Sklavenitis, who also conducted the experiments and analysis in 2021-2022 [47]. The model was made out of plexiglass and thus will be named the plexiglass model hereafter, see Section 5.1.2. Each model has its conclusions and recommendations for future research, and relevant considerations for the new design iterations are summarized in Section 5.1.3.

5.1.1. The ice model

This model was designed to recreate the plumes of Enceladus in the available facilities of the FH Aachen University of Applied Sciences. To achieve this, first a small scale model was developed and tested in a vacuum chamber at the TU Delft. The results of this experiment led to the proposal of a larger model which would fit in the vacuum chamber at the FH Aachen. The design was driven by the ice layer and liquid ocean of Enceladus. The physical characteristics of the model were based on the relations between the throat and vent area (see Chapter 3), and so a supersonic nozzle-like structure was created in order to reach the plume exhaust velocities observed by Cassini. The model was made by pouring water into a mould, freezing this water and removing the mould once frozen. A picture of the setup can be seen in Figure 5.1.

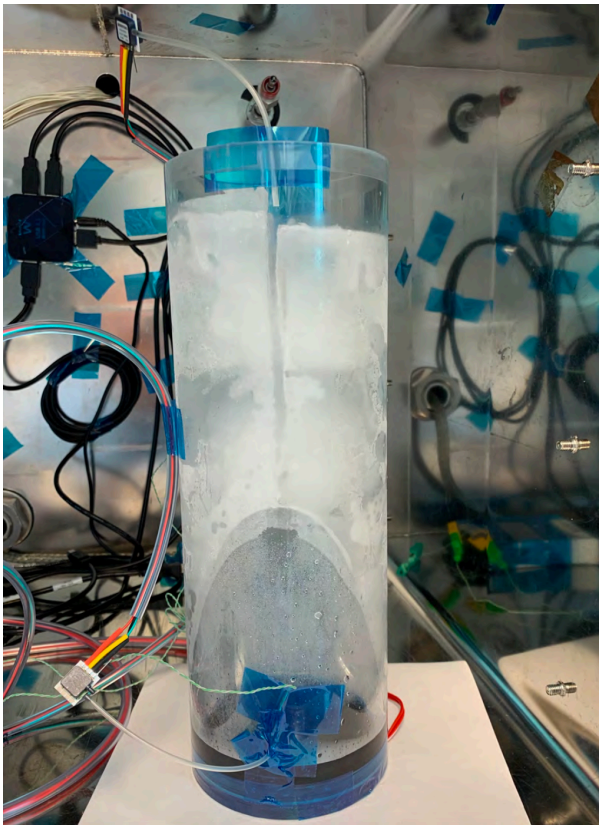

Figure 5.1: The setup of the (small) ice model in a vacuum chamber, including sensors and heating foils [50].

The vacuum chamber at FH Aachen is large (1.0 m diameter, 1.9 m height) and can reach internal pressures as low as 8 Pa without gas ballast and 70 Pa with gas ballast. In this study, however, the larger model was not actually tested inside this vacuum chamber, although the initial calculations of the models were based on these pressures. The smaller model has a length of 300 mm, diameter of 100 mm, and both the reservoir and channel have a length of 150 mm. The reservoir volume is about 2.356 cm^3 and weighed about 2.2 kg when filled with ice. The temperatures were measured using 2 K-type thermocouples, and the pressures were measured using 2 relative pressure sensors and an absolute pressure sensor. The vacuum pump used for the smaller model in Delft could not reach much lower pressures than 500 Pa. The results from this test setup led to the following recommendations:

- Any moulds used should be made out of metal to make them easily removable.
- The water reservoir should be heated, in order to prevent freezing of the water in the reservoir.
- The lowest measured pressure of around 500 Pa in the vacuum chamber resulted in (roughly) estimated plume velocities of 49-106 m/s, where at least 100 Pa would be required to reach supersonic plumes.

So the suggested larger setup should have the following properties and characteristics:

- The model should have heated metal moulds, since using wrapped cling foil causes wrinkles in the ice and changes the shape, and is difficult to remove.
- A heated reservoir. The channel did not freeze due to the plumes.
- Advisable to have all sides of the model covered with ice (instead of plexiglass), since the wall temperature also plays a role for grain growth [40], as well as the wall roughness.
- If the grain growth is studied, the channel could be longer and the reservoir smaller, if the size of the boiling chamber/reservoir is studied, the channel could be shortened and the reservoir volume increased. Reservoir volume also directly influences the runtime of the experiment due to the evaporation of reservoir water.
- The suggested design specifications for the larger model can be found in the Becx' thesis [50].

5.1.2. The plexiglass model

Experiments with the plexiglass model have been conducted using two different configurations: the small setup (see Figure 5.2a and the large setup (see Figure 5.2b). The small setup consists of a small reservoir with 3 heating foils installed at the bottom, and a nozzle above. Because of the small volume, the liquid inside the reservoir evaporates quickly and the boiling liquid could reach the sensors, making the readings invalid. To prevent this, and to create a higher pressure difference by adding more heating foils on a larger reservoir area, an enlargement of the reservoir has been added at a later stage: the large setup. Because of the higher pressure difference, higher Mach numbers can be reached. Besides, more heating foils were required in order to prevent freezing of the liquid surface water. The model and the reservoir are made completely out of plexiglass, and the top part (so the small reservoir and the nozzle) is 200 mm long, and the bottom part (the large reservoir) is 220 mm long. The top part has an external diameter of 74 mm and the bottom part has an external diameter of 185 mm. The nozzle has a conical shape with a throat diameter of 6 mm and a vent diameter of 7.9 mm, and the expansion ratio is 1.7336. The large reservoir has a capacity of 5.051 L. The physical characteristics were based on the isentropic relations. The technical drawing of the small model can be found in can be found in appendix B, and the technical drawing of the reservoir in appendix D[47].

(a) The small plexiglass setup [47].

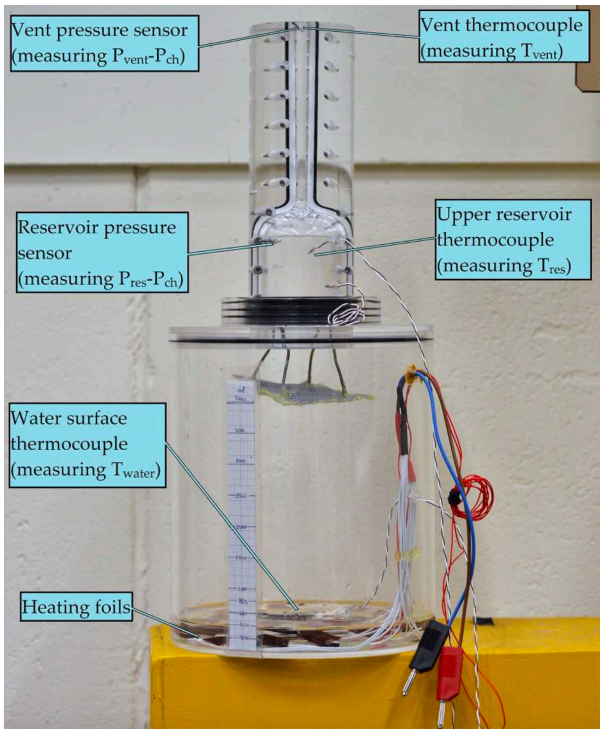

(b) The large plexiglass setup, including the placement of sensors and heating foils [47].

Figure 5.2: In the left figure, the small test setup can be seen. In the figure on the right is the model placed on top of the larger reservoir.

The vacuum chamber used for the experiments is the Hypersonic Test Facility Delft (HTFD) at the High Speed Lab (see Section 4.1). The minimum pressure measured during the study was 0.78 ± 0.12 mbar [47]. The water in the large reservoir is heated by 12 small heating foils, and one larger heating foil (see Section 4.2.2). At the top part, two T-type thermocouples are installed to measure the temperature at the vent and small reservoir (see Section 4.3.1), and two differential pressure sensors are installed to measure the pressure at the vent and the reservoir (see Section 4.3.2). An additional floating thermocouple has been added to the larger reservoir to measure the temperature of the water surface.

5.1.3. Considerations for a new model design

The lessons learned and corresponding recommendations of the ice model and the plexiglass model have been summarized and listed below. The recommendations will be taken into account for the new design.

The ice model

Proposed topics for further research following from the study of the ice model are as follows [50]:

- It might be useful to have a larger mass flow than proposed in this thesis for future experiments, and to consider the practical limitations of the experiment: e.g. the required pressure in order to reach a certain exhaust velocity.
- The study suggests a slight change in channel geometry is required when ammonia is added to the reservoir, in order to reach the desired plume exhaust velocity. Therefore, a study on the effect of the observed elements in the plume (mainly salts) on the triple point is recommended, as these would affect the 'required' channel geometry.
- It is doubtful that grains can grow in the relatively small designs proposed in this study, but growth could be studied when smaller nucleation particles with a known composition and size are placed inside the reservoir, and their size (and possibly composition) can be compared to the original particles when they are expelled.
- An analysis is desirable to determine whether a grain growth study is feasible for such a short channel length, since on Enceladus the grain growth is partially stimulated by wall collisions on the way to the vent [40].
- Having an irregular wall shape allows for more collisions and thus more grain growth. Future experiments could therefore have irregular walls, with minimum and maximum openings set by the throat-to-vent ratio.
- Additional research can be done to study the effects of: boiling chamber volume, channel length and the effects of gravity, as some of the heavier molecules might not reach Cassini's lowest flyby altitude and were therefore not discovered, although this could also be attributed to the fragmentation of molecules due to radiation.
- More advanced topics for future research include: Adding an ionization source to create charged particles and study the effects on the ejected particles, in case the water used in the experiments consists of more plume constituents than water. This could be used to study the effect of charged particles on the plume characteristics. Complex organic molecules or bacteria could be added to the water, to determine their presence in the plumes. The impact ionization of Cassini's CDA instrument fragments the molecules, and this way a study can be conducted on the molecules before they break.

The plexiglass model

The lessons learned from this experiment, along with relevant recommendations and implications for further research are listed below [47]. The relevant results in terms of pressure and temperature measurements are provided in Section 6.2.3, where they are compared to the results of this study.

Lessons learned

- The mass flow rate through the nozzle is mainly driven by the heat supplied to the water in the reservoir. More heat supplied means a larger mass flow rate. The water temperature and pressure in the reservoir can also be controlled by the heating power, to a limited extent.
- Besides the heat supplied by heating foils, heat comes from other sources too: it is expected that the plexiglass provides energy to the water in the reservoir via convection, and that energy comes from the vacuum chamber walls via thermal radiation. The plexiglass itself is also heated by the metal floor of the vacuum chamber, and the created plume gases. This is difficult to quantify due to the many variables involved. The heat supplied by external sources seems to decrease with boiling time.
- The flow of vapor becomes choked in the nozzle almost immediately after boiling. The water surface temperature responds with a delay to the increasing reservoir pressure after boiling.

- The critical mass flow rate equation systematically overestimates the mass flow rate by 32%$\pm$10%. This is expected to be caused by thermal choking in the nozzle, due to the heat release of condensing gas. The thermal throat is narrower than the geometrical throat. The size of this thermal throat is either independent from, or changing very slowly with respect to the mass flow rate. With heating power supplied, the thermal throat is slightly smaller than without heating foils. There seems to be condensing vapor already before the geometrical throat. The condensed water particles travel faster than the vapor and do not completely vaporize before reaching the vent.
- It is not clear yet whether the created plumes are supersonic: pressure measurements suggest a Mach number above 1, but temperature measurements suggest significant heat exchanges in the model, making the isentropic assumptions invalid. The vapor leaving the vent is unsaturated and has a higher temperature than the water in the reservoir, also suggesting subsonic conditions.
- Particle Image Velocimetry revealed ejected particles with speeds up to 426$\pm$5 m/s, meaning that supersonic speeds have been reached. However, the most common observed speeds were between 120-200 m/s, meaning that the flow is most likely subsonic. Particles with Mach numbers above 1 prove that the flow is choked (possibly thermally) and that there must be a supersonic expansion section in the nozzle, even with a subsonic outflow.

Recommendations for future research

- In order to avoid thermal choking, a study could be performed on how rapidly the nozzle should expand. The degree of (super)saturation and the temperature required to cause thermal choking could be studied. The effects of changing the nozzle geometry or removing heat from the flow could also be studied.
- An analysis on the effect of active cooling of the walls of the experiment and the thermal gradients along the ice shell of Enceladus is therefore desired. A narrower, cold wall can effectively cool the expelled vapor.
- An analysis on the effect of the condensed mass fraction on the Mach number and the choking point is desired, although this depends on the geometry of the setup. Testing setups with different geometries could provide insights into these effects.
- More sensors could be placed along the nozzle, to give more insight in the thermodynamic process that drives the vapor flow. The nozzle could also be extended, so that condensed particles have more time to vaporize before reaching the vent.
- Schlieren imaging could show if the plume is supersonic or not, by visualizing the flow and revealing possible shockwaves. This would require a transparent model and specific optics components, including sufficient space in the test section.

5.2. Design choices

This section discusses the geometry and material of the new model designs (Section 5.2.1), and their expected qualitative results (Section 5.2.2).

The main focus areas for a possible solution for a new design iteration from Section 5.1.3 are as follows:

- The model should include more points where the temperature and pressure are measured along the channel. This is done to give more insight into what is actually happening inside the channel, i.e. to acquire evidence for any thermodynamic phenomena. The measurement points should be equidistant to get an accurate progression through the channel, and not obstruct the flow.
- The previous experiments indicated that there are significant heat exchanges along the flow with the environment and model itself, which would mean that the isentropic assumption is no longer valid. The heat exchanges should be studied in more detail, for which there are three options (assuming that there are more measurement points w.r.t. the previous experiments):

    1. Different channel geometries should be considered, to study how heat exchanges depend on the geometry. Examples include (but are not limited to): the section where condensation occurs and a possible location of a thermal throat due to the latent heat release, the presence of any shockwaves, the necessity of a geometrical throat and more. Options for different channel geometries include: increase in model length, removal of a geometrical throat (straight

or converging/diverging channel), different throat to vent ratio, different throat diameter and a different expansion angle.
2. Cooling the model should reduce the heat addition to the flow, which should affect the location of a thermal throat (if still present), and condensation.
3. Using a different material for the setup. The heat exchanges are also depending on the material properties, so using different materials coould shed light on the heat exchanges present in the setup. The material used for this model should be able to withstand freezing.

Other considerations include:

- The effects of tides play a large role on the plume formation on Enceladus, because of the generated currents, backpressure and heat generated due to wall friction. Replicating this is difficult with the used setup and is beyond the scope of this study. It is however taken into account when determining the implications for Enceladus (Chapter 7).
- The existence of a large subsurface reservoir on Enceladus is debatable, as discussed in Chapter 2. A reservoir with a larger water surface with pressurized gas above would mean that there is a larger evaporating surface area, larger mass flow and a larger pressure difference w.r.t. the vacuum chamber. Both options (with/without reservoir) are considered.

5.2.1. Geometry and material

In this section, the different models, the goal of the models, their geometry and their material are described. Besides the plexiglass model, 6 additional models have been created for this study. Experiments have been conducted will all 7 models. The following models have been studied:

Plexiglass model

The plexiglass model is the same model used in the previous study (as described in Section 5.1), except that 5 additional holes have been drilled for extra pressure sensor measurements. The additional pressure sensor readings give a more accurate progression of the pressure along the channel. The specifications of the plexiglass model were already described in Section 5.1.2, and are repeated in the summary below. The CAD model can be found in appendix B [47]. This model serves as the baseline for the other models, as either 1 or 2 of its properties are changed w.r.t. the other models, in order to observe the effects of this change.

- Material: Plexiglass
- Channel type: Converging-diverging
- Total length: 200 mm
- Throat-vent length: 120 mm
- Inlet: 49.2 mm
- Throat: 6.0 mm
- Vent: 7.9 mm
- Vent-to-throat area ratio: 1.734
- Converging angle (inlet-throat): - (curved funnel shape)
- Expansion angle (throat-vent): 0.906°

Model 1 - the narrower converging/diverging channel

The first model is a converging-diverging model, and has a longer channel (245 mm) and approximately the same expansion angle as the plexiglass model. It therefore has a larger vent diameter w.r.t. the plexiglass model, because the model is longer. The throat size is however decreased w.r.t. the plexiglass model: mainly due to the printing process (see Section 5.3). The model is made out of polylactic acid, or PLA, which will be further described in Section 5.3. It should be noted that for the PLA models, there is a significant difference between the dimensions of the CAD model and the actual model, due to the manufacturing process. The dimensions shown in this section are the accurately measured dimensions of the final model. This model is used to study the effects of a smaller throat size and an increase in channel length without changing the expansion angle. Model 1 has the following characteristics:

- Material: PLA

- Channel type: Converging-diverging
- Total length: 245 mm
- Throat-vent length: 175 mm
- Inlet: 6.2 mm
- Throat: 5.3 mm
- Vent: 8.2 mm
- Vent-to-throat area ratio: 2.394
- Converging angle (inlet-throat): 0.737°
- Expansion angle (throat-vent): 0.949°

The CAD model of the *outside* of this model can be found in appendix C. The outer dimensions of all the new models are equal to the model depicted in appendix C, however the channel of the model shown in appendix C is straight (model 4, which is shown below), but is different for each model. The holes in the walls of the model are measurement points, and will be further described in Section 5.3.

Model 2 - the wider converging/diverging channel
This model is essentially model 1, but with an increase in channel width along the whole channel. This implies that the expansion angle remains the same as model 1, although there is a small deviation in the expansion angle due to the manufacturing process inaccuracy. The model is therefore used to study the effects of the channel width. The model has the following characteristics:

- Material: PLA
- Channel type: Converging-diverging
- Total length: 245 mm
- Throat-vent length: 175 mm
- Inlet: 7.4 mm
- Throat: 6.3 mm
- Vent: 9.1 mm
- Vent-to-throat area ratio: 2.086
- Converging angle (inlet-throat): 0.90°
- Expansion angle (throat-vent): 0.917°

Model 3 - the longer straight channel
This model has a straight channel, and is extended (390 mm instead of 245 mm length) so that the water level is higher than the inlet of the channel. This results in a small evaporating area of 22.06 mm^2. It is used to replicate controlled boiling, a theory of the origin of the plumes as described in Chapter 2. Preliminary tests with simple off-the-shelf models have revealed that the model needs a modification to let the remaining air from the reservoir out during the evacuation of the chamber. If this is not present, the water will simply be sucked out from the reservoir through the channel due to the lower pressure in the chamber. To solve this issue, a one-way check valve is attached to the model, as shown in Figure 5.3. This valve will force the overpressure in the reservoir out through the channel into the vacuum chamber, until the pressure starts increasing inside the channel from the evaporating and boiling water in the channel itself. This pressure should then block the check valve to prevent the flow of vapor from flowing back to the reservoir, and an equilibrium is then achieved. The model has the following characteristics:

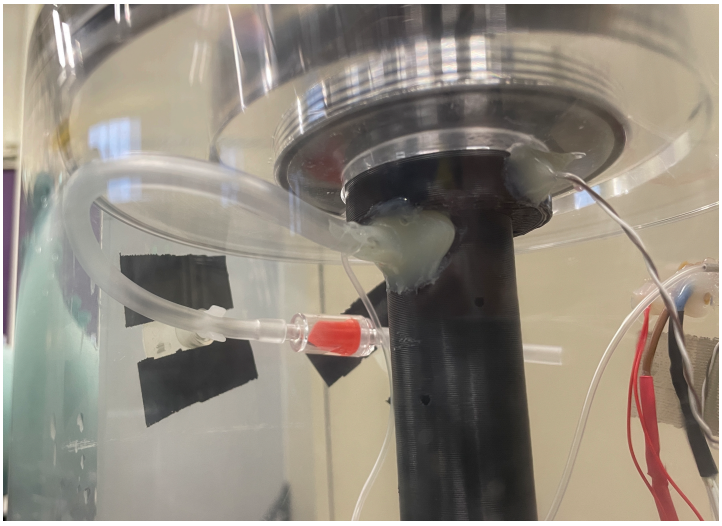

Figure 5.3: Model 3 with the check valve attached.

- Material: PLA
- Channel type: Straight
- Total length: 390 mm
- Throat-vent length: -
- Inlet: 5.3 mm
- Throat: -
- Vent: 5.3 mm
- Vent-to-throat area ratio: 1
- Converging angle (inlet-throat): 0°
- Expansion angle (throat-vent): 0°

Model 4 - the shorter straight channel
This model also has a straight channel, and has the same (outer) dimensions as the models 1, 2, 5 and 6. The channel diameter is a bit larger w.r.t. model 3 (6.3 mm vs 5.3 mm) and inlet of the model is not below the water level anymore, so that a direct comparison can be made with the other models. The main difference between this model and model 3 (besides the dimensions), is that the pressure in the reservoir will be much higher, which could give an insight into whether a pressurized chamber is necessary in order to recreate the plumes of Enceladus. It has the following characteristics:

- Material: PLA
- Channel type: Straight
- Total length: 245 mm
- Throat-vent length: -
- Inlet: 6.3 mm
- Throat: -
- Vent: 6.3 mm
- Vent-to-throat area ratio: 1
- Converging angle (inlet-throat): 0°
- Expansion angle (throat-vent): 0°

Model 5 - increased channel length and different material w.r.t. plexiglass model
This model has the same vent and throat diameter as the plexiglass model, and is made out of a different material: polypropylene. This is done so that the model can also be tested after freezing the model, see Section 5.3. Besides the difference in material, the model is longer than the plexiglass model, so a comparison can be made with a model with the same vent to throat area ratio but with

increased length. Because of this same ratio and the greater length, the expansion angle naturally becomes lower. The goal of this model is therefore to observe the effects of the increased channel length, and to assist translating the plexiglass model to the new models because of their similar outer dimensions. The model has the following characteristics:

- Material: PP
- Channel type: Converging-diverging
- Total length: 245 mm
- Throat-vent length: 175 mm
- Inlet: 6.7 mm
- Throat: 6.0 mm
- Vent: 7.9 mm
- Vent-to-throat area ratio: 1.734
- Converging angle (inlet-throat): 0.573°
- Expansion angle (throat-vent): 0.622°

Model 6 - the diverging channel
This model has a channel that is only diverging, and is included to study the effects of a fully tapered channel without having a preceding converging section. The inlet diameter is equal to the throat diameter of the plexiglass model and model 5, and since there is a pressurized chamber beneath the model, the inlet acts essentially as a throat. The model has a larger expansion angle, and a longer channel. The model is used to observe if there are any signs of grain formation when there is a longer expanding section, and to study the effects on the heat exchanges when having a larger expansion angle. It has the following characteristics:

- Material: PLA
- Channel type: Diverging
- Total length: 245 mm
- Throat-vent length: -
- Inlet: 6.0 mm
- Throat: -
- Vent: 16.6 mm
- Vent-to-throat area ratio: -
- Converging angle (inlet-throat): -
- Expansion angle (throat-vent): 2.479°

Reservoir
The reservoir from the previous experiments with the plexiglass model, described in Section 5.1, will be reused in this study. The above models are therefore designed to fit on top of this reservoir, and the connection is made airtight using rubber O-rings. The heating foil configuration also remains unchanged, although the maximum power throughput (and thus the maximum heating capacity) has been increased for this study. The dimensions of the reservoir can be found in the CAD drawing in appendix D [47]. For completeness, the model characteristics have been summarized and can be seen in Table 5.1 below. A schematic overview of all the models can be seen in Figure 5.4.

Table 5.1: Overview of the model characteristics.

Model	Plexiglass	1	2	3	4	5	6
Material	Plexiglass	PLA	PLA	PLA	PLA	PP	PLA
Channel type	Con.-Div.	Con.-Div.	Con.-Div.	Straight	Straight	Con.-Div.	Diverging
Total length [mm]	200	245	245	390	245	245	245
Throat-vent length [mm]	120	175	175	-	-	175	-
Inlet diameter [mm]	(49.2)	6.2	7.4	5.3	6.3	6.7	6.0
Throat diameter [mm]	6.0	5.3	6.3	-	-	6.0	-
Vent diameter [mm]	7.9	8.2	9.1	5.3	6.3	7.9	16.6
Vent-throat area ratio	1.734	2.394	2.086	1	1	1.734	-
Expansion angle [deg]	0.906	0.949	0.917	0	0	0.622	2.479
Converging angle [deg]	-	0.737	0.90	0	0	0.573	-

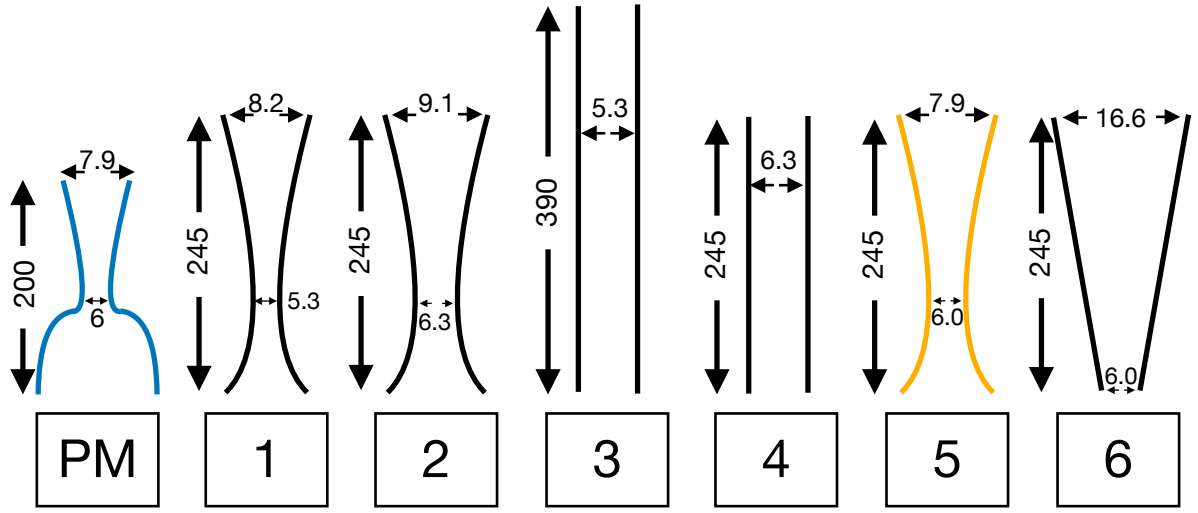

Figure 5.4: Schematic overview of all models used in this study. Dimensions are given in mm. Not to scale.

Dimensional limitations

It should be noted here that the dimensions of the above models are limited by the size of the test section. A similar ratio of the assumed channel length and width (of Enceladus' crevasses) used in the simulations of the articles on the plume mechanisms from Chapter 2 cannot be recreated in the lab. For example, the open model from Rubin & Kite (described in Chapter 2) suggests a water table of approximately 3.5 km below the surface, and a (straight) channel diameter between 1 and 5 meters, because any diameter smaller than 1 meter would close the channel by freezing, and any larger than 5 meters would narrow it down over time due to ice accumulation [20]. And thus, even when taking the widest possible channel width of 5 meters, having the same width/length ratio as the article would result in a channel diameter of only 0.35 mm in the lab with a model length of 245 mm. In part 1 of the controlled boiling model from Nakajima and Ingersoll (also described in Chapter 2), the simulations are conducted assuming 50 - 100 mm channel diameters over a channel depth between 1.5 and 4.5 km [29]. Again when taking the largest width/length ratio option, this would result in a channel diameter of only 0.02 mm on a vacuum chamber scale. Part 2 of the article of the same authors suggests a water depth of about 2 km, with a tapered channel from 1 m at the liquid-gas interface to 0.05 - 0.1 m at the vent, which again results in microscopic channel diameters in the lab [30]. The numerical simulation from Yeoh et al. in 2017 comes closest to having width/length ratios usable in the lab, with a channel length of 45 m, a vent diameter of 2.8 m, a first throat diameter of 0.46 m and a second throat 'slightly larger than the first throat' [51]. This translates to a vent diameter of 15.25 mm and a (first) throat diameter of 2.5 mm in the vacuum chamber. The above models have channel or throat

diameters larger than described here, which would be equivalent to cutting away part of the channel if the width/length ratios from the articles were used for the same diameters as the models.

5.2.2. Expected results

The expected (qualitative) results of each model are listed below.

Plexiglass model
The goal of the plexiglass model is to establish the baseline, and to reproduce the results from the previous study. These are expected to be similar, however the initial conditions have changed since then. The largest contributors to the change in these initial conditions are due to the fact that the experiments were conducted in a different season (different room temperature) and the performance of the vacuum pumps deteriorates with time, unless they have had their periodic revision (more about this in Chapter 6). The additional pressure sensor readings could result in the confirmation or debunking of certain hypotheses from Section 5.1.3.

Model 1 - the narrower converging/diverging channel
It is expected that the smaller throat size will decrease the mass flow, because the choked mass flow depends on the (throat) area as shown in Chapter 3. Because of the lower mass flow and narrower/longer channel, the heat addition to the flow from the environment and model is expected to be higher, which may cause a thermal throat, or move the thermal throat upstream of the channel (assuming the flow becomes supersonic at the geometrical throat). Because of the higher vent-to-throat area ratio w.r.t. the plexiglass model, it is expected that higher Mach numbers can be achieved, but this would depend on the effects of the heat exchanges along the channel.

Model 2 - the wider converging/diverging channel
The throat diameter is increased by 1 mm w.r.t. model 1, so the (choked) mass flow should increase and other effects such as backpressure from friction should relatively decrease. The vent-to-throat area ratio is decreased, so the Mach number at the vent should be lower than model 1, but still higher than the plexiglass model. Because of the wider channel/larger mass flow, the heat addition to the flow from the environment should be relatively lower, which could trigger condensation more upstream in the channel due to the shift to the left in the phase diagram (no change in pressure, but lower temperature).

Model 3 - the longer straight channel
Due to the straight channel, a thermal throat has to be present in order to achieve supersonic velocities. If this throat is not present, the flow will accelerate until Mach 1 at the vent, and then expand into a vacuum which would make the flow supersonic after the vent. The pressure and temperature gradient are measured along the channel, but what happens outside the channel can only be confirmed using techniques such as Schlieren imaging or particle image velocimetry, which are not used in this study. It is expected that due to the narrow channel, heat exchanges will occur along this (longer) channel, so that a thermal throat can form and supersonic velocities can eventually be reached if sufficient heat is provided.

Model 4 - the shorter straight channel
Because of the smaller channel diameter w.r.t. model 3, the reservoir pressure will be higher, which could give insight into the necessity of a pressurized chamber. This pressurized chamber is a theory that is also challenged in multiple articles, as described in Chapter 2. A pressurized chamber has a large effect on the pressure ratio along the channel, which in turn determines the Mach number at the vent. Here it is also expected that a thermal throat will be formed, so that the flow reaches supersonic velocities. The model will also be used to make an estimation of the heat addition to the flow and the influence of the friction of the walls. These can be quantified by using the Rayleigh and Fanno flow equations from Chapter 2 (which are valid for a straight channel) and comparing the results to other models.

Model 5 - increased channel length and different material w.r.t. plexiglass model
Because the Mach number is determined by the vent to throat area ratio, and this ratio is equal to the vent/throat ratio of the plexiglass model, the Mach number at the vent should be the same. It is expected

however that this will not be the case: due to the increased length, the effect of the heat addition from the walls will be greater w.r.t. the plexiglass model. The additional heat will move the sonic point more downstream of the throat, or, move a thermal throat (if present) more upstream. Either way, the result will be a lower Mach number at the vent than for the plexiglass model, because the additional heat will decrease the Mach number for supersonic flow. It is also taken into account that the model is made out of a different material, which results in a different friction coefficient which in turn has an effect on the backpressure of the flow. The different material can also give insight into the heat supplied by external sources, as this could differ from the other materials.

Model 6 - the diverging channel
The model has a larger expansion angle, and a longer channel section where solid particles could nucleate. In case there were any shockwaves in the channel during the prior experiments with the plexiglass model to explain the increase in temperature or pressure along the channel, the larger expansion angle and additional measurement points of this model could reveal if this is possible to occur in the used setup. It is however not expected that this would happen, because the expansion angle is still low. It is also unlikely that if there are no shockwaves inside this model, that they would be present in the other models, although the presence of condensation shocks (or thermal choking) cannot be ruled out by this theory. It is expected that the largest Mach numbers can be achieved by this model, reaching Mach numbers of nearly 3.5 given sufficient upstream pressure, assuming isentropic conditions and the inlet acting as a throat. This model could also be used to study the theory of the flow becoming sonic at the vent, and turning supersonic when expanding into a vacuum. This is plausible for both Enceladus and the experimental setup, where the setup would require sufficient reservoir pressure (reach the critical pressure ratio), and that it is also assumed that the inlet of the model would be the analogue for the vent of the icy channel of Enceladus.

5.3. Material and manufacturing process

As already briefly mentioned in Section 5.2.1, the new model designs are made out of polypropylene and polylactic acid, and the properties of these materials are described in Section 5.3.1. Printing the models is done by using different 3D printing techniques, which are described in Section 5.3.2.

5.3.1. Material properties

These PP and PLA have been selected because of their toughness, very low flexibility, water resistance, their manufacturability and their cost effectiveness. The polypropylene also has good thermal shock resistance (no deformations under large temperature variations). A transparent material for the models (like the plexiglass model) would have been considered as a bonus, but this is not the case because PLA and PP have black and beige colors.

Polypropylene is a common material for household items, such as plastic containers, trash cans, plastic bottles and more. The polypropylene has a better thermal shock resistance because of its internal structure, which is different from the PLA. Polypropylene is a polymer with a semi-crystalline structure, whereas polylactid acid has an amorphous structure, see Figure 5.5. However, for the temperature ranges explored in our experiments, the benefit of the better thermal shock resistance is negligible. It does serve another purpose: because of the semi-crystalline structure, the PP model with a solid internal structure is better capable of storing internal energy, unlike the hollow structure of the PLA models as will be explained below. This makes the PP model better suited for the experiments with a cooled model.

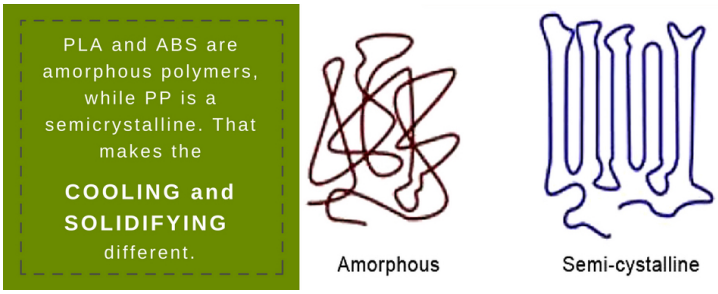

Figure 5.5: Schematic overview of model 3.[1]

5.3.2. Printing process

The hollow structure from the PLA model comes from the printing method: which is Fused Deposition Modelling or FDM. FDM is the 'common' 3D printing technique, used for general purposes and is also the printing technique of most household 3D printers. FDM is a layer-by-layer printing technique, see Figure 5.6. The PLA is squeezed through a heated nozzle, then prints a layer which is pre-defined by a 3D slicing software, this layer then cools and solidifies, and a next layer is printed on top of the previous layer. This process is repeated until the print is finished. To save both material and time, the slicing software creates a hollow interior with a fortifying inner structure, and prints additional material near surface areas (including the holes from the measurement points). This is done so that the model is still airtight and the measurements during the experiments are not compromised. To prevent the model from falling, support material is printed as well and is removed when the printing is finished. The PLA models are printed at the TU Delft Aerospace Engineering faculty, and one of the final products can be seen on the left of Figure 5.7. The outer dimensions could be printed with decent accuracy (less than 0.1 mm deviation), although the smaller the channel dimensions get, the worse the printing accuracy becomes (up to a 0.7 mm difference, which is a lot for the throat). The offset in printing accuracy changes when the print differs, but remains the same for identical prints. The CAD models have been adjusted to account for the printing inaccuracy by adding a pre-defined deviation, and the final, printed dimensions have already been summarized in Table 5.1.

[1] https://www.lpfrg.com/guides/3d-printing-polypropylene/

Figure 5.6: 3D printing of the PLA models at the TU Delft AE faculty.

Model 5 is the only model printed out of polypropylene. It is more difficult to print than PLA, and requires a more sophisticated printing method. The method used for this model is Selective Laser Sintering, or SLS. SLS works as follows[2]: a layer of powdered polypropylene is spread across a building platform, and a strong laser melts specific areas of the powder. The powder is fused together and a new layer of powder is added on top, and the process is repeated until the print is finished. SLS does not require support material, and the remaining powder can be reused. SLS can print with high accuracy, and the deviations from the CAD model are in the order of 10^{-2} mm. The print has a solid internal structure, and can be seen on the right of Figure 5.7. The model is printed by Ricoh's 3D printing facilities in the UK, and shipped to the Netherlands.

On the printed PP model, the glued metal tubes can be seen. When the models were printed, 22 holes were drilled in each model. The holes were partially included in the CAD model, and were manually drilled out to prevent curved edges. The 22 holes are placed as follows: there are 11 holes for both the temperature and pressure sensors along the channel on one side, and 11 other holes on the opposites side. The holes are equidistant, and have a small angular displacement to prevent disturbance of the airflow (see Figure 5.7). A long metal tube has been cut into 11 small tubes for each model, and sanded on the sides to remove the sharp edges. The small tubes are glued into place, and are used to connect the pressure sensors using a plastic tube. The full setup can be seen in Figure 5.8. The unused pressure sensor openings are closed using the small tubes with glued ends, and the attached pressure sensor tubes which are used for an experiment have water traps installed in order to prevent water from entering the pressure sensor. The thermocouple wires are also glued into place before an experiment (see Section 6.1).

[2] https://rapidfab.ricoh-europe.com/technologies/selective-laser-sintering/

Figure 5.7: On the left, an example of one of the 5 3D printed PLA models, and on the right the 3D printed PP model where the metal tubes are glued in place. On the opposite side of the metal tubes are drilled holes, which are difficult to see.

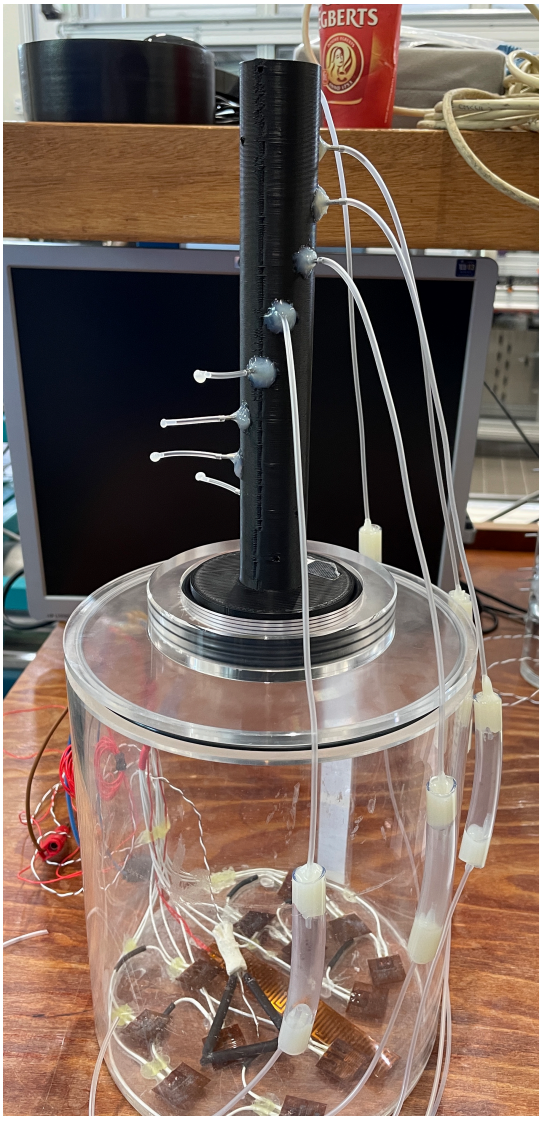

Figure 5.8: Overview of the complete setup.

5.4. Theoretical performance analysis

To assess the theoretical performance of the new designs, a distinction has been made between two channel types: the converging-diverging channel and the straight channel. For the converging-diverging channel, the analysis has been done with the dimensions of model 5, which has the same vent to throat area ratio as the plexiglass model. For the straight channel, the dimensions of model 4 are used. The outcome gives a quantitative indication of the expected results for the experiments. The results shown in this section are solely based on the geometry of the channel and different assumptions made, and are not based on any measurements.

5.4.1. Converging-diverging channel

The conclusions from Sklavenitis' study presented in Section 5.1 have shown that the flow in the channel is not fully isentropic, mainly due to the heat addition. Heat addition, friction and possibly shockwaves cause a change in entropy, making the isentropic relations invalid. However, if the flow becomes supersonic in the channel, the vapor will spend only 0.6 milliseconds (at most - for M = 1) inside the channel of one of the models. It is questionable that so much heat can be exchanged in such a short time frame. So despite the deviation of the results from the isentropic relations, the isentropic relations are still used in order to have a first approximation of the flow parameters of the models. From Chapter 3 we know the effects of heat exchanges and friction on the flow parameters, which is taken into account when analyzing the experimental data. A first order approximation of the heat term and friction term from the Rayleigh- and Fanno flow relations for a straight channel is provided in Section 5.4.2.

Isentropic expansion ratios

The isentropic relations from Chapter 3 are used to visualize the theoretical Mach number and the pressure- , density- and temperature ratios along the channel. These ratios only depend on the geometry of the channel and are not (yet) based on measurements. The Mach number is determined by the ratio of the cross sectional area along a point in the channel and the cross sectional area of the geometrical throat. The pressure-, density- and temperature ratios are subsequently calculated using this Mach number. The expansion ratios and Mach number are in the top plot of Figure 5.9. The absolute pressure and temperature - derived from the Mach number - is the bottom plot of the same figure. The temperature and pressure plot require an initial guess for the reservoir temperature and pressure, and these have been (arbitrarily) set at T = 0.01°C (triple point temperature), 15°C and 30°C for the temperature, and at P = 6.117 mbar, 12.234 mbar and 18.351 mbar for the pressure, which are 1, 2 and 3 times the triple point pressure.

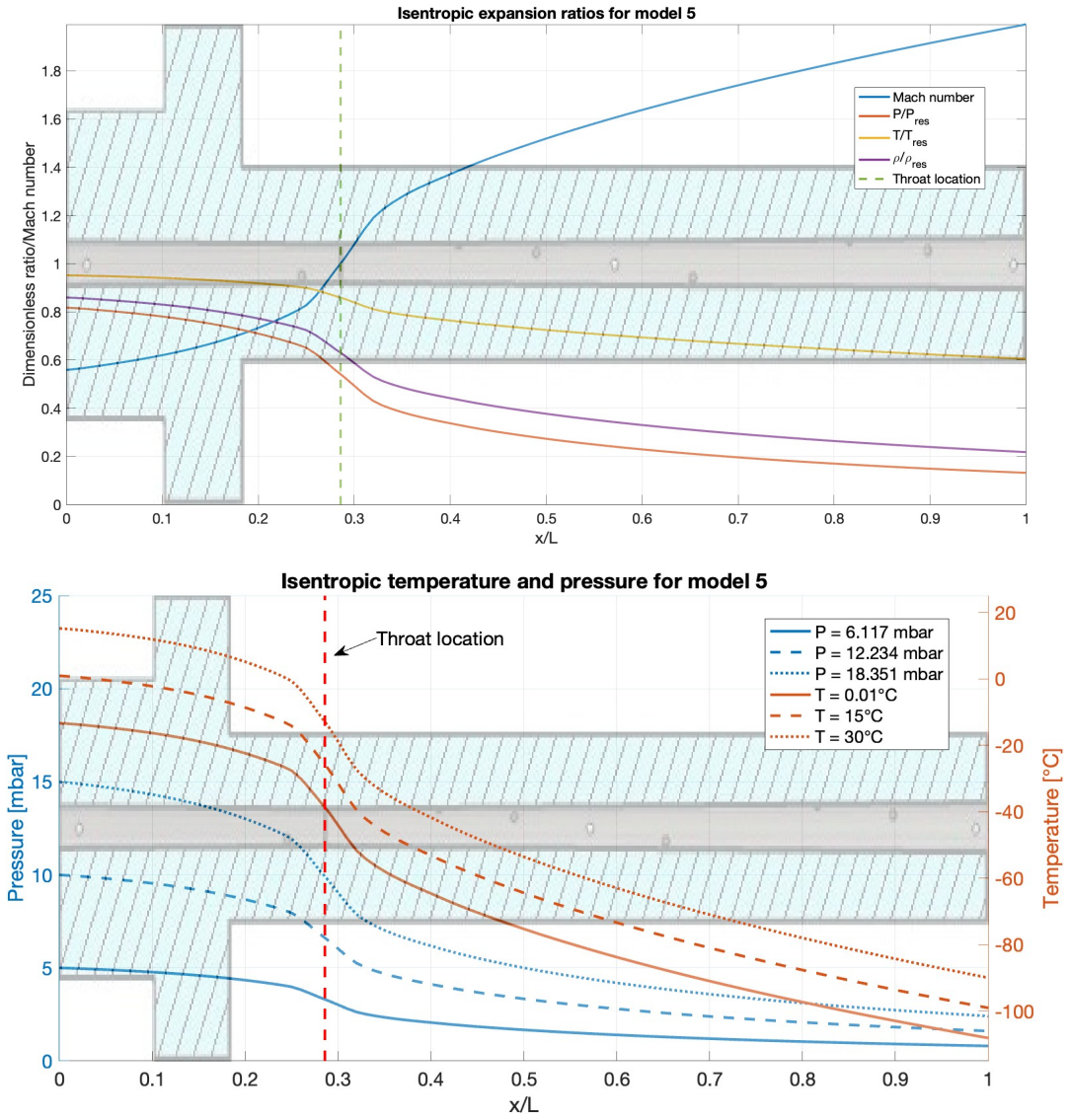

Figure 5.9: Top figure: the isentropic expansion ratios for model 5. Bottom figure: the isentropic absolute pressure and temperature for model 5. The initial assumed reservoir pressure and temperature are given in the legend.

It can be seen that at the inlet, the Mach number is already relatively high with a value of 0.558. This is because there is a pressurized chamber underneath the model, and the inlet of the channel has a relatively small diameter. The smaller inlet diameter will force a pressure reduction and flow velocity increment, making the Mach number relatively high at the inlet. Model 6 is the model where the inlet is also the narrowest section of the channel, so that A/A_t is very large before the throat, which can be compared to the converging-diverging models. It can be seen that at the vent, the design (isentropic) Mach number of 1.993 is reached. The isentropic Mach numbers at the vent for the converging-diverging channel models are as follows:

- Plexiglass model: Mach 1.993
- Model 1 - the narrower converging-diverging channel: Mach 2.330
- Model 2 - the wider converging-diverging channel: Mach 2.190
- Model 5 - increased channel length and different material: Mach 1.993
- Model 6 - the diverging channel: Mach 3.4285 - assuming the flow is already choked at the inlet (the flow remains subsonic if it is not)

The isentropic expansion ratios of the plexiglass model are plotted in Figure 5.10 [47]. The red line indicates the pressure ratio, the black line the temperature ratio, the cyan line the density ratio and the purple line the Mach number. Although the expansion ratios before the throat are different w.r.t. model 5, as well as the model length, the isentropic Mach number at the vent remains unchanged.

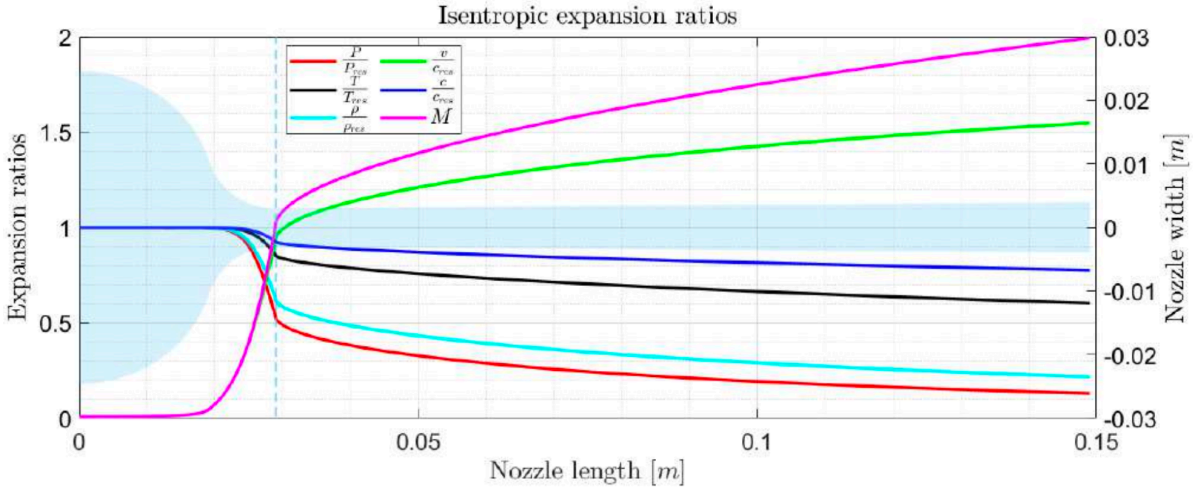

Figure 5.10: Isentropic expansion ratios - plexiglass model [47].

Degree of (super)saturation

In Figure 5.11, the theoretical saturation degree (s = P / $P_{eq}^{(l.g.)}$(T_{gas})) along the channel can be seen for model 5, still assuming the isentropic conditions based on the channel geometry, not measurements. The saturation degree is plotted for different reservoir temperature/pressure combinations, where the (dark) blue line resembles the triple point conditions. Besides the triple point conditions, temperatures of 15°C and 30°C were evaluated, with pressures of 2 and 3 times the triple point pressure (12.234 and 18.351, respectively), similar to the isentropic temperature and pressure plot before. It can be seen that regardless of the reservoir temperature or pressure, the vapor will become extremely supersaturated. This is mainly due to the fact that the liquid-gas equilibrium pressure only depends on the temperature of the gas. With the isentropic assumption, the temperature of this gas can be extremely low, even below -100°C at the vent depending on the reservoir temperature, as seen in the bottom figure of Figure 5.9. For these low temperatures, the vapor quickly becomes saturated. Sklavenitis' experiments have shown that the temperature of the flow comes nowhere near -100°C at the vent, and therefore the theoretical saturation degree is severely overestimated under the isentropic assumptions based on the channel geometry. It can however be seen that for all reservoir temperature/pressure combinations, the flow already becomes supersaturated before the throat. The degree of saturation will be re-evaluated using the experimental data, so with the actual temperature along the channel and the actual reservoir conditions. This could reveal when (or if) condensation should occur, and if a condensation shock is instigated. From the figure it is nonetheless evident that under constant pressure and increasing temperature, the saturation degree curve decreases, and for constant temperature and increasing pressure, the saturation degree curve increases.

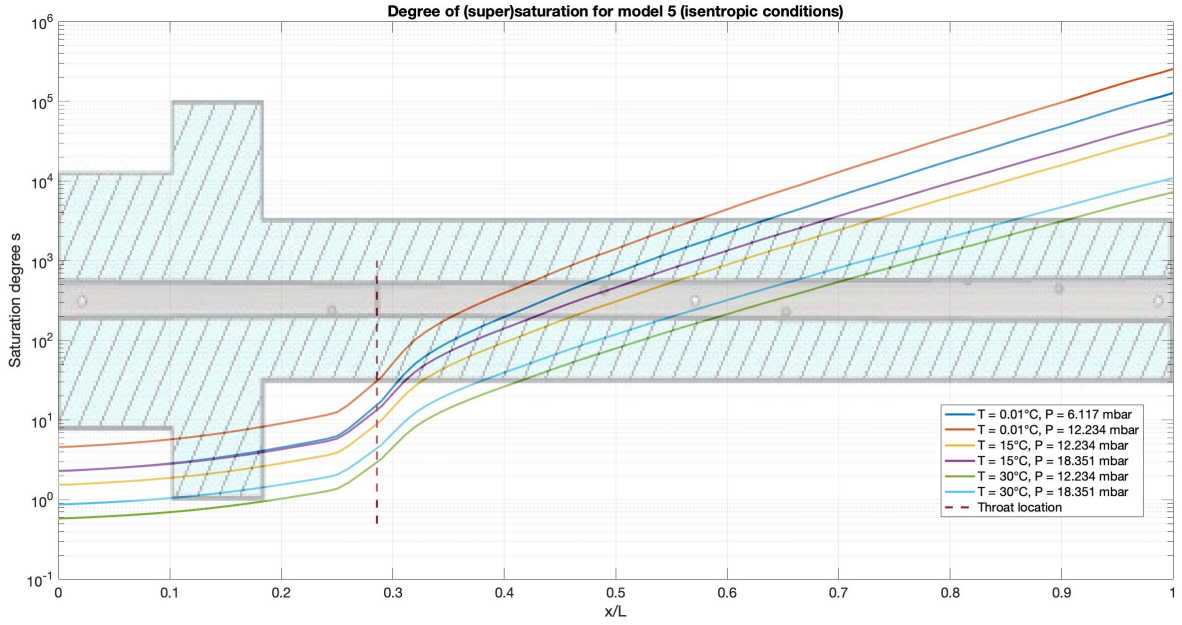

Figure 5.11: Saturation degree s for different pressure/temperature combinations. Model 5 - isentropic conditions. The dashed line indicates the throat of the channel, and the given pressure and temperature in the legend are the conditions of the reservoir.

Condensed mass fraction for thermal choking

The next parameter that is analyzed is the theoretical condensed mass fraction to thermally choke the flow, or f_{max}. Previous experiments have shown an indication of the presence of a thermal throat, due to the condensation occurring in the channel. The required condensed mass fraction of the flow to thermally choke the flow can be estimated by calculating the critical specific heat addition q_{max} using Equation 5.1 [52], and subsequently calculating f_{max} using Equation 5.2 [47]. The value the specific enthalpy of vaporization Δh_{vap} is assumed to be 2514 kJ/kg (based on a pressure of 10 mbar and temperature of 7°C, as a possible combination for the reservoir conditions [3]). The specific heat capacity at constant pressure c_p is assumed to be 1.86 kJ/kgK[4]. The specific heat ratio γ is set at 1.33. The stagnation temperature T_0 is assumed to be 20°C, and for realistic temperature changes, the maximum change in f_{max} is approximately 0.3%. The uncertainty of $\delta f_{max} = \pm\frac{1}{2}\left(\frac{q_{max}}{\Delta h_{vap}}\right)$ [47].

$$q_{max} = c_p \cdot T_0 \cdot \frac{(M^2-1)^2}{2(\gamma+1)M^2[1+\frac{1}{2}(\gamma-1)M^2]} \tag{5.1}$$

$$f_{max} = \frac{q_{max}}{\Delta h_{vap}} \cdot \left(1 - \frac{q_{max}}{2 \cdot \Delta h_{vap}}\right) \tag{5.2}$$

The result is plotted in Figure 5.12. For M = 0.5, 9.55% of the flow has to condense to choke the flow, and for M = 0.7, 2.26% has to condense. Following from the predicted isentropic Mach number from the previous section, it can be seen that relatively little additional heat is required to thermally choke flows with these velocities. It can also be seen that when the Mach number approaches 1, the required condensed mass fraction to choke the flow quickly reduces, and quickly increases again when the flow is supersonic. This indicates that when the Mach number is becomes close to 1, only little additional heat is required to thermally choke the flow, but also to keep the flow velocity at Mach 1 if it were to become supersonic. When the flow is supersonic, the condensation can still cause thermal choking, which in this case will cause a condensation shock and make the flow subsonic again in the channel.

[3] https://www.engineeringtoolbox.com/steam-vapor-enthalpy-d_160.html
[4] https://www.engineeringtoolbox.com/water-vapor-d_979.html

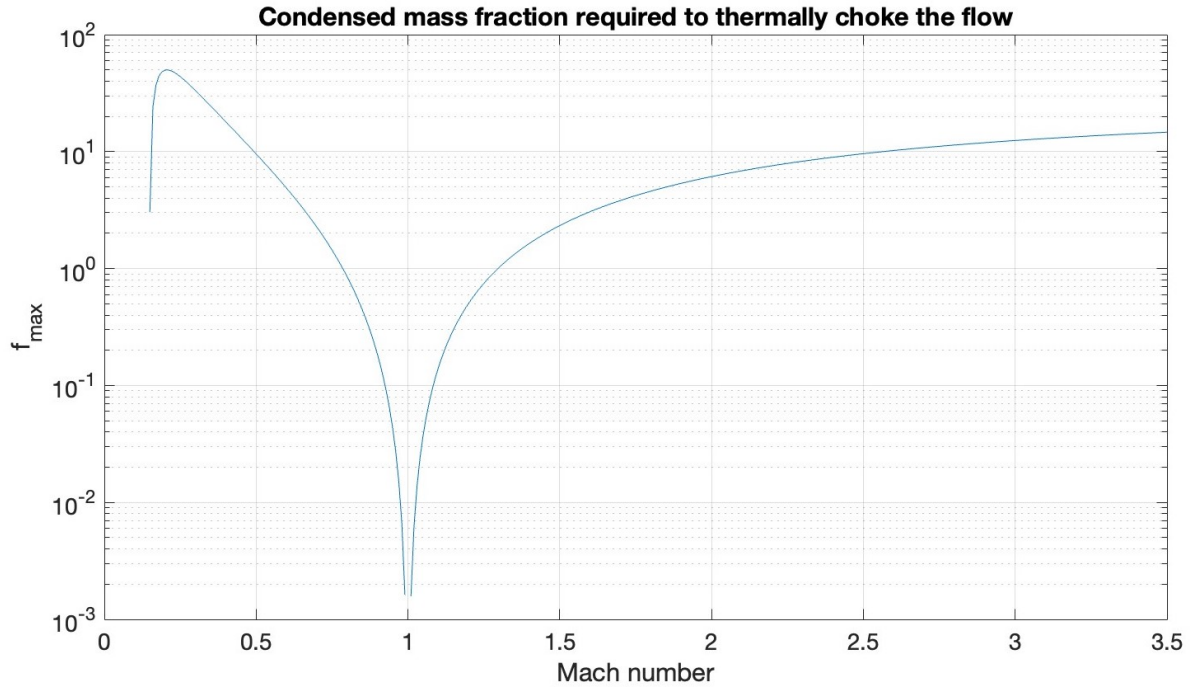

Figure 5.12: Condensed mass fraction required, to thermally choke the flow (plotted as the percentage of the total flow mass).

5.4.2. Straight channel

For the straight channel, the Fanno- and Rayleigh flow relations (from Chapter 3) will be used to assess whether friction or heat transfer alone could either frictionally or thermally choke the flow. These relations are only valid for constant area channels. The flows only have an input and output, so this section only focuses on the inlet and vent conditions and does not contain a plot of the flow behavior throughout the channel.

Fanno flow

Starting with friction, the (Fanno) choked flow duct length equation from Chapter 3 is repeated below for convenience (Equation 5.3).

$$\frac{4fL^*}{D} = \frac{1-M^2}{\gamma M^2} + \frac{(\gamma+1)}{2\gamma} \ln\left(\frac{(\gamma+1)M^2}{2+(\gamma-1)M^2}\right) \tag{5.3}$$

When conducting the experiments with various power settings, the Mach number at the inlet (M) and the point along the channel where the flow becomes choked (L^*, in case choking occurs) can be estimated, and since channel diameter D and specific heat ratio γ are fixed, the shear stress coefficient f can then be approximated by using the equation above. If the flow becomes choked exactly at the vent (so at L^* = 245 mm), f will be 0.0046 if the inlet Mach number is assumed the same as model 5 (=0.558). If the inlet Mach number is reduced to M=0.2, f = $\pm$0.0967 and if M is increased to M=0.7, f = $\pm$0.0014, but it is not likely that the deviation of the inlet Mach number is so large because the change in channel diameter is only small. This means that there is a significant variation in the shear stress coefficient if the inlet conditions vary. When f is estimated, the property relations of the Fanno flow from Chapter 3 will be used to estimate the temperature and pressure gradients along the flow, and will be compared to the isentropic solutions. The effects of friction can be significant in this study, as it accelerates subsonic flow and decelerates supersonic flow. It essentially squeezes the channel due to the generated boundary layers on the channels walls. If the length of the channel is shorter than the choked flow duct length, the flow does not become sonic. If the choked flow duct length is equal to the channel length, the flow becomes sonic exactly at the vent. And if the length of the channel is larger than the choked flow duct length, the flow is 'adjusted': the sonic point will be shifted towards the vent, regardless of the (additional) channel length. It is theoretically not possible for a flow to become supersonic by friction alone. The estimated shear stress coefficient from the straight model can be taken into account during the analysis of the converging-diverging channels, as all the models (except

model 5 and the plexiglass model) are made out of the same material and are expected to have about the same friction effects.

Rayleigh flow
For the heat addition, the Rayleigh flow relations from Chapter 3 are used, and the relations used for the calculations below are repeated for convenience. For the theoretical performance, various values for the inlet conditions are entered into the calculation model, and the corresponding exit conditions are the output of the calculations. For the inlet, values for the Mach number (M_1 = 0.25, 0.5), pressure (P_1 = 6.117, 12.234 mbar) and temperature (T_1 = 0.01, 20 °C) are assumed (similar to the assumed values in the previous sections). A baseline is calculated using the first number of the values between the brackets, and recalculated with one of the four variables changed to the value on the right side between the brackets. This is done to determine the effects on the flow parameters if only one of the inlet conditions has changed. The values for q are an estimation based on preliminary calculations using results from the previous experiments with the plexiglass model, and q is positive in case of heat addition.

First, the (initial) stagnation temperature $T_{0,1}$ and stagnation pressure $P_{0,1}$ are calculated using Equation 5.4 and Equation 5.5. The values used for γ and c_p in the following calculations are equal to the values mentioned in the previous sections, and are 1.33 and 1.86, respectively. The units used in the calculations are kPa for pressure, and K for temperature.

$$T_{0,1} = T_1 \left(1 + \frac{\gamma - 1}{2} M_1^2\right) \tag{5.4}$$

$$P_{0,1} = P_1 \left(\frac{T_{0,1}}{T_1}\right)^{\frac{\gamma}{\gamma-1}} \tag{5.5}$$

Next, the stagnation temperature at the sonic point is calculated, by solving for T_0^* in Equation 5.6:

$$\frac{T_{0,1}}{T_0^*} = \frac{2(\gamma+1)M_1^2\left(1 + \frac{\gamma-1}{2}M_1^2\right)}{(1+\gamma M_1^2)^2} \tag{5.6}$$

The change in stagnation temperature can be calculated using $T_{0,2} = T_{0,1} + q/c_p$, where q is the arbitrarily chosen heat addition term (using q = 25 and 50 kJ/kg). The Mach number at the vent (M_2) can then be calculated using Equation 5.6, by filling in the value for $T_{0,2}$ and solving for M, making use of the fact that T_0^* does not change with a change in state. $P_{0,2}$ and P_0^* can be calculated using Equation 5.7 and filling in the values for M_1, M_2 and $P_{0,1}$, and again making use of the fact that P_0^* doesn't change with a change in state. 'x' in this equation is either 1 or 2, depending on the state (before or after the heat addition).

$$\frac{P_{0,x}}{P_0^*} = \frac{\gamma+1}{1+\gamma M_x^2}\left[\left(\frac{2}{\gamma+1}\right)\left(1 + \frac{\gamma-1}{2}M_x^2\right)\right]^{\frac{\gamma}{\gamma-1}} \tag{5.7}$$

We then calculate T_2 and P_2 using Equation 5.8 and Equation 5.9, finishing the calculations.

$$T_2 = \frac{T_{0,2}}{\left(1 + \frac{\gamma-1}{2}M_2^2\right)} \tag{5.8}$$

$$P_2 = \frac{P_{0,2}}{\left(1 + \frac{\gamma-1}{2}M_2^2\right)^{\frac{\gamma}{\gamma-1}}} \tag{5.9}$$

The results for the different assumed inlet conditions are summarized in Table 5.2. The calculation method has been validated by solving Example 4.1 of *Fundamentals of Gas Dynamics* for the values used in the example, and correcting the equation used to solve for P_2 [53].

Table 5.2: Vent conditions for assumed inlet conditions, calculated using the Rayleigh flow equations.

Input:					
Assumed inlet Mach number M1 [-]	0.25	0.5	0.25	0.25	0.25
Assumed inlet pressure P1 [mbar]	6.117	6.117	12.234	6.117	6.117
Assumed inlet temperature T1 [°C]	0.010	0.010	0.010	20	0.010
Assumed specific heat addition q [kJ/kg]	25	25	25	25	50
Output:					
Calculated vent Mach number M2 [-]	0.2571	0.5225	0.2571	0.2566	0.2641
Change in Mach number w.r.t inlet [-]	+0.0071	+0.0225	+0.0071	+0.0066	+0.0141
Calculated vent pressure P2 [mbar]	6.090	5.980	12.180	6.092	6.063
Change in pressure w.r.t. inlet [mbar]	-0.027	-0.137	-0.054	-0.025	-0.054
Calculated vent temperature T2 [°C]	13.146	11.882	13.146	33.137	26.264
Change in temperature w.r.t. inlet [°C]	+13.136	+11.872	+13.136	+13.137	+26.254

It can be seen from the results that for a large increase in temperature along the channel, the increase in Mach number and decrease in vent pressure is only low. This means that for realistic values for the inlet Mach number, pressure and temperature, unrealistic values for the specific heat addition q are required to thermally choke the flow. The value for q will be estimated more accurately using the experimental data from the experiments. In reality, the model will experience both friction and heat addition, so in Chapter 6 it will be determined to what extent the friction and heat addition contribute to the change in entropy of the flow.

6

Experiments and results

This chapter details the experiments conducted, and the accompanying results. The chapter starts with a description of the experiment preparations, and the verification and validation of the setup and used methods (Section 6.1). Then, the results of the plexiglass model are described, and compared to the results of the previously conducted experiments with the plexiglass model (Section 6.2). Subsequently, the effects of the channel length (Section 6.3) and channel diameter (Section 6.4) are studied. Then, the channel shape is explored, including a straight channel (Section 6.5) and a diverging channel (Section 6.6. Lastly, the design choices and boundary conditions are evaluated (Section 6.7), followed by a result comparison with a Computational Fluid Dynamics model (Section 6.8).

6.1. Experiment preparations and verification & validation

This section is divided into two parts: experiment preparations and the outline of the experiments.

6.1.1. Experiment preparations

Each experiment follows a list of preparation steps, where the configuration and power settings are selected such that eventually each model is covered for every power setting.

Configuration and setup preparation

In order to get the complete measurements of a model, three different configurations are required for the longer channel models, and 2 different configurations are required for the plexiglass model. A 'configuration' in this case is a fixed pressure and temperature sensor allocation over the channel. Combining the readings of these configurations gives the results for the whole model for a certain power setting. Since each different configuration includes one measuring point that coincides with another configuration, the data of different configurations could be manipulated such that they match the other configuration and can be combined. If experiments were conducted under different initial or boundary conditions (for example different temperatures on a different day), this data manipulation consists of time shifts and scaling factors for the pressure and temperature, which are required in order to align the measurements. A schematic overview of the different configurations for the longer channel models can be seen in Figure 6.1. For the plexiglass model, there are 4 measurement points for the temperature, so a configuration swap is not necessary. The 8 pressure measurement points of the plexiglass model are distributed over 2 different configurations, with the reservoir pressure coinciding for the different configurations.

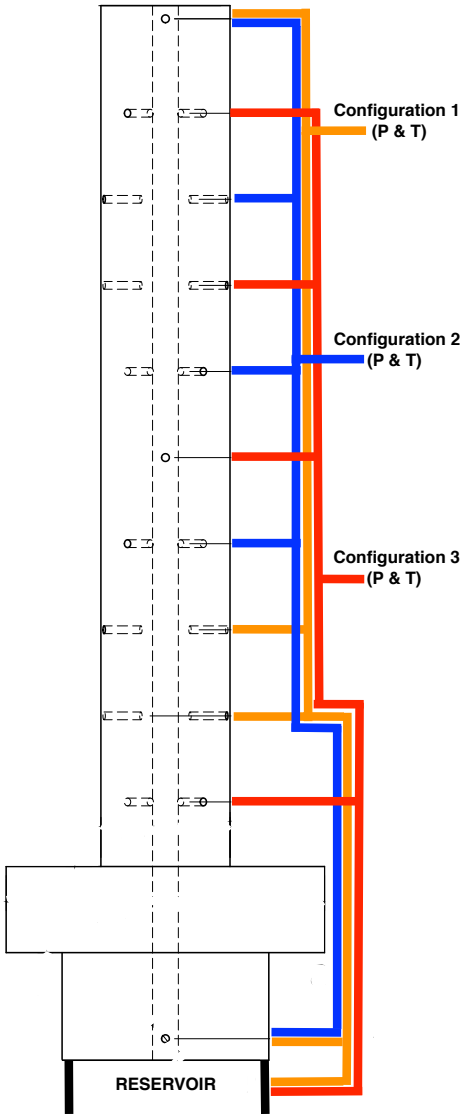

Figure 6.1: The measuring points along the channel, for the three different configurations.

The experimental procedure is as follows:

- Before the first experiment of the day, the vacuum chamber pumps are turned on for at least 30 minutes, to warm up.
- The five temperature sensors are glued into place using a glue gun.
- The unused holes for the temperature sensors are shut with duct tape.
- The unused tubes for the pressure sensors are shut using a tube that is closed on the other end.
- The model is placed on top of the reservoir lid, and the splash screen is installed on the bottom of the lid, see Figure 6.2. The splash screen prevents the buildup of an 'ice tunnel', seen in Figure 4.4.
- The model is placed inside the test section, and the water level of the reservoir is filled up to $\pm$ 2000 ml (or $\pm$ 2500 ml for model 3, the longer straight channel).
- The thermocouples are connected to the connectors inside the vacuum chamber. The pressure sensor tubes are connected to the metal tubes on the model. The small and large heating foils are connected to their power supplies.
- The sensors are tested in Labview, to see if they are connected and functioning properly (no blockages by water etc.).

- The experiment is then started: the data and time are logged, the vacuum chamber pumps are turned on and the settings of the power supply are selected.
- After 30 minutes, the data logging is stopped and saved, the vacuum chamber is re-pressurized and the power supply is turned off after the reservoir water is reheated to 20°C. Except for the warmup, this process is repeated for each experiment. The connected models, ready to use, can be seen in Figure 6.3.

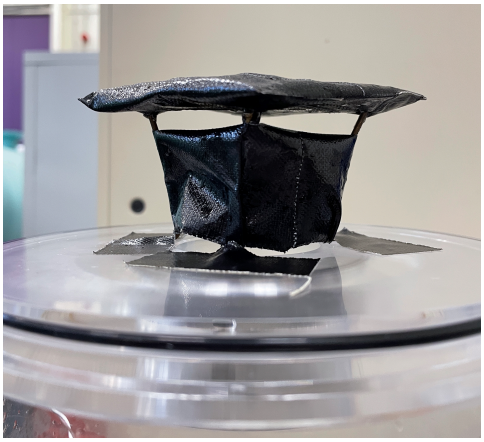

Figure 6.2: The splash screen installed on the bottom of the lid of the reservoir. The splash screen prevents liquid from entering the channel.

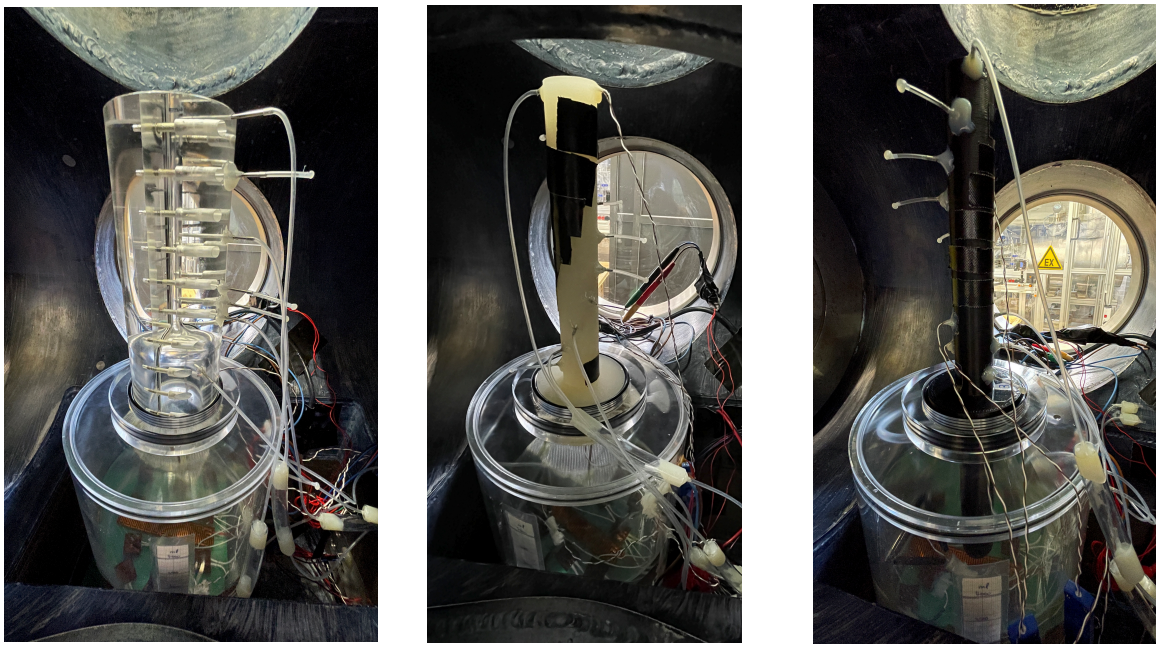

Figure 6.3: On the left: the plexiglass model, in the middle: an example of one of the 5 3D printed PLA models, and on the right: the 3D printed PP model, with all wires and tubes attached.

Power settings

As mentioned in Section 4.2, the water in the reservoir is heated by heating foils, which are connected to the power supply. During the preparations for a specific experiment, the power settings are selected accordingly. For this study, each experiment is conducted with three different power settings, which are: *full power*, *half power* and *no power*. The inclusion of different power settings is due to the fact that the temperature and pressure of the reservoir are directly controlled by these power settings, which have a direct and large influence on the flow behaviour. By selecting the *no power* setting, the liquid

surface water will eventually freeze, and the surface water freezes faster when channels have a larger diameter. The *full power* setting is included to maintain higher water temperatures and thus more violent boiling and a higher pressure inside the reservoir, which results in a higher pressure difference with the vacuum chamber. The maximum power of the large foil is limited by the maximum voltage of the power supply, and the maximum power of the small foils is limited by the maximum electric current of the power supply. Combined, they can deliver 139.7 W of heating power. The *half power* setting delivers half the power of the *full power* setting: 70.07 W. The *half power* setting is included to establish the effects of the transition from lower to higher temperatures and pressures. These settings can be used to observe the behaviour of the flow through the channels of the models for different 'initial conditions'. An overview of the power settings as input for the power supply is given in Table 6.1.

Table 6.1: Overview of the different power settings.

Full power	Voltage	Electric current	Power
Large foil	32.1 V	1.61 A	51.68 W
Small foils	27 V	3.26 A	88.02 W
Combined heating power			139.7 W
Half power			
Large foil	22.6 V	1.14 A	25.76 W
Small foils	19.1 V	2.32 A	44.31 W
Combined heating power			70.07 W
No power			
Large foil	0 V	0 A	0 W
Small foils	0 V	0 A	0 W
Combined heating power			0 W

6.1.2. Experimental setup verification & validation

The analysis of a typical chamber evacuation, the corresponding progression on the phase diagram and the estimation of the measurement uncertainty are used to verify & validate the experiments.

Typical chamber evacuation

To see the typical behavior of the flow during an experiment, the conditions in the setup (with model 1) are plotted, measured at different locations: at the reservoir (Figure 6.4), halfway the channel (Figure 6.5 and at the vent (Figure 6.6).

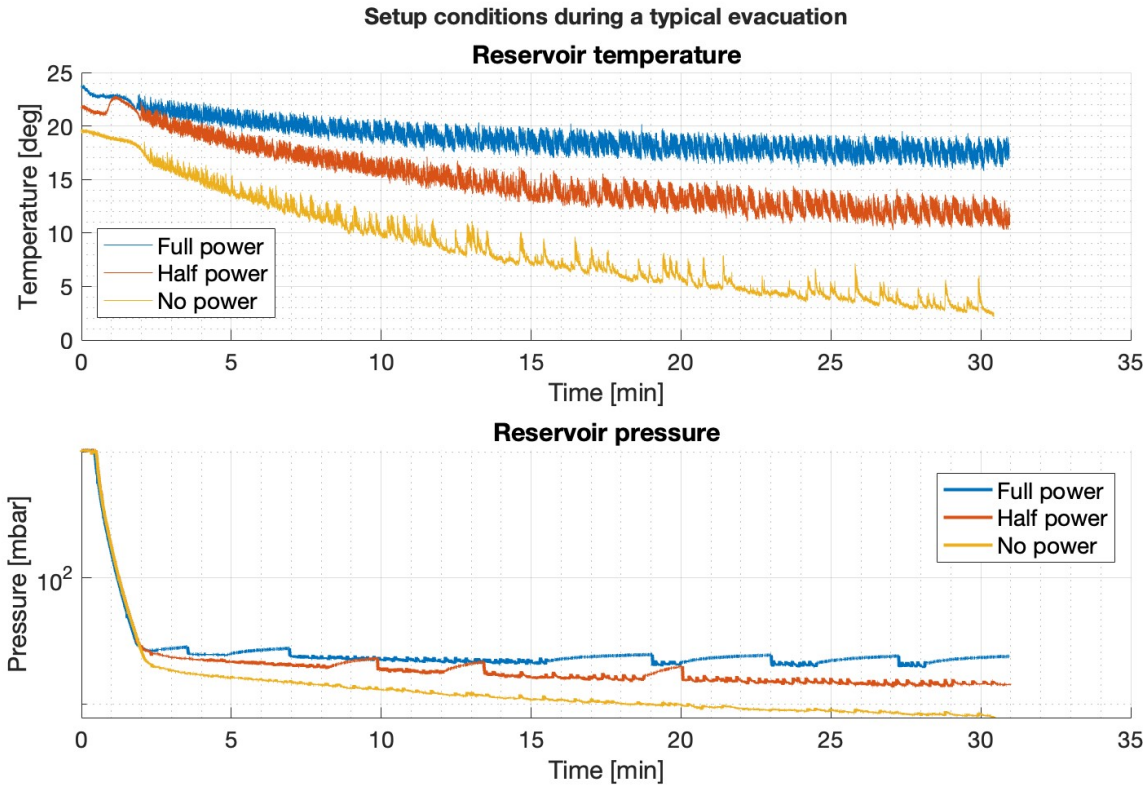

Figure 6.4: Reservoir conditions during a typical evacuation.

In Figure 6.4, it can be seen that when more heating power is supplied, the temperature converges to equilibrium conditions, and without heating it will take longer to reach an equilibrium than the 30 minutes of the experiment. Because the water supply is finite, the conditions will never be long-term stable, unless the liquid surface water freezes before the water is completely evaporated when no heating power is supplied. The small peaks in the plot are attributed to the boiling of the water when the chamber pressure becomes low enough to initiate the boiling stage. It can also be seen that when no heating power is supplied, there are less temperature fluctuations, meaning that the intensity of the boiling is much lower. When more heating power is supplied, the temperature drops less fast. The higher power settings also increase the reservoir pressure. The small ramps that can be seen for the full and half power setting are due to the fact that the boiling water droplets covered the inlet of the pressure sensor tubes, making the readings temporarily invalid. When the reservoir pressure reduces over time, the tubes become unblocked again when the water that is blocking the tube is drawn back to the reservoir due to the pressure difference.

In Figure 6.5, it can be seen that the conditions halfway the channel are more stable. Also in this case, the higher power settings correspond to a higher pressure and temperature in the channel. The lines are almost linear, but even with the full power setting it can be seen that no equilibrium is reached after 30 minutes.

The vent conditions are the most unstable, and show inconsistencies throughout the experiments. The temperature curves show that because of the difference in initial temperatures, it takes at least 15 minutes to reach a state where the differences in initial conditions are mitigated. Because of this, throughout the experiments in this study the conditions at t = 25 min are analyzed and compared. It can also be seen that at t = 30 min, the temperature of the no power setting became higher than the half power setting, making the time an important factor in the analysis. For the pressure, it can be seen that the readings are fluctuating much more than the other locations. This is because the pressure difference with the vacuum chamber is the smallest at that section, making the pressure sensors measure pressures close to their offset values, causing more fluctuations. The fluctuations

can be mitigated using the data manipulation methods mentioned in Chapter 4.

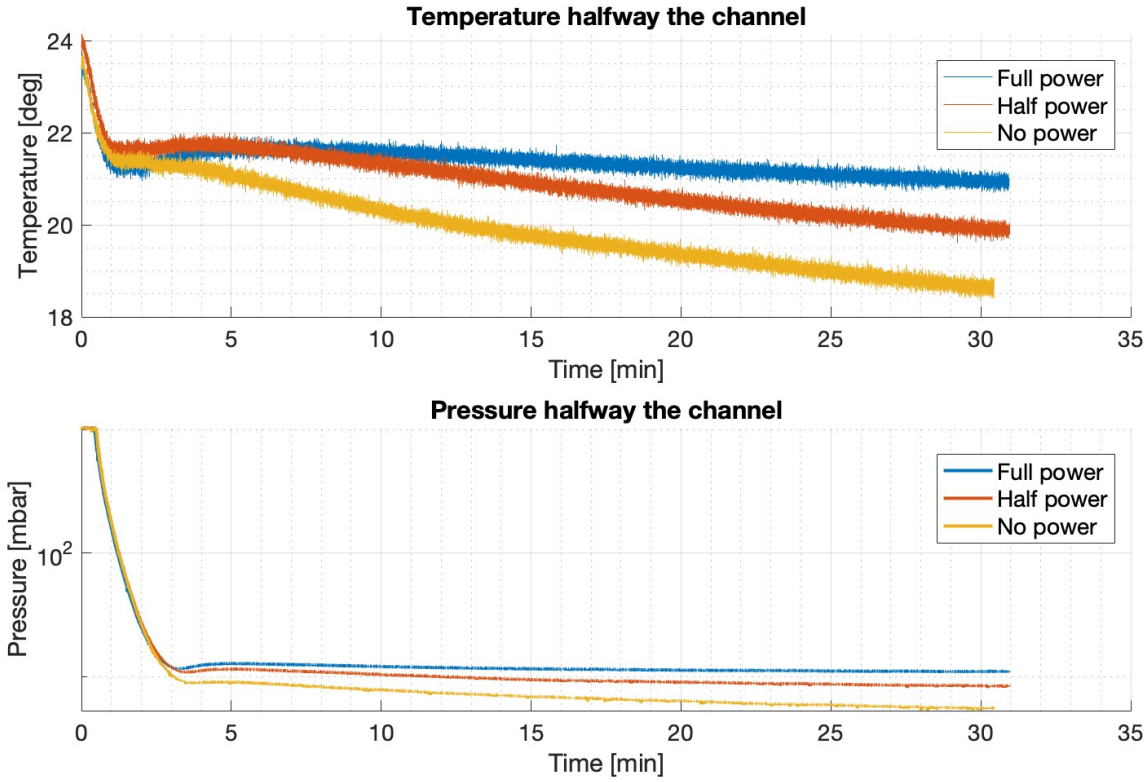

Figure 6.5: Conditions halfway the channel during a typical evacuation.

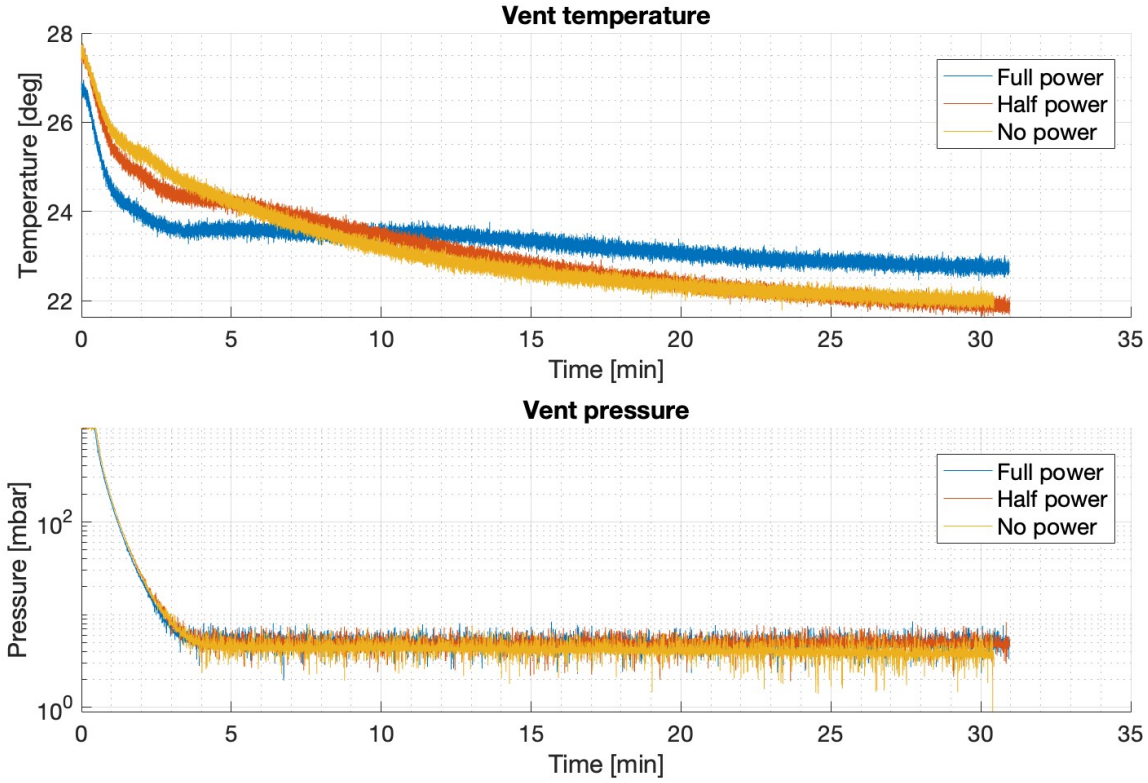

Figure 6.6: Vent conditions of a typical evacuation.

Typical progression on phase diagram

The typical progression of the reservoir conditions on the phase diagram can be seen in Figure 6.7. These are the results with model 1 (the narrower converging-diverging channel) on top of the large reservoir. It can be seen that when less heating power is supplied, the conditions descend along the liquid-gas equilibrium line towards the triple point. The horizontal shifts that can be seen for the full and half power setting, are due to the blocked pressure sensor tubes mentioned in the previous section. The small temperature peaks due to the boiling can also be seen in the plot as the small protrusions to the right of the liquid-gas equilibrium, which is evaporating water. Because the temperature is measured on the surface of the water, and the pressure is measured in the remaining reservoir volume above the water, the pressure is above the liquid-gas equilibrium line since the reservoir water is in the liquid phase. The descend along this equilibrium line validates the conditions of the experiment. When a model is used with a higher mass flow rate (or wider throat/channel), more heat is lost and the conditions stagnate around the triple point. The water in this case changes to the ice phase as it becomes slightly colder than the triple point conditions and passes the solid-liquid equilibrium line, at around -2°C.

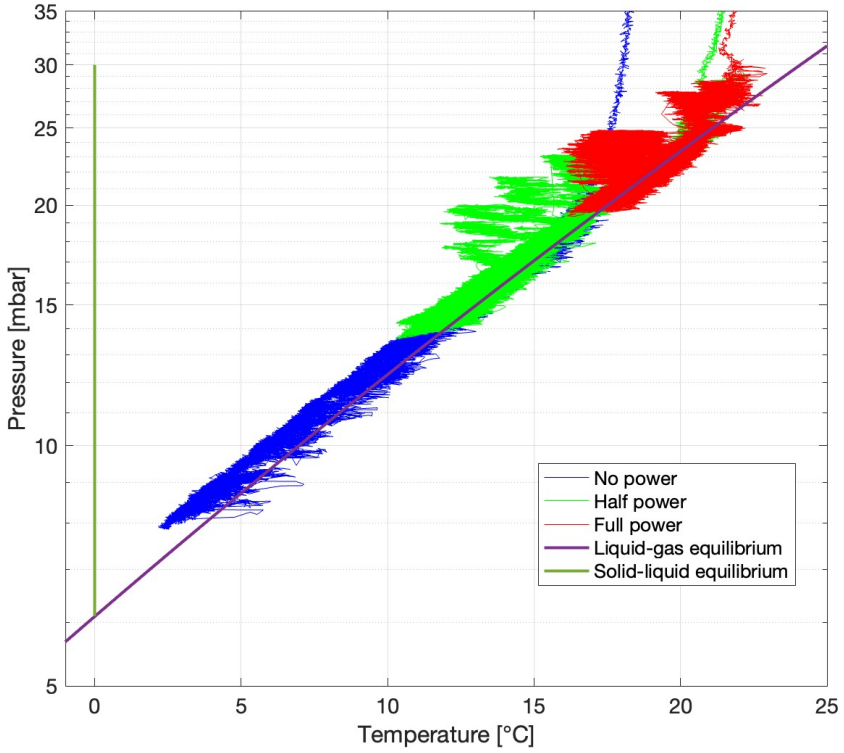

Figure 6.7: Progression on the phase diagram for each power setting.

Estimation of measurement uncertainty
The uncertainty of the measuring equipment itself was estimated in Chapter 4, but because of statistical noise and the fact that either two or three configurations have to be combined into one set of flow conditions, the measurement uncertainty was re-evaluated. The uncertainty from these sources is much higher than the uncertainties predicted in Chapter 4. The uncertainties are listed below and are based on the experimental data, being the largest temperature and pressure shift between the different configurations:

- The uncertainty in the pressure measurements is $\pm 1.5\%$.
- The uncertainty in the temperature measurements is $\pm 3\%$.
- Therefore, the uncertainty in the pressure ratio is $\pm 3\%$ and the uncertainty in the temperature ratio is $\pm 6\%$.
- Since the Mach number calculations are based on the pressure ratio, the uncertainty of the Mach number is also $\pm 3\%$. But because the Mach number calculations assume isentropic conditions, the assumption in general will have a greater uncertainty than the aforementioned percentage. The exact uncertainty is not known and will be discusses throughout the results.

6.2. Plexiglass model results and comparison

This section presents the results of the plexiglass model, for experiments conducted with the model at room temperature (Section 6.2.1) and with the model stored in a freezer overnight (Section 6.2.2). The results are subsequently compared with the results of Sklavenitis' study (Section 6.2.3). The term 'Sklavenitis' study' used throughout this chapter refers to the work presented in the Master's thesis of S. Sklavenitis, on the previous analysis of the plexiglass model [47]. The term 'this study' refers to the experiments and results from this thesis.

6.2.1. Results of the plexiglass model

To analyze the flow of the plexiglass model for the different power settings (at room temperature and t = 25 min), the pressure, temperature, pressure ratio, isentropic Mach number and saturation degree are plotted in Figure 6.9, where the channel geometry is superimposed on the plot. The isentropic Mach

number is based on the pressure ratio rather than the temperature ratio. This has been done for all experiments, as it turned out that the pressure ratio is a more reliable parameter to base the follow-up calculations on. This has two reasons, the first being that the pressure is less dependent on the initial conditions of the setup, such as the room temperature or the initial reservoir water temperature (which will be described in more detail in Section 6.7). The second is that the temperature increases throughout the channel and there are thermal effects in the channel (just as was observed during Sklavenitis' experiments), causing a large deviation from the isentropic solution for the temperature of the flow. A comparison between the calculation of the isentropic Mach number based on the pressure- and temperature ratio for a specific case (Model 1 - full power) can be seen in Figure 6.8. 'FP' refers to the full power setting, 'HP' to the half power setting and 'NP' to the no power setting.

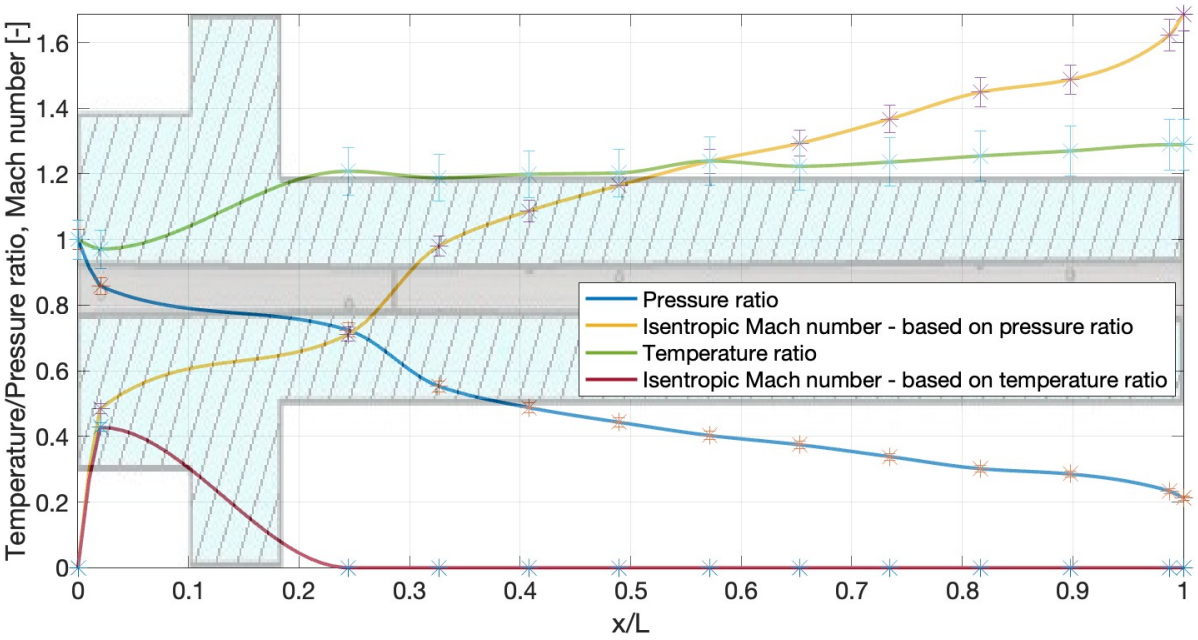

Figure 6.8: Isentropic Mach number based on the pressure ratio and the temperature ratio (for model 1 - Full power setting).

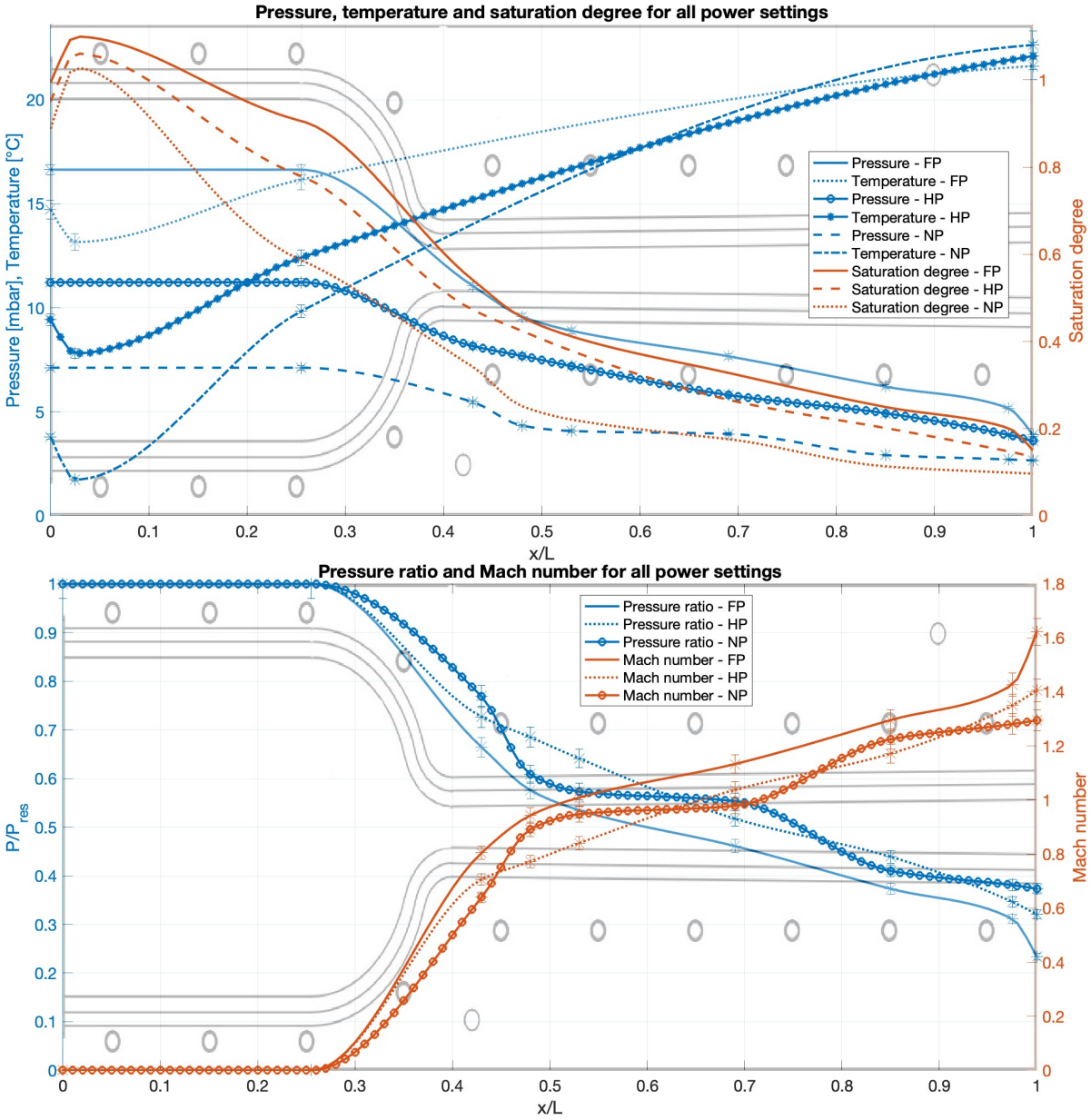

Figure 6.9: Plexiglass model. Full, half and no power settings at t = $\pm$ 25 min.

It can be seen that the flow is choked for all 3 power settings, although none of them is choked at the geometrical throat. The point where the (isentropic) Mach number becomes 1 is at x/L = 0.52 for the full power setting, x/L = 0.65 for the half power setting and x/L = 0.72 for the no power setting, while the geometrical throat is located at x/L = 0.4. This means that with a higher upstream pressure, the pressure ratio has a steeper decline more upstream in the channel (near the throat) so that the critical pressure ratio is reached earlier in the channel. Theoretically, the sonic point under isentropic conditions should be exactly at the geometrical throat. From Chapter 3 we know that both heat addition and friction move the sonic point more downstream of the throat. The influence of friction is mainly driven by the friction coefficient and the inlet Mach number (for constant area channels). Since the friction coefficient is constant and the inlet Mach number differs only by a Mach number less than 0.1 for the different power settings and the shift in sonic point is relatively small, it is expected that the thermal effects overrule the friction effects. The small pressure dip near the vent at the full power setting is an indication of an underexpanded nozzle, as the exit pressure is higher than the ambient pressure. The temperature of the reservoir water is 14.7°C, 9.4°C and 3.80°C for the full, half and no power setting, respectively. The temperature follows the saturated (reservoir) pressure curve on the P,T-diagram. The small dip

in temperature that can be seen at x/L = 0.025 for each power setting (measured above the reservoir water), is due to the fact that evaporation is an endothermic process. The water molecules on the surface absorb the surrounding heat, increasing the kinetic energy which is required to change to the gaseous phase. Despite the different reservoir water temperatures, the temperatures for all power settings seem to converge to approximately the same temperature at the vent. It is expected that the temperature of the environment and the model itself have a large effect on the temperature inside the channel. Since it was already known from Sklavenitis' experiments that there is a temperature increase through the channel instead of a decrease (as would be expected for an isentropic flow), an additional analysis on the relation between the room temperature and the vent temperature is conducted, and will be described in Section 6.7.3.

6.2.2. Results of the cooled plexiglass model

The experiments were repeated for the full and half power setting, where the plexiglass model is left in a freezer overnight to cool the model. The no power setting has been left out due to time constraints, and with 2 out of 3 power settings conclusions can already be drawn. Because of the high environmental temperatures during the summer when the experiments were conducted, the model warmed up quickly but remained below 14°C after the experiments. As soon as the model left the cooling bag, water immediately started condensing on the model, see Figure 6.10. The results and comparison of the full power setting can be can be seen in Figure 6.11, and Figure 6.12 for the half power setting.

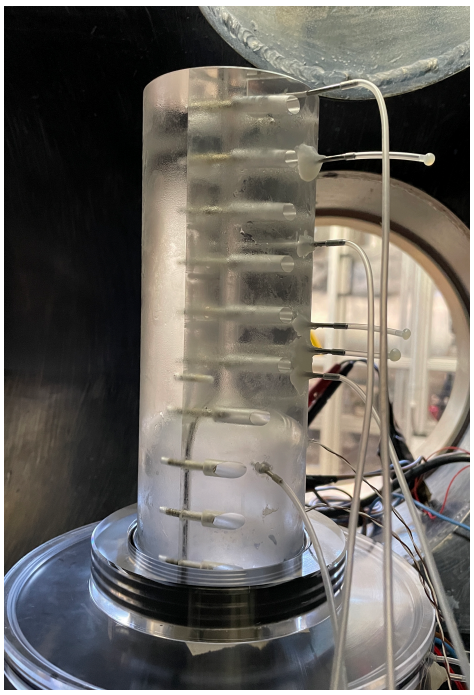

Figure 6.10: Condensation on the cooled plexiglass model inside the vacuum chamber.

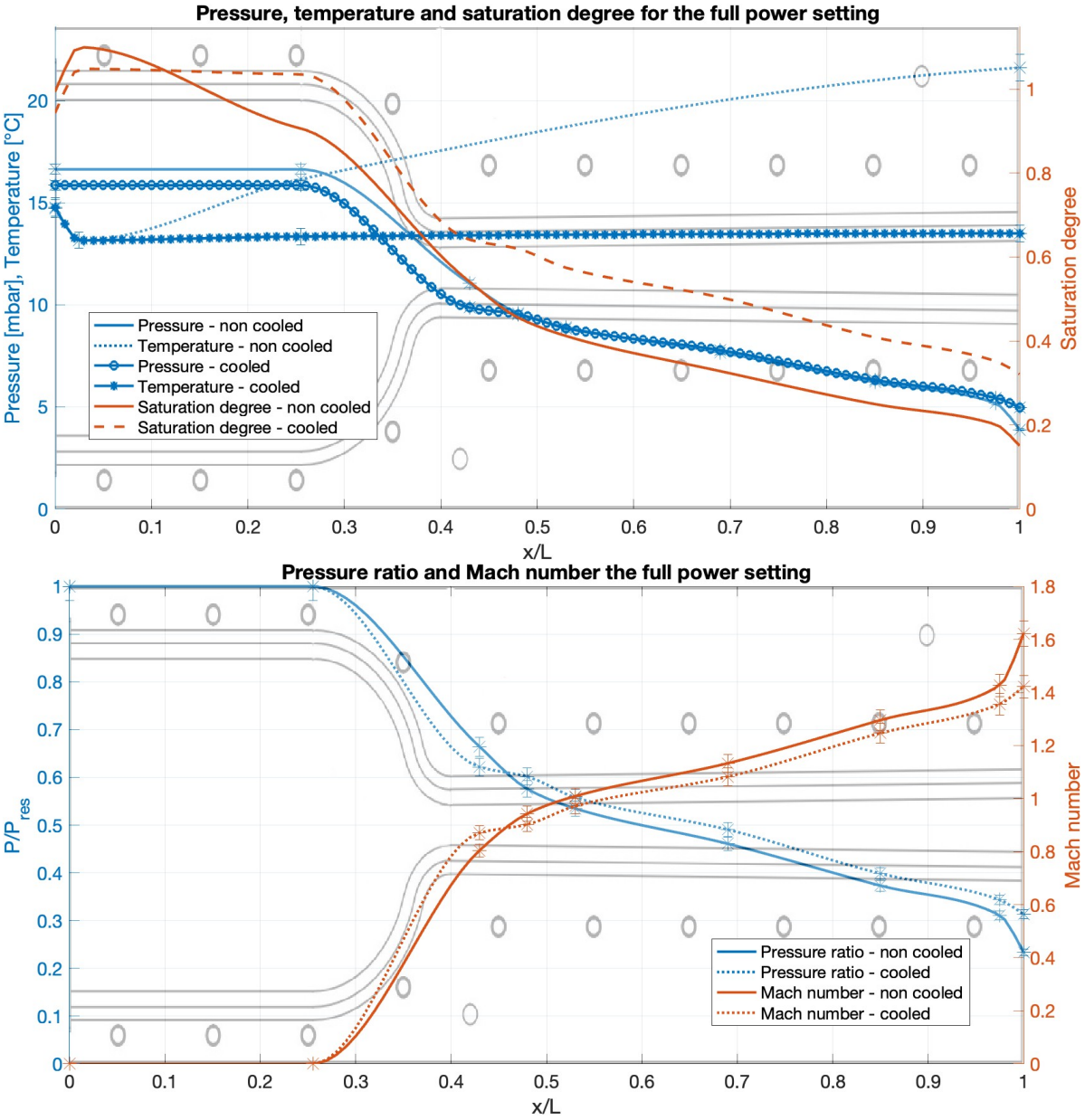

Figure 6.11: Cooled plexiglass model. Full power setting at t = $\pm$ 25 min.

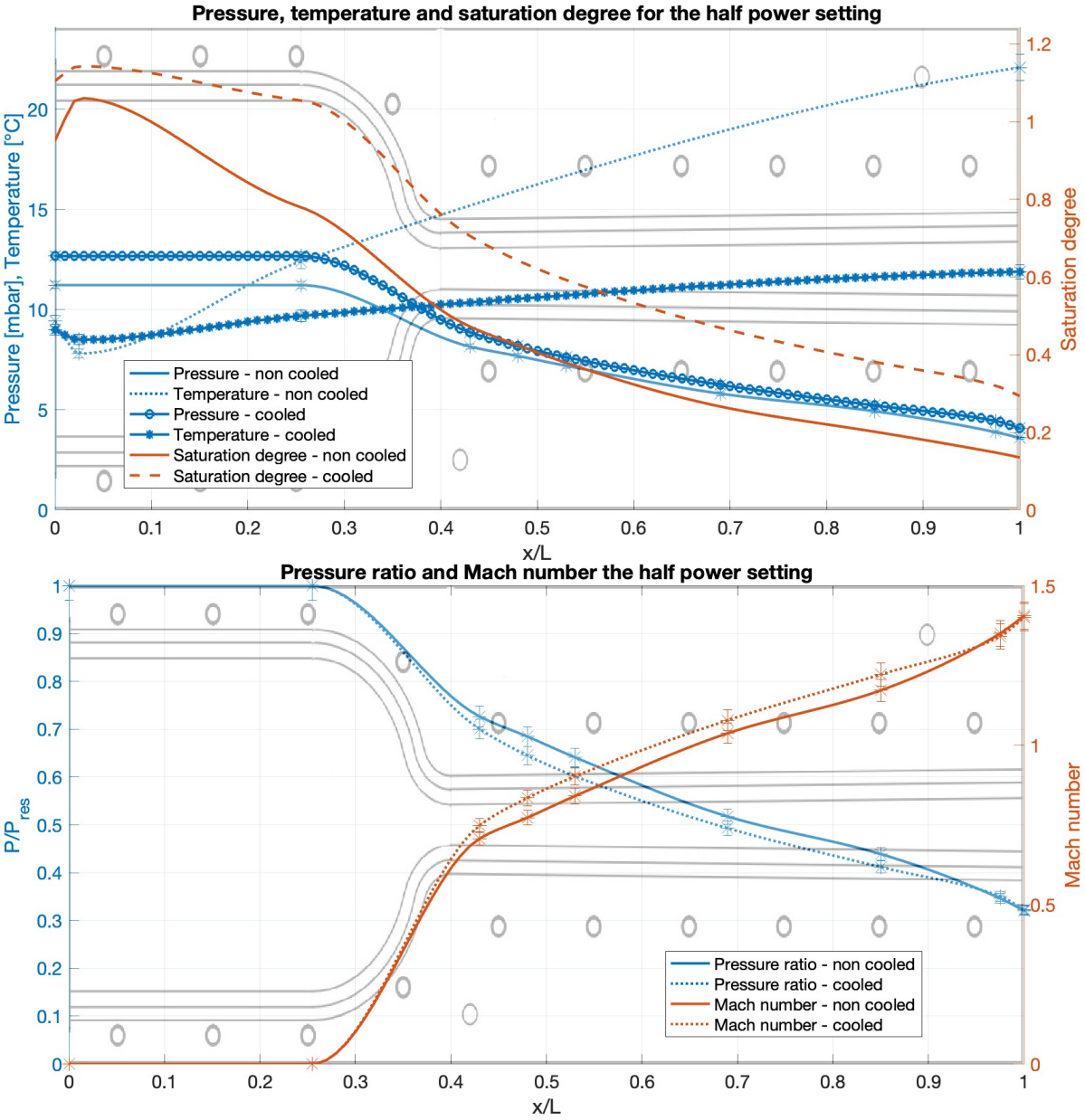

Figure 6.12: Cooled plexiglass model. Half power setting at t = ± 25 min.

It turned out that the flow through the cold plexiglass model had an almost linear temperature increase with time, again making it plausible that the temperature measurements of the model mostly depend on the environmental conditions rather than the flow itself. After 25 minutes, the temperature at the vent for the full power setting is 13.50 °C and 11.9°C for the half power setting. The temperature of the reservoir water is 14.8°C for the full power setting and 9°C for the half power setting. So for the full power setting, the temperature remains almost constant, while for half power it slightly increases towards the vent. Although no separate temperature measurements of the model itself were made, the measured vent temperature seems to be almost equal to the temperature of the model itself rather than the temperature of the flow, which was also observed during the experiments of Sklavenitis' study. As mentioned above, the analysis of this influence follows in Section 6.7.3. The reservoir temperatures are more or less the same as with the experiments without the model being cooled. This meets the expectations, as the temperature of the model does not affect the reservoir conditions. In terms of pressure, the pressure inside the reservoir for the full power setting is 15.86 mbar, and 12.68 for the half power setting. This is slightly lower than the values for the non-cooled model, but this difference is mainly due to a higher pressure in the vacuum chamber because the experiments were conducted in a

different time period (which will be described in more detail in Section 6.7.2). Here, the flow becomes sonic at x/L = 0.56 for the full power setting, and at x/L = 0.61 for the half power setting. This means that cooling the model shifted the sonic point downstream for the full power setting, while it shifted the sonic point upstream for the half power setting. Theoretically, the cooled model extends the section in the channel where condensation occurs, so the latent heat release should shift the sonic point downstream. But the shift is also caused by the change in vacuum chamber pressure: the pressure at the reservoir for both power settings is slightly lower and the pressure at the vent is slightly higher w.r.t. the experiments done with the non-cooled model. As a result, the pressure ratio curves become a bit flattened, shifting the isentropic Mach number as well.

The saturation degree for the 3 power settings for the non-cooled model and the 2 power settings for the cooled model are plotted in Figure 6.13.

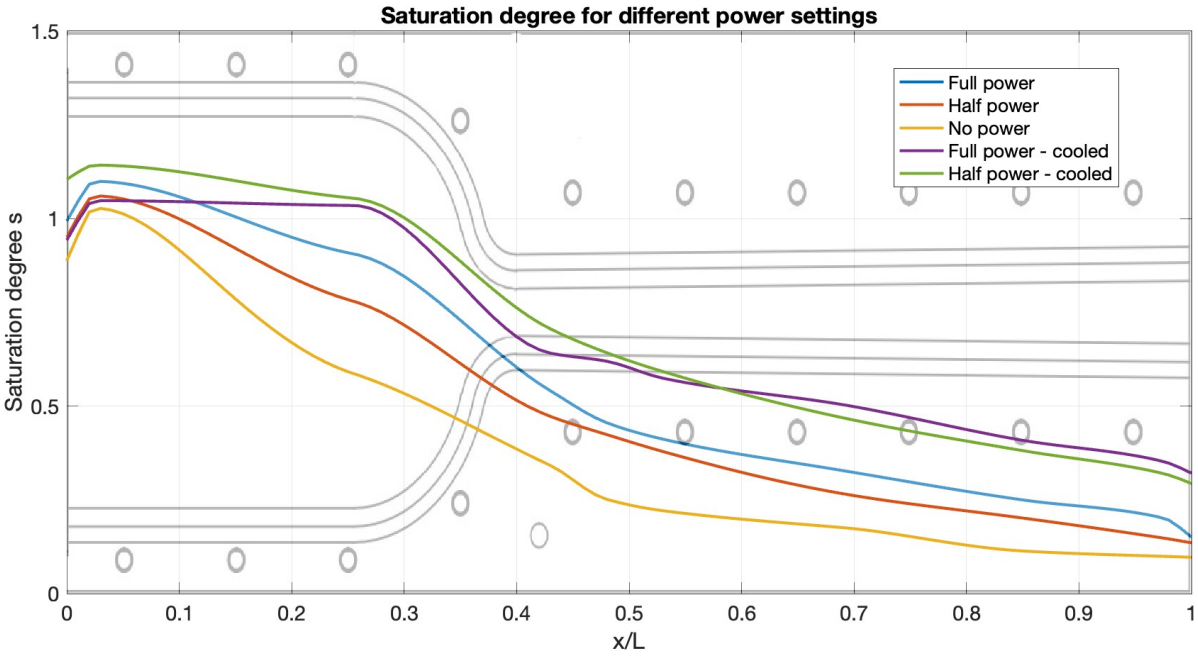

Figure 6.13: Saturation degree comparison for the plexiglass model (at t = $\pm$ 25 min).

It can be seen that for the non-cooled model, the flow only becomes supersaturated in the reservoir. A higher power setting elevates the saturation degree curve, because the pressure increases more than the saturated (equilibrium) pressure for the increasing temperatures through the channel. It shows that cooling the model extends the section where the flow is supersaturated to close to the throat, and also elevates the saturation degree curve throughout the channel. This is because the pressure is about the same as the non-cooled model, but the temperature of the model itself is lower, causing the saturated vapor pressure to drop and the degree of saturation to increase. It can also be seen that the curve for the full and half power setting for the cooled model overlap, which is due to the fact that the half power model was about 1.5°C colder, slightly elevating the saturation degree curve in the channel, so that they become equal. For the same temperature, the curve for the half power setting would have been slightly lower, as was the case for the non-cooled model. For all models it can be seen that the flow is not supersaturated when flowing through the throat, meaning that condensation is only likely to occur in the reservoir, and not in the channel.

The mass flow and isentropic Mach number at the vent for the cooled and non-cooled model for all power settings are given in Table 6.2, and are calculated using Equation 3.10 (M_{vent}) and Equation 3.14 (mass flow rate) or Equation 3.15 (choked mass flow rate). The measured (average) mass flow rate for the non-cooled model is derived from the decrease in water level during the experiments: approx. 130 ml for the full power setting, 70 ml for the half power setting, and 65 ml for the no power setting. The meaning of these numbers will be described in Section 6.7.1, after the numbers of all models are given

in their respective sections. The design Mach number is in this case is 1.993. All power settings and model temperatures reached lower Mach numbers at the vent than the design Mach number, due to the change in entropy from heat addition and friction in the channel. A colored, graphical representation of the temperature and pressure of the flow through the channel can be found in appendix E.

Table 6.2: The isentropic Mach number at the vent and mass flow rate of the plexiglass model.

	Isentropic M_{vent} [-]	Mass flow rate $\dot{m}$ [kg/s]	Measured $\dot{m}$ [kg/s]
Full power	1.427	$8.682 \cdot 10^{-5}$	$7.222 \cdot 10^{-5}$
Half power	1.351	$5.914 \cdot 10^{-5}$	$3.889 \cdot 10^{-5}$
No power	1.280	$3.788 \cdot 10^{-5}$	$3.611 \cdot 10^{-5}$
Full power - cooled	1.355	$8.274 \cdot 10^{-5}$	-
Half power - cooled	1.341	$6.683 \cdot 10^{-5}$	-

6.2.3. Comparison with results from Sklavenitis' study

The experiments of Sklavenitis' study have been conducted with two different power settings: no heating power supplied (equivalent to the no power setting in this study) and 99.12W of heating power supplied (approximately in the middle of the full and half power setting in this study). The comparison has therefore been divided over the two power settings. For each power setting, a distinction has been made between the similarities of the experiments and the differences. This section addresses only the measured results from both studies, and not the theoretical conclusions drawn from these results. A brief discussion on the theoretical conclusions follows afterwards. The results are summarized below.

No heating power:
Similarities:

- The reservoir pressure and temperature follow the P,T-diagram. The pressure (6-7 mbar) is similar, but the temperature becomes lower (-1 to 0°C) in Sklavenitis' study, because less water is used in this study (0.5 kg vs 2kg in this study), see Figure 6.14a.
- The temperature near the upper reservoir and throat at t = 25 min is similar (approx. 10 °C).

Differences:

- The experimentally measured mass loss is on average 0.028 kg in Sklavenitis' study after 15 minutes of boiling, while approximately 0.065 kg was lost after 30 minutes of boiling in this study. Based on the measured temperature drop rate, more heat is lost in the beginning of an experiment, thus the mass flow rate decreases throughout the experiment. This shows that proportionally more water evaporated in this study, although 2 kg was used in this study instead of 0.5 kg in Sklavenitis' study.
- The temperature at the vent is also inconsistent between individual measurements, but in general (much) lower temperatures were achieved in Sklavenitis' study: around 15°C at the vent, where the vent temperatures are about 5-10°C higher in this study (see Figure 6.14b). This is most likely due to the fact that the experiments in this study were conducted during the summer, instead of the winter for Sklavenitis' study, causing large environmental temperature changes.

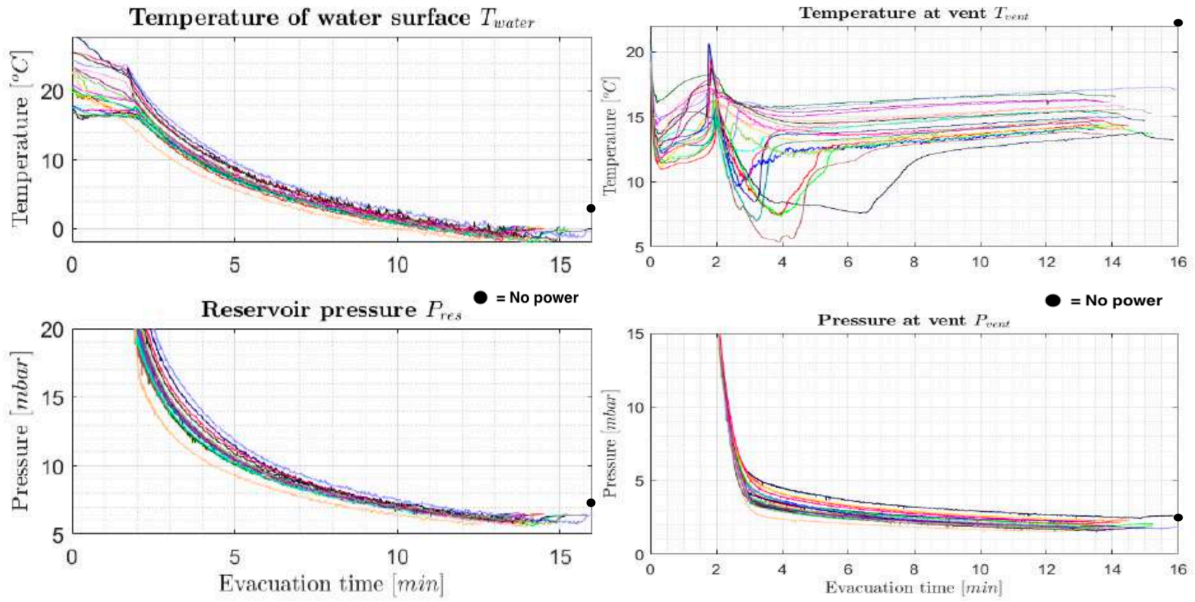

(a) The reservoir conditions with no heating power.

(b) The vent conditions with no heating power.

Figure 6.14: In the left and right figure, the reservoir and vent conditions of Sklavenitis' study without heating power are depicted, respectively. The black dot indicates the pressure and temperature measurements of this study, at t = 25 min. The surface water in Sklavenitis' study froze near t = 15 minutes, due to less reservoir water being used.

With heating power (99.12W):
Similarities:

- The reservoir conditions of Sklavenitis' study (temperature around 8-9°C, pressure around 11-12 mbar) are approximately equal to the reservoir conditions of the half power setting of this study, which can be seen in Figure 6.15a. The pressure and temperature follow the P,T-diagram. However, in Sklavenitis' study, 99.12W of heating power is supplied while 70W was supplied in this study. This confirms that there is a larger influence of external heat in this study. The reservoir water temperature at the start of the experiments fluctuates between 15-22°C in Sklavenitis' study, with most experiments starting at around 15°C, while in this study the starting reservoir water temperatures lies around 20°C. The temperature converges after 25 minutes to constant values, but it would explain a small portion of the difference with this study.

Differences:

- In Sklavenitis' study, the measured mass loss with 99.12W of power is 0.08 kg after 30 minutes, versus 0.07 kg with 70W and 0.13 kg with 140W in this study. Also here it is shown that in this study, relatively more water has evaporated.
- The temperature measurements at the vent with heating power are also inconsistent, and are between 8-14°C in Sklavenitis' study, see Figure 6.15b. In this study, the vent temperature is also 5-10°C higher, but this study also showed a lower temperature at the vent (1 or 2 °C) when more power is supplied. This effect is further analyzed and described in Section 6.7.3.

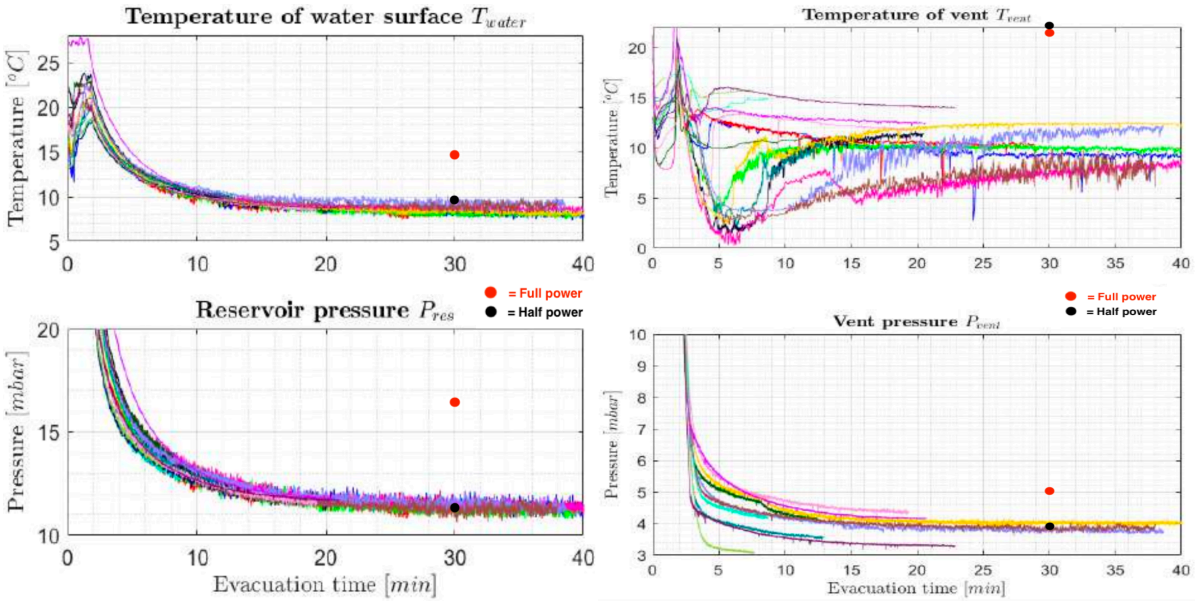

(a) The reservoir conditions with 99.12W of heating power.

(b) The vent conditions with 99.12W of heating power.

Figure 6.15: In the left and right figure, the reservoir and vent conditions of Sklavenitis' study with 99.12W of heating power are depicted, respectively. The red dot indicates the pressure and temperature measurements of the full power setting of this study, at t = 30 min. The black dot indicates the half power setting at t = 30 min.

In general, the reservoir conditions are similar for the two studies, while the vent conditions vary due to the different environmental conditions (room temperature, vacuum chamber pressure) and initial conditions (water temperature). The influence of the environmental temperatures on the setup is significant in both studies. In both studies, the flow is choked under all power settings, and condensation occurs only in the reservoir (before the throat). The Mach number calculations based on the temperature measurements were unreliable in both studies, and the Mach number based on the measured pressure ratios is similar with heating power, but higher in Sklavenitis' study (up to Mach 1.4 vs 1.28 in this study), likely due to the lower vacuum chamber pressure in Sklavenitis' study. Besides measuring the mass loss after an experiment to determine the mass loss rate, Sklavenitis' study also propagated a theoretical mass loss rate function based on the measured temperature drop rate, which resulted in an underestimation of the mass loss with no heating power supplied (by 30% to 52%), at $7.6 \cdot 10^{-6}$ kg/s to $1.1 \cdot 10^{-5}$ kg/s at 15 minutes. The mass loss rate with heating power (99.12W) is estimated within the uncertainty range of the experimentally measured mass, being $4.0 \cdot 10^{-5}$ kg/s to $4.1 \cdot 10^{-5}$ kg/s after 25 minutes. This means that with 99.12W of heating power supplied, the measured mass loss rate is similar in this study, while with no power supplied it is up to 3 times larger. In both studies and for all power settings, the mass loss rate based on the pressure ratio overestimated the mass loss by at least 11% and at most 50%. The difference between the mass loss rate equations and the experimentally measured mass loss indicates the presence of a thermal throat/thermal choking.

6.3. Effect of channel length

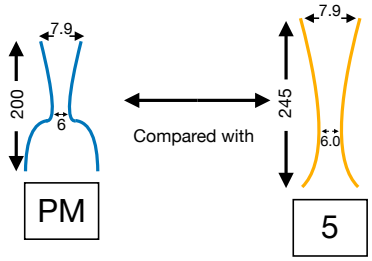

Figure 6.16: The tested models to determine the effects of an increase in channel length - plexiglass model and model 5.

To study the effects of an increase in channel length, model 5 is used. This model has a throat to vent length increase of 55 mm w.r.t. the plexiglass model, and the model is 245 mm in total instead of 200 mm, see Figure 6.16. The throat to vent ratio is equal, meaning that the same Mach numbers should be achieved, as the design Mach number only depends on the local channel area to throat area ratio. The model is also made out of a different material (polypropylene instead of plexiglass). Experiments conducted with this model can be divided into two categories: the first being at room temperature (or non-cooled) with the three different power settings, and the second after cooling the model, at (only) the half power setting due to time

constraints. The comparison between the pressure and temperature of the plexiglass model and model 5 can be seen in Figure 6.17, the pressure ratio and Mach number comparison in Figure 6.18 and the saturation degree comparison in Figure 6.19. The comparison for the half power setting between model 5 and the cooled model 5 can be seen in Figure 6.20.

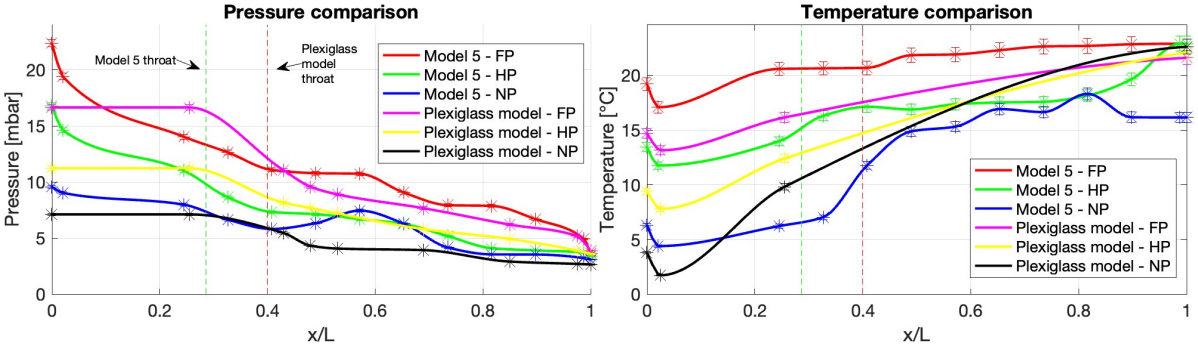

Figure 6.17: The comparison between the plexiglass model and model 5 for the pressure and temperature, for all power settings at t = 25 min. The green, vertical dashed line indicates the throat location of model 5, and the red, vertical dashed line indicates the throat location of the plexiglass model.

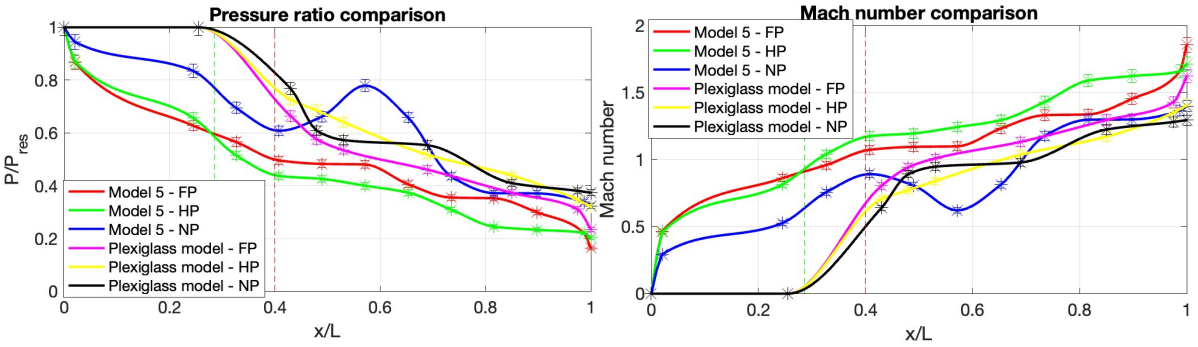

Figure 6.18: The comparison between the plexiglass model and model 5 for the pressure ratio and Mach number, for all power settings at t = 25 min.

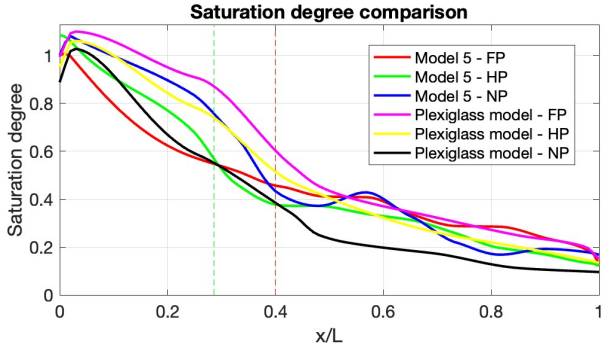

Figure 6.19: The comparison between the plexiglass model and model 5 for the saturation degree, for all power settings at t = 25 min.

For all experiments, the flow is choked, and the sonic points are at x/L = 0.35 for full power, x/L = 0.31 for half power, x/L = 0.69 for no power and at x/L = 0.4 for the cooled, half power setting. The geometrical throat is at x/L = 0.286. From the experiments with the plexiglass model it is expected that the sonic point is shifted upstream with increasing power, while it appears that this is not the case with the half power setting here. For comparison, the cooled half power setting also has its sonic point behind the full power setting. When comparing the downstream shift in sonic point with the plexiglass model,

the sonic points are more spread out over the channel for this model, meaning that the sonic point for full power is relatively closer to the geometrical throat, while the sonic point for no power is relatively further away from the geometrical throat. The pressure drop near the throat is also much less sudden for this model, because of the more gradual decrease in channel area. There appears to be a bump in pressure in the channel at around x/L = 0.58 for the no power setting. Whether this is caused by condensation is doubtful, because the degree of saturation is still low at that point (around 0.4). For the full power setting, a small pressure dip near the vent can be seen, which was also the case with the plexiglass model. This indicates that the nozzle is underexpanded for this setting. The inconsistency of the upstream shift in sonic point for the half power setting and the larger fluctuations in measurements, could also be attributed to the uncertainty in the measurements.

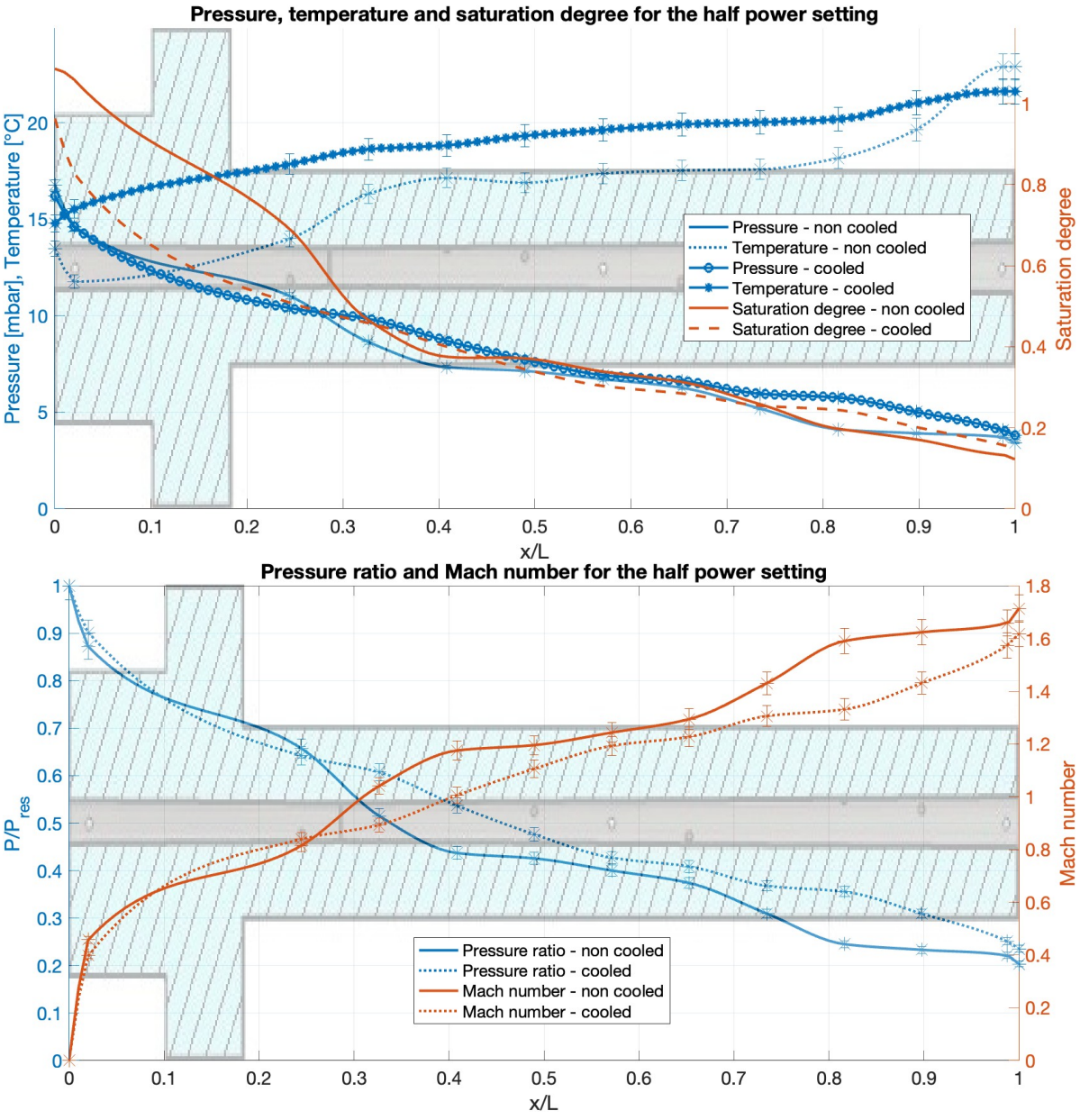

Figure 6.20: The comparison between the half power setting of model 5, cooled vs non-cooled at t = 25 min.

Cooling the model turned out to be less effective than cooling the plexiglass model, due to its (much) lower mass, giving it a much higher heat capacity. This model warms up quicker than the plexiglass model, and has a near-linear temperature increase as well. The temperature is still increasing at t =

25 min. The vent temperature at t = 25 min is 21.6°C compared to the 22.9°C of the non-cooled model. The vent temperature is also 22.9°C for the full power setting, while it is 16.2°C for the no power setting, again making the no power setting the statistical outlier. There is however a significant difference in reservoir conditions for this model, the reservoir temperature and pressure are higher regardless of cooling and for all power settings. Since the throat area is the same, the mass flow rates have become significantly higher as this depends on the reservoir conditions and throat area, see Table 6.3. In this table, it can also be seen that the isentropic Mach numbers at the vent are also significantly higher than the plexiglass model, due to the lower pressure ratio at the vent. The Mach number is also lower than the design Mach number of 1.993. The results contradict the expectations, as it was expected that the Mach number would have been lower due to the larger section that is heated from the environment. It is however likely that the changes in the mass flow rate and Mach number for the different models can be attributed to the additional heat convection at the walls. The results show a behavior similar to a smaller throat area, indicating that the additional heat ”pinches” the flow so that the flow is thermally choked with a thermal throat smaller than the geometrical throat.

Table 6.3: The isentropic Mach number at the vent and mass flow rate of model 5.

	Isentropic Mach number at vent [-]	Mass flow rate $\dot{m}$ [kg/s]
Full power	1.659	$1.157 \cdot 10^{-4}$
Half power	1.659	$8.769 \cdot 10^{-5}$
No power	1.366	$5.068 \cdot 10^{-5}$

In all settings the flow is not saturated throughout the channel, except for a small section at the inlet for the no power setting. It could be possible that vapor that condensed in the reservoir or the inlet, tends to evaporate again in the channel, of which the evaporative cooling forms solid particles when the absolute pressure dropped below the triple point pressure somewhere halfway the channel. This would explain the increase in pressure and temperature further in the channel because of the energy released by this process, assuming the density increased slower than the increase in temperature/pressure. The increased channel length and different material have nonetheless increased the mass flow rate and the (isentropic) Mach number at the vent. But because this model has a longer channel with thinner walls, the model is more prone to the environmental conditions, as mentioned before. When expressed in percentages, an increase in channel length of 45.8% (with an increase in total model length of 22.5%) and the different material resulted in a Mach number increase of 16.3% and a mass flow rate increase of 33.3% for the full power setting, a Mach number increase of 22.8% and mass flow rate increase of 48.3% for the half power setting, and a Mach number increase of 6.7% and mass flow rate increase of 33.8% for the no power setting.

6.4. Effect of channel diameter

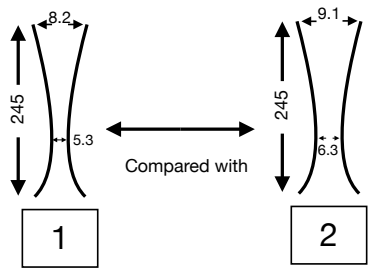

Figure 6.21: The tested models to determine the effects of an increase in channel diameter - model 1 and 2.

To study solely the effect of a larger channel diameter, the results of model 1 and model 2 are compared. They both have a converging-diverging channel with an expansion angle approximately equal to the plexiglass model, see Figure 6.21. Model 1 has a narrower channel with a throat diameter of 5.3 mm, while model 2 has a wider channel with a throat diameter of 6.3 mm. The comparison between model 1 and model 2 for the pressure and temperature is plotted in Figure 6.22, the comparison for the pressure ratio and Mach number is plotted in Figure 6.23 and the saturation degree comparison is plotted in Figure 6.24.

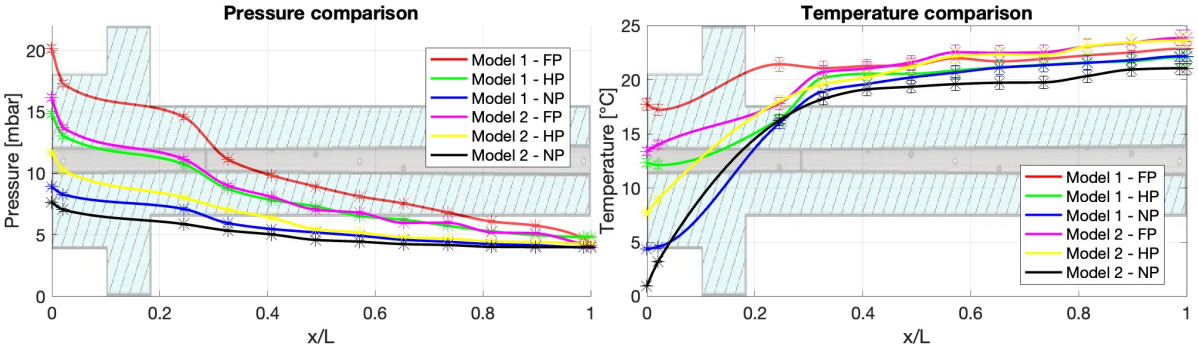

Figure 6.22: The comparison between model 1 and model 2 for the pressure and temperature, for all power settings at t = 25 min.

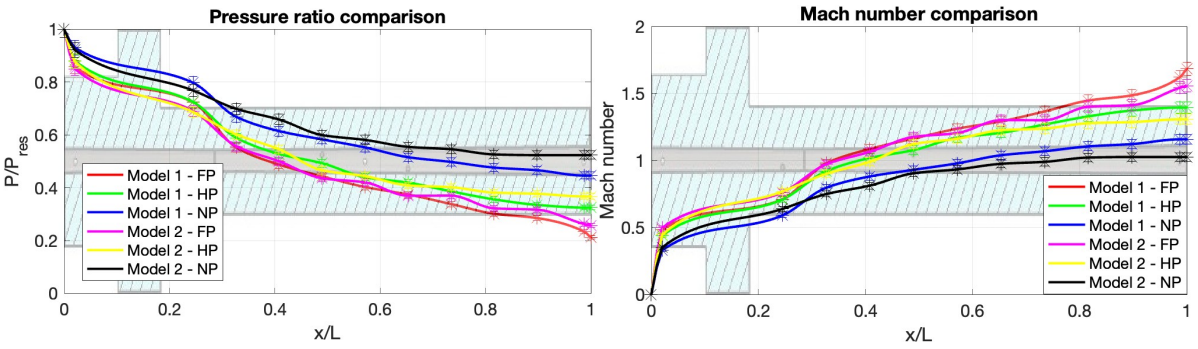

Figure 6.23: The comparison between model 1 and model 2 for the pressure ratio and Mach number, for all power settings at t = 25 min.

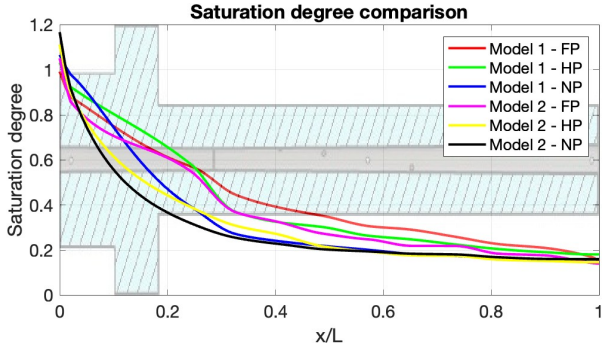

Figure 6.24: The comparison between model 1 and model 2 for the saturation degree, for all power settings at t = 25 min.

It can be seen that at the geometrical throat of model 1, there is a more clear pressure drop than model 2, which is something that is expected with an isentropic expansion. Model 2 has a nearly linear decrease in pressure throughout the channel. But despite this, the sonic points are nearly equal for the full and half power setting: x/L = 0.33 for model 1 full power, x/L = 0.34 for model 2 full power, x/L = 0.38 for model 1 half power and x/L = 0.41 for model 2 half power. There is a larger difference for the no power setting: here the sonic point is at x/L = 0.59 for model 1 and at x/L = 0.75 for model 2. The reservoir pressure and temperature at the no power setting are barely high enough for the flow of model 2 to become supersonic. The results show that the sonic point shifts upstream with a higher power setting, and even more with a narrower channel. The upstream shift in sonic point is likely because of the higher reservoir pressure and temperature, resulting in a more steep pressure ratio and the critical pressure ratio being reached more upstream in the channel. Still none of the points occur at the geometrical throat, likely due to the heat addition. For all power settings, the reservoir temperature is about 4-5°C lower for model 2 than for model 1, and the reservoir pressure is also lower,

but it has lowered proportionally: about 4 mbar lower for the full power setting, about 3 mbar lower for the half power setting and about 1.5 mbar lower for the no power setting. This means that there is a shift in the P,T-diagram, along the liquid-gas equilibrium line, as expected. The higher upstream pressure/temperature of model 1 resulted in higher (isentropic) Mach numbers at the vent than model 2, see Table 6.4. The design Mach number at the vent is 2.330 for model 1, and 2.190 for model 2. In the table it can also be seen that for all power settings, the mass flow rate (determined by the reservoir conditions, throat area and pressure ratio) is higher for model 2. Since the material and outer dimensions are the same for both models, the effects of friction are predicted to be equal for both model 1 and 2, as well as the heat addition from the environment. This means that a wider channel translates to a lower isentropic Mach number at the vent, and a higher mass flow rate, given that the initial and environmental conditions are the same.

Table 6.4: The isentropic Mach number at the vent and mass flow rate of model 1 and 2.

	Isentropic Mach number at vent [-]	Mass flow rate $\dot{m}$ [kg/s]
Model 1 - Full power	1.622	$8.165 \cdot 10^{-5}$
Model 1 - Half power	1.396	$6.063 \cdot 10^{-5}$
Model 1 - No power	1.160	$3.690 \cdot 10^{-5}$
Model 2 - Full power	1.543	$9.312 \cdot 10^{-5}$
Model 2 - Half power	1.308	$6.808 \cdot 10^{-5}$
Model 2 - No power	1.027	$4.504 \cdot 10^{-5}$

The models match the predicted results: the narrower channel resulted in a higher flow velocity, and the wider channel in a higher mass flow rate. When expressed in percentages: a throat area increase of 41.3% resulted in a Mach number decrease of 4.9% and mass flow rate increase of 14.1% for the full power setting, a Mach number decrease of 6.3% and mass flow rate increase of 12.3% for the half power setting, and a Mach number decrease of 11.5% and mass flow rate increase of 22.1% for the no power setting.

6.5. Straight channel

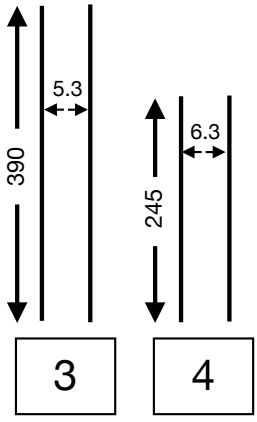

Figure 6.25: The straight channels - model 3 and 4.

Model 3 (a longer straight channel) and model 4 (a shorter straight channel) are analyzed to determine whether a converging-diverging section of a channel is necessary or that the estimated plume velocities from the Cassini measurements can be achieved with solely the effects of heat exhanges and friction inside the channel. The schematic model can be seen in Figure 6.25. The water level of model 3 is such that it is inside the channel instead of below it, to replicate the controlled boiling model (see the overview in Figure 6.26). The experiments with model 3 were done last, because the water inside the channel comes with a higher risk of damaging the measuring equipment.

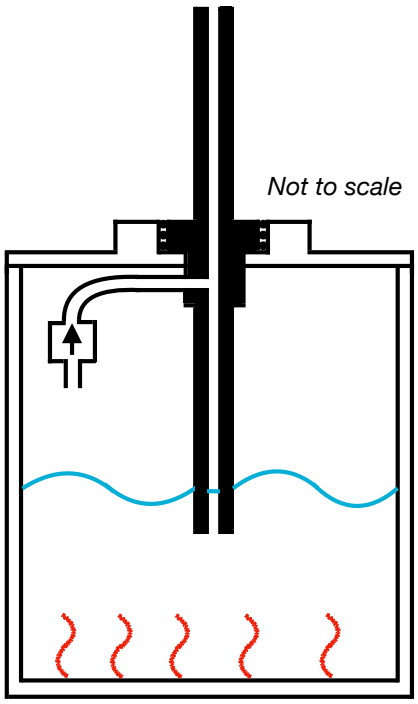

Figure 6.26: Schematic overview of model 3.

Unfortunately, the experiments with model 3 have failed. A plausible scenario of what happened during the experiments is as follows: First, the vacuum pumps start sucking the air out of the vacuum chamber. This creates a pressure difference between the chamber and the remaining air in the reservoir. The air in reservoir expands, and flows through the check valve (in the direction of the arrow) and through the channel back to the chamber. However, the air cannot flow out fast enough, either due to the channel diameter being too small, or the flow limit of the check valve has been reached. As a result, the pressure difference keeps increasing and the lid is pushed upwards (but does not come off), and the water in the reservoir is pushed downwards. The only way this water can go is up through the channel, so that the water level inside the channel rises. When it keeps rising, eventually the tube of the check valve is blocked with water, and any excess air in the reservoir cannot get out anymore. The evacuating chamber then directly sucks out the water through the channel, and this water stream is maintained (so only water comes out the vent, not air).

Model 4, the shorter straight channel, has been used to study the effects of friction and heat addition. The results (a comparison between the power settings) can be seen in Figure 6.27. In contrast to the previous models, the results of the straight channel are analyzed using the Fanno flow relations (for friction effects) and the Rayleigh flow relations (for heat addition effects).

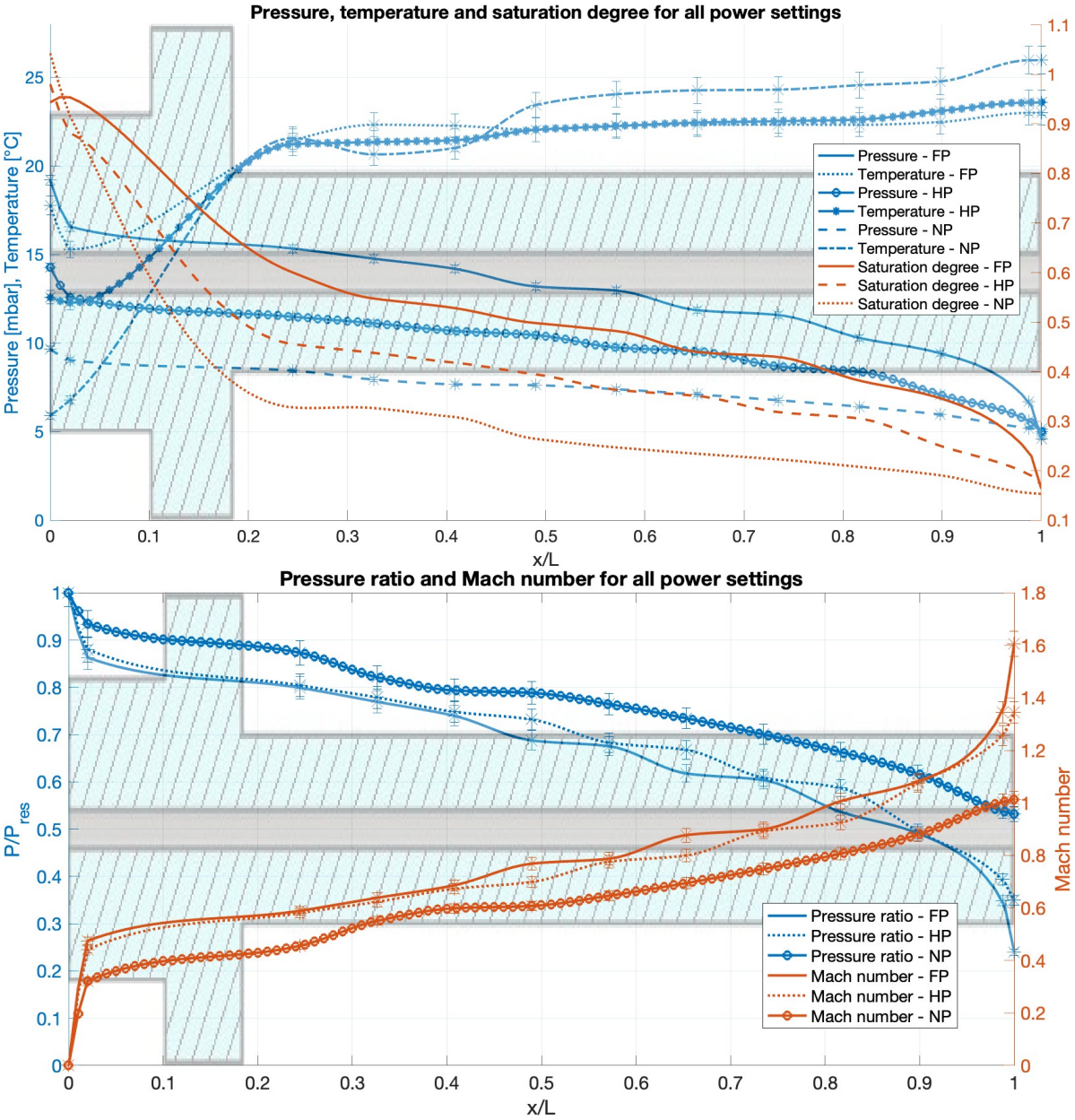

Figure 6.27: Model 4 - straight channel, Full, half and no power settings at t = 25 min.

Friction - Fanno flow

With the consideration of (only) friction in the channel of model 4, the isentropic solutions are by definition not valid due to the change in entropy. The isentropic relations could however give insight in the choking point in the channel, based on the pressure ratios following from the different power settings. According to these relations, the flow becomes choked at x/L = 0.81 with the high power setting, x/L = 0.86 for half power, and with no power the flow becomes sonic exactly at the vent (x/L = 0.99), as can be seen in Figure 6.27. From the results in the previous sections it has become evident that in general the sonic points shift more towards the (geometrical) throat with increasing reservoir pressure. With the isentropic relations, a similar behavior can be seen for this model. From Chapter 3 we know that friction moves the sonic point downstream, and that the flow cannot become supersonic by friction alone. To make the flow supersonic, a lot of heat has to be removed downstream the sonic point, which is not the case during the experiments.

The shear stress on the walls due to friction is defined as the shear stress coefficient times the dynamic

pressure, meaning that if compressibility effects have not (yet) been taken into account, the increase in shear stress at the walls is proportional to the square root of the flow velocity. In the subsonic flow region, the friction increases the velocity & Mach number, and decreases the pressure (and enthalpy), something that can be seen clearly in Figure 6.27. The isentropic solutions show that the sonic point shifts upstream with higher reservoir pressures. This would imply that a higher initial pressure in the channel increases the shear stresses on the walls, generating a larger boundary layer between the flow and the walls, 'squeezing' and thereby accelerating the flow towards Mach 1. This choking point occurs still relatively close to the vent, which makes sense because in case of frictional choking it is expected to occur more downstream the channel than the geometrical throat, as mentioned in Chapter 3. When it comes to choking the flow, the effects of friction are 'squeezing' the flow much less compared to having a geometrical throat. Following from the continuity equation, for higher reservoir pressures there is simply a higher (initial) pressure in the channel that can be converted into a larger flow velocity. The larger shear stress on the walls decreases the flow velocity in the vicinity of the wall, which means that the flow velocity away from the wall must increase in order to adhere to the continuity equation.

However, in Section 5.4.2 it is mentioned that if the flow becomes frictionally choked before reaching the vent, the flow is 'adjusted', so that the sonic point is shifted towards the vent. The choked duct length L^* can therefore be taken as 245 mm when using Equation 5.3 (repeated below for convenience, as Equation 6.1) to estimate the shear stress coefficient. The (isentropic) inlet Mach number is 0.48 for full power, 0.44 for half power and 0.32 for no power, which can be used as initial conditions together with channel diameter D of 6.3 mm and L^* of 245 mm to solve for the shear stress coefficient. For the full power setting, f = 0.0085, for the half power setting, f = 0.0116 and with the no power setting, f = 0.0303. This means that with a higher reservoir pressure, a lower friction coefficient is required in order to choke the flow at the vent. The friction coefficient is also a function of the Reynolds number and the relative roughness of the channel walls (which can be seen in a so called Moody diagram, see Figure 6.28), but the takeaway here is that since the relative roughness remains equal, the Reynolds number must be lower for a higher f. The Moody chart is used to estimate the mass flow rate in a channel with friction, and to estimate the pressure drop that is caused by this friction.

$$\frac{4fL^*}{D} = \frac{1-M^2}{\gamma M^2} + \frac{(\gamma+1)}{2\gamma} \ln\left(\frac{(\gamma+1)M^2}{2+(\gamma-1)M^2}\right) \tag{6.1}$$

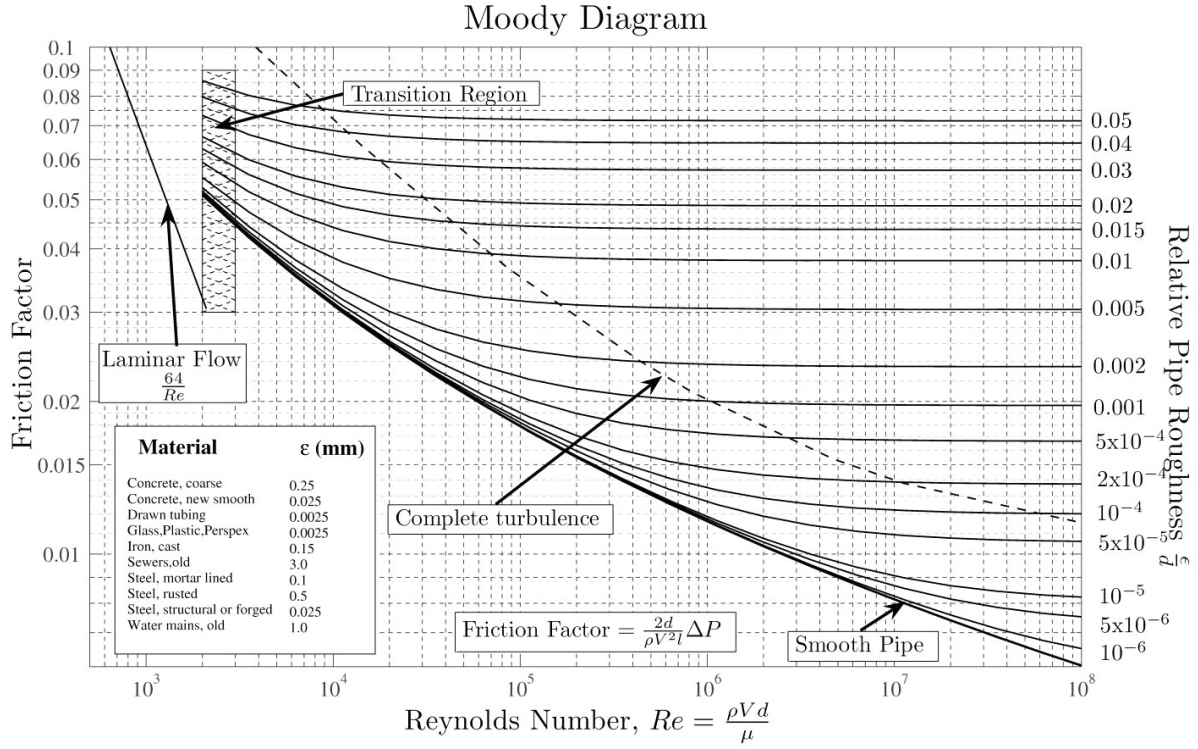

Figure 6.28: Moody diagram[1].

Because of the low kinematic viscosity of water vapor (here assumed to be 10^{-5} m^2/s - approximately the same as air[2]), the Reynolds number will be very large (in the order of 10^6) and therefore the flow will be turbulent regardless of the surface roughness. Judging by the manufacturing processes of the models and feeling their surface finish, the plexiglass model has the smoothest surface, followed by the PP model, and the PLA models have the roughest surface finish. The relative roughness for plexiglass is approximately $4{\cdot}10^{-4}$, which is the ratio ϵ/D, where ϵ - the absolute roughness - is assumed to be 0.0025 (from Figure 6.28) and D is the channel diameter, 6.3 mm. The other models will have a larger value for the relative roughness. Looking again at Figure 6.28, the friction factor plotted on the left y-axis is the Darcy-Weisbach friction factor, which is 4 times the aforementioned shear stress coefficient. Meaning that the full power setting has a Darcy-Weisbach friction factor of 0.034, half power setting a factor of 0.046 and the no power setting a factor of 0.121. From the diagram it can be read that for the full power setting, a relative roughness of approximately 0.007 is required, for the half power setting the relative roughness should be 0.015 and for the no power setting there is no solution. This means that to choke the flow at the vent, the channel has to have a roughness equivalent to a stainless steel pipe for the high power setting, a corroded steel pipe for the half power setting, and for the no power setting it would require a higher wall roughness than realistically used in practice. Although this is theoretically possible, the required roughness seems disproportionally high when comparing it to the roughness of the plexiglass model, making it unlikely that the flow becomes choked due to friction alone. Friction does seem to play a part in plume formation and sustaining the plumes, which will be further described in Chapter 7.

Heat addition - Rayleigh flow

In this case, the friction will be neglected, and only the heat addition to model 4 will be considered, assuming a Rayleigh flow. For all power settings, the flow through the short, straight channel does not become supersaturated, meaning that the measured temperature increment through the channel comes from external factors and not from condensation. When repeating the calculation process of the Rayleigh flow from Section 5.4.2 using the assumed inlet isentropic Mach number and the measured pressure and temperature as inlet and vent conditions, an estimation of the specific heat addition can be

[1] `https://commons.wikimedia.org/w/index.php?curid=4681366`
[2] `https://www.pipeflowcalculations.com/tables/steam.xhtml`

made for the different power settings. An overview can be seen in Table 6.5 where the Mach number at the vent is calculated as well as the required heat addition to match the measured pressure and temperature.

Table 6.5: Vent Mach number and required specific heat addition to acquire the measured vent pressure and temperature. Calculated using the Rayleigh flow equations.

Power setting	Full power	Half power	No power
Input:			
Measured inlet temperature [°C]	15.3	12.27	6.81
Measured inlet pressure [mbar]	16.57	12.58	9.04
Isentropic inlet Mach number [-]	0.475	0.441	0.320
Measured vent temperature [°C]	23	23.58	25.97
Measured vent pressure [mbar]	6.7	5.62	5.21
Output:			
Calculated vent Mach number [-]	1.291	1.169	0.855
Calculated required specific heat addition q [kJ/kg]	145.73	128.44	93.89

For reference, if the flow is assumed to be isentropic, the Mach numbers at the vent would be: 1.345 for the full power setting, 1.257 for the half power setting, and 1.00 without power. This means that the heat addition term lowered the (isentropic) Mach number at the vent, and without power the flow does not become choked at all. This is counter-intuitive, as the heat addition would accelerate subsonic flow and decelerate supersonic flow, and from the reservoir to the vent there is only an increase in temperature. However, just like the Fanno flow, if thermal choking occurs before the vent, the flow also becomes 'adjusted' so that the sonic point shifts towards the vent. More specifically: when the heat addition q exceeds the maximum heat addition to thermally choke the flow q_{max}, a series of pressure waves propagate upstream, so that the initial (inlet) conditions are adjusted such that the flow becomes sonic exactly at the vent [44]. Just as with friction, the heat addition reduces the total pressure and increases the flow velocity (when subsonic). The ratio between the required q and Mach number at the vent is about the same for each power setting: 145.73/1.291 = 112.88 for full power, 128.44/1.169 = 109.87 for half power and 93.89/0.855 = 109.86 for no power. This implies that to thermally choke the flow at the vent, q has to be at least 110 kJ/kg.

Now that q is calculated for the different power settings, multiplying q with the mass flow rate of each power setting will give the amount of energy added to the flow each second. The mass flow rate for the no power setting with M = 0.8546 is calculated using Equation 3.14, and the choked mass flow rate for the full and half power setting is calculated using Equation 3.15. The results are summarised in Table 6.6 below.

Table 6.6: Energy added to the flow to achieve the theoretical (Rayleigh) solutions.

	Specific heat addition q [kJ/kg]	Mass flow rate $\dot{m}$ [kg/s]	Heat addition/second [J/s or W]
Full power	145.73	$1.099 \cdot 10^{-4}$	16.011
Half power	128.44	$8.251 \cdot 10^{-5}$	10.598
No power	93.89	$5.456 \cdot 10^{-5}$	5.207

This shows that the required heat addition per second is surprisingly low to acquire the measured inlet and vent temperatures and pressures, and thus thermal choking can quite easily occur. It is also notable that the values for half power and full power are approximately two and three times larger than the value for no power, respectively. The thermal conductivity of the models is low and more or less equal (0.17-0.19 W/mK for plexiglass, 0.1-0.22 W/mK for PLA and PP [3]), but despite the low thermal conductivity it is possible for the flow to become thermally choked by the heat radiated from

[3] https://ctherm.com/resources/newsroom/blog/the-thermal-conductivity-of-unfilled-plastics/

the walls of the vacuum chamber alone. If we assume that the vacuum chamber walls radiate heat as a blackbody, the radiated heat can be calculated using: $q_{vac} = \sigma T^4 A$, where σ is the Stefan-Boltzmann constant (5.6703 $\cdot 10^{-8}$ W/m^{2}K^4)[4], T is the temperature of the walls (assumed to be 300 K, during a hot summer day) and A is the area of the vacuum chamber walls that radiates heat (inner area assumed to be 0.5 m^2). With these values, q_{vac} = 229.6 W, so there is 229.6 Watts of vacuum chamber inner wall heat radiated in every direction in the test section. The amount of energy absorbed by the test setup is much lower, since the temperature of the setup is already relatively high. But even with the low thermal conductivity and the small portion of radiated heat onto the surface of the small model, it is possible that the radiated heat, which is conducted through the model, can thermally choke the flow.

For the experimental setup, there will be a combination of both friction and heat addition, and the exact distribution between these factors is difficult to specify. In Chapter 7, a reflection will be given on the effects of the friction and heat exchanges of the models.

6.6. Diverging channel

Model 6 is used to study the effects of a larger expansion angle, with a solely diverging channel (see Figure 6.29. The reservoir serves as a pressurized chamber where, given sufficient upstream pressure, the flow becomes choked at the inlet of the model, which acts as a throat. The flow should then expand supersonically throughout the channel. The design (isentropic) Mach number at the vent is 3.43 - only if the flow is choked at the inlet/throat. The results for the model are plotted in Figure 6.30.

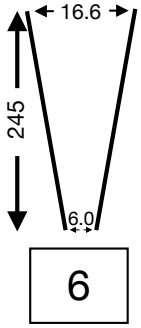

Figure 6.29: The diverging channel - model 6.

[4] https://www.engineeringtoolbox.com/radiation-heat-transfer-d_431.html

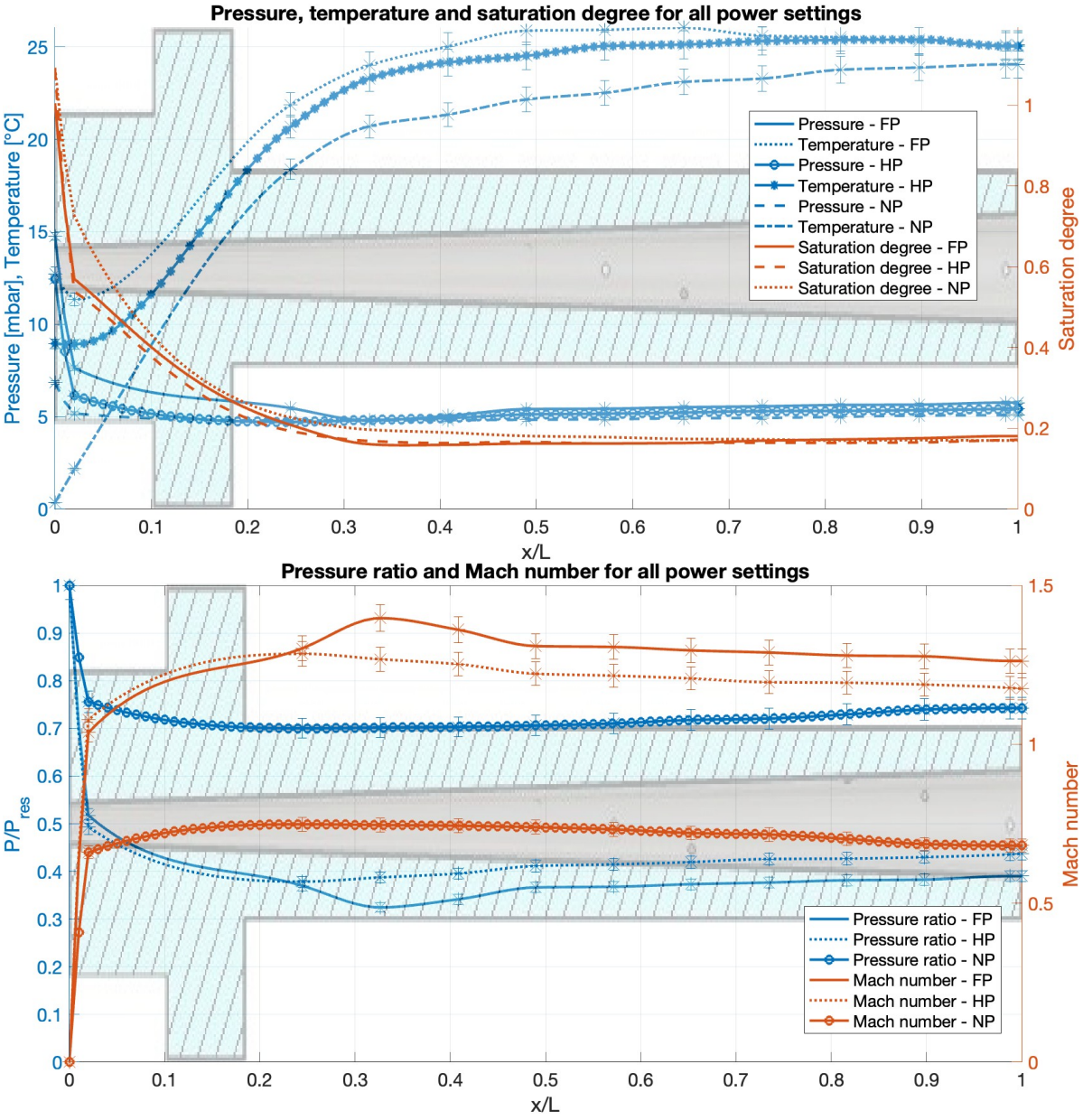

Figure 6.30: Model 6 - diverging channel. Full, half and no power settings at t = ± 25 min.

Because the first measurement point is at x/L = 0.05, it can immediately be verified if the flow becomes choked at the inlet, a condition necessary for supersonic expansion in the channel. It can be seen in the figure that this is the case for the full and half power setting, while for the no power setting the flow does not become choked and remains subsonic throughout the channel. With an isentropic Mach number at the vent of 0.681, it has the lowest velocity of all models and settings. Because the channel is also the widest of all models, the effects of friction and heat addition become relatively smaller compared to the other models, accelerating a subsonic flow only to a limited extent. The wider channel also resulted in the lowest reservoir pressure and temperature of all models and all power settings, implying that more energy of the reservoir water was lost because of boiling and evaporation. The results of this model show something that has not been seen before: the measured pressure in the channel is *lower* than the pressure in the vacuum chamber. For the full and half power setting, the temperature in the channel is also higher than the temperature at the vent. Because the pressure ratio is increasing after the flow has become supersonic, there could be either a normal shock, condensing vapor (a condensation shock) or flow separation due to an overexpanded nozzle. It is not expected that there is a normal shock since this requires a sudden increase in pressure and temperature, and it is also unlikely that there

is condensing vapor due to the low degree of saturation. This makes it plausible that the nozzle is overexpanded, and that the flow already separates from the wall quite close to the throat. When there is no flow separation, the pressure decreases after the throat, and the velocity increases. Conversely, if the pressure increases, a net force is opposing the flow and the velocity decreases, which is what can be seen in the plots. This effect is defined as an adverse pressure gradient [44]. In regions of an adverse pressure gradient, the boundary layer separates, explaining the measured pressure and temperature. It can also be seen that this separation occurs more downstream at the full power setting, starting at x/L = 0.33 instead of already starting before x/L = 0.24 for the half power setting. The flow separation results in the lowest (isentropic) Mach numbers at the vent compared to the other models, which can be seen in Table 6.7. The mass flow rates are also the lowest of all models, except for the half power setting: only the plexiglass model has a lower mass flow rate.

Table 6.7: The isentropic Mach number at the vent and mass flow rate of model 6.

	Isentropic Mach number at vent [-]	Mass flow rate $\dot{m}$ [kg/s]
Full power	1.263	$7.728 \cdot 10^{-5}$
Half power	1.177	$6.557 \cdot 10^{-5}$
No power	0.681	$3.296 \cdot 10^{-5}$

In order to reach high Mach numbers using the expansion angle of model 6 (around 2.5°), the upstream pressure needs to be much higher than achieved in this study. This expansion angle would also require either a large vent on Enceladus, or a very small throat, given that the channel length on Enceladus is much larger. This makes it unlikely that the expansion angle on Enceladus comes close to the expansion angle of model 6. The icy wall conditions on Enceladus would only worsen the effects of an adverse pressure gradient: the local friction effects would increase and the local Mach number would decrease further, making it unlikely that there is any kind of flow separation in the channels of Enceladus (assuming there are no obstacles in the channel, and the flow is supersonic) [54].

6.7. Evaluation of boundary conditions and design choices

To validate the results and put them into perspective, a selection of boundary conditions and design choices are evaluated. The analysis begins with an overview of the mass flow rates and isentropic Mach number at the vent for each model (Section 6.7.1). Next, the effects of a lower vacuum chamber pressure after the revision of the vacuum chamber pumps is given in Section 6.7.2. Then, the influence of the room temperature on the vent temperature is analyzed in Section 6.7.3. The effect of the throat diameter on the reservoir conditions is given in Section 6.7.4, and the effects of the measuring location of the thermocouples are discussed in Section 6.7.5.

6.7.1. Mass flow and (isentropic) Mach number at the vent

Before the evaluation of the boundary conditions and design choices, the model characteristics, mass flow rates and isentropic Mach numbers at the vent from the previous sections are summarized in Table 6.8. The evaluation will query the isentropic assumptions, and affect the results from the previous sections. Conclusions will be drawn in Chapter 8.

Table 6.8: Overview of all model characteristics, isentropic Mach numbers at the vent and mass flow rates. (C) indicates the cooled model.

Model	Plexiglass	1	2	4	5	6
Material	Plexiglass	PLA	PLA	PLA	PP	PLA
Channel type	Con.-Div.	Con.-Div.	Con.-Div.	Straight	Con.-Div.	Diverging
Total length [mm]	200	245	245	245	245	245
Throat-vent length [mm]	120	175	175	-	175	-
Inlet diameter [mm]	(49.2)	6.2	7.4	6.3	6.7	6.0
Throat diameter [mm]	6.0	5.3	6.3	-	6.0	-
Vent diameter [mm]	7.9	8.2	9.1	6.3	7.9	16.6
Vent-throat area ratio	1.734	2.394	2.086	1	1.734	-
Expansion angle [deg]	0.906	0.949	0.917	0	0.622	2.479
Converging angle [deg]	-	0.737	0.90	0	0.573	-
Isentropic M_{vent} - design	1.993	2.330	2.190	-	1.993	3.4285***
Isentropic M_{vent} - FP	1.427	1.622	1.543	1.00*	1.659	1.263
Isentropic M_{vent} - HP	1.351	1.396	1.308	1.00*	1.659	1.177
Isentropic M_{vent} - NP	1.280	1.160	1.027	0.855**	1.366	0.681
Isentropic M_{vent} - FP (C)	1.355	-	-	-	-	-
Isentropic M_{vent} - HP (C)	1.341	-	-	-	1.575	-
Mass flow - FP [kg/s]	$8.682 \cdot 10^{-5}$	$8.165 \cdot 10^{-5}$	$9.312 \cdot 10^{-5}$	$1.099 \cdot 10^{-4}$	$1.157 \cdot 10^{-4}$	$7.728 \cdot 10^{-5}$
Mass flow - HP [kg/s]	$5.914 \cdot 10^{-5}$	$6.063 \cdot 10^{-5}$	$6.808 \cdot 10^{-5}$	$8.251 \cdot 10^{-5}$	$8.769 \cdot 10^{-5}$	$6.557 \cdot 10^{-5}$
Mass flow - NP [kg/s]	$3.788 \cdot 10^{-5}$	$3.690 \cdot 10^{-5}$	$4.504 \cdot 10^{-5}$	$5.456 \cdot 10^{-5}$	$5.068 \cdot 10^{-5}$	$3.296 \cdot 10^{-5}$
Mass flow - FP - (C) [kg/s]	$8.274 \cdot 10^{-5}$	-	-	-	-	-
Mass flow - HP - (C) [kg/s]	$6.683 \cdot 10^{-5}$	-	-	-	$8.452 \cdot 10^{-5}$	-
*Reduced to M=1 because higher is theoretically impossible in straight channel without cooling						
**Rayleigh flow solution, ***Assuming the flow is choked at the inlet/throat						

6.7.2. Effect of lower vacuum chamber pressure

Throughout the experiments, it appeared that the performance of the vacuum pumps gradually worsened over time. The vacuum chamber pressure was initially already higher than during Sklavenitis' study with the plexiglass model, as the hole drilled for the extra pressure and temperature sensors introduced additional leaks. The higher mass flow rate of the experiments with full and half power settings resulted in a higher vacuum chamber pressure, as the pumps cannot keep the pressure low with higher mass flow rates. The vacuum pumps continuously pump out water vapor during the experiments, causing fluids to build up in the vacuum pumps, deteriorating their performance. This effect is significant: during one of the first experiments with the plexiglass model at the full power setting the vacuum chamber pressure was 3.89 mbar after 25 minutes. The last experiments conducted with model 6 reached a chamber pressure of 5.76 mbar with the full power setting at t = 25 min, close to the triple point pressure. The vacuum pumps had their periodic revision after the experiments, and an experiment has been repeated for the half power setting on model 5 (with the same throat to vent ratio as the plexiglass model), to determine the differences of the lower vacuum chamber pressure. The results are plotted in Figure 6.31.

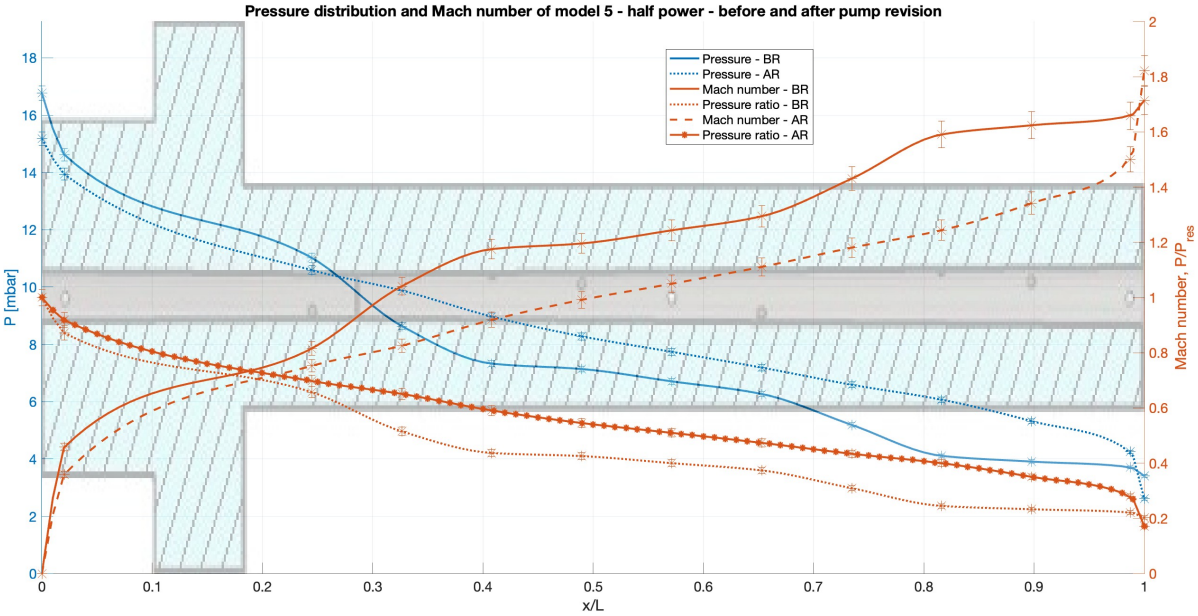

Figure 6.31: The pressure, pressure ratio and isentropic Mach number of model 5 (increased length, different material model) before and after the revision of the vacuum chamber pumps.

In this case we are only interested in the pressure, so the pressure, pressure ratio and isentropic Mach number (based on the pressure ratio) have been plotted using data before and after the revision. It should be noted here that before the revision, the experiments were conducted with room temperatures between 23 and 25°C, where the room temperature during the experiments after the revision was 20°C. The difference in chamber pressure is significant: the chamber pressure before the revision was 3.41 mbar, where it is 2.61 mbar after the revision. Surprisingly, the pressure decrease in the channel is more gradual after the revision, compared to a clear drop in pressure near the throat before the revision. As a result, the Mach number increase is also more gradual, shifting the sonic point downstream the channel. The isentropic Mach number is therefore lowered after the revision: M = 1.52 instead of 1.66. This is counter-intuitive as one would expect a higher flow velocity if the downstream pressure is lower. It can be seen that there is a pressure dip near the vent after the revision, meaning that for the half power setting after the revision, the nozzle became underexpanded, which could cause the decrease in Mach number. The design Mach number will not be reached and the flow will continue to expand after it exits the vent. This means that after the revision, it is expected that the performance (in terms of Mach numbers reached at the vent) of the full and half power settings would decrease as they are (or become) underexpanded, where the performance of the no power setting would increase, likely choking any non-choked flows during the study.

6.7.3. Influence of room temperature on vent temperature

Throughout the experiments it became evident that the room temperature played a large role on the thermal conditions of the setup. To assess whether there is a proven correlation between the vent temperature and the room temperature, the vent and room temperatures of all experiments were logged and plotted in Figure 6.32. The lines indicate the linear fit between the data points. The vent temperatures of the cooled models were left out, as they would automatically become the statistical outliers.

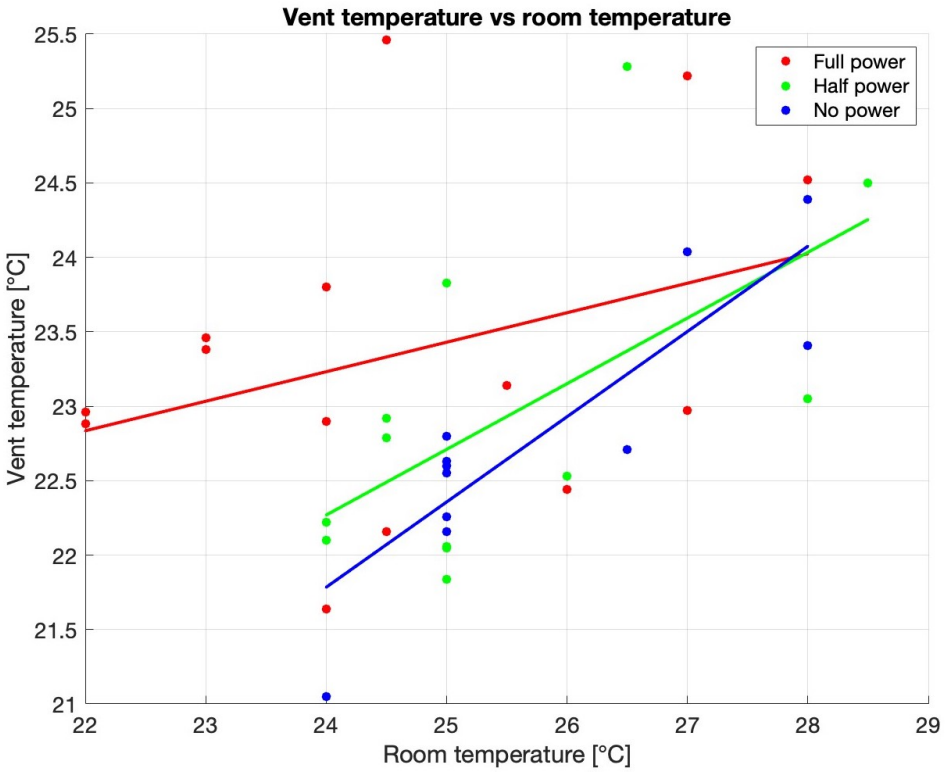

Figure 6.32: The vent temperature plotted against the room temperature. The cooled models were not included.

The correlation for the full power setting is 0.3403, for the half power setting it is 0.6018 and for the no power setting it is 0.8673. This means that when less power is supplied, the correlation between the vent and room temperature increased, and became high when no power is supplied. This confirmed the suspicions during the experiments, that the room temperature has a large influence on the results of the vent temperatures. The larger mass flow for the higher power settings apparently have a cooling effect. The vapor in the reservoir is relatively cold compared to the model itself, meaning that the vapor actively cools the model and gives colder readings. This could also explain the (much) lower temperature readings of the plexiglass model during Sklavenitis' study, when the experiments were conducted during the winter. The behavior shown in the plot could also be partially caused by the placement of the thermocouples. The effects of changing the location of the temperature sensors are discussed in Section 6.7.5.

6.7.4. Effect of throat diameter on reservoir conditions

When comparing the results of model 5 (the increased length, different material model) with the results of the plexiglass model, it became clear that model 5 had much larger mass flows compared to the plexiglass model, while the throat diameter is the same. Once the flow is choked, the mass flow is mainly determined by the throat diameter and the reservoir conditions. But whether the reservoir conditions were solely determined by the throat diameter, regardless of the channel geometry, is still unclear. The experiments have shown that when more heating power is supplied, the sonic points shifts upstream. It is also suggested that with less power supplied, relatively more heat is added to the setup from the environment. Therefore, the throat diameter is plotted against the measured reservoir temperature for each model to determine their correlation, and can be seen in Figure 6.33.

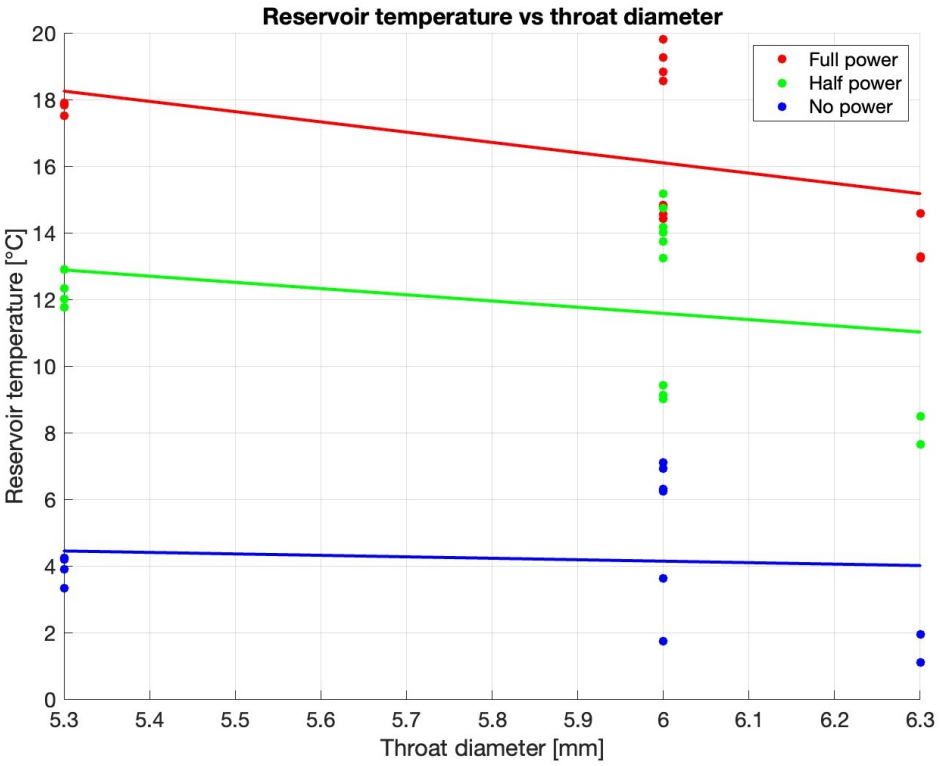

Figure 6.33: The reservoir temperature plotted against the diameter of the throat.

Again, a linear fit of the data points is plotted for each power setting. There were only 3 different throat diameters used in this study, but there still appears to be a trend: the correlation for the full power setting is -0.5070, for the half power setting it is -0.2703 and for the no power setting it is -0.0847. Although there is no direct correlation and the temperature also depends on the flow conditions, it gives a clear indication that when more power is supplied, proportionally more heat is lost for larger diameter throats. Since it is expected that more heat is lost for setups with a higher reservoir pressure and larger throat, the flattening of the curve for the no power, larger diameter throat indicates that when the temperature gets close to the freezing point, relatively more heat from the environment is absorbed by the reservoir. This makes sense, but again shows the significant contribution of the environmental temperatures.

6.7.5. Effect of temperature sensor location

As mentioned before, the temperature results indicated that besides the actual flow temperature, the temperature of the model itself had a significant influence on the temperature readings. The thermocouples were placed inside the wall along the flow during the experiments, while for this analysis the temperature sensors were placed in the middle of the channel of model 5 (half power), to study the effects of the temperature sensor measuring point. However, the temperature readings of the different configurations for the same power setting were too inconsistent to make a meaningful plot. The readings did have something in common: the measured vent temperatures were exactly the same as when measured along the walls. There was a more clear heat bump visible of around 0.75-1.00°C near x/L = 0.75-0.85. Except for model 6, there was no evidence for temperatures inside the channel that were higher than the vent temperature, although the difference for model 6 was only small while it is significant in this experiment. This heat bump does give reason to believe that there is flow condensing more downstream in the channel as opposed to what is predicted before, or that the condensed vapor upstream in the channel froze when the pressure is reduced beyond the triple point pressure downstream the channel, and the thermocouples were able to pick up the latent heat release of this process.

Because of the inconsistent measurements, it is not advisable to measure the flow in the middle of the channel. Besides the obvious obstruction/disturbance of the flow, the thermocouples are also more

prone to being struck by icy particles, making the readings invalid afterwards.

6.8. Comparison with Computational Fluid Dynamics model

Parallel to this study, a numerical analysis on plume formation has been conducted by T. Fontes. Although the numerical analysis is originally performed for channels of 1 m in length and on 'Enceladus-scale', the parameters were scaled down to the proportions of the models used in this study to make a comparison between the CFD model and the experiments in the vacuum chamber. Two simulations have been conducted, where the first simulation assumed an adiabatic wall with no friction, where condensation occurs in the channel. Because of the apparent large deviation from the isentropic temperatures during the experiments, the second simulation assumed an isothermal wall (at 22°C) with friction effects, so that the wall temperature is uniform along the channel and heat exchanges between the wall and the flow. The results are combined into one plot, and can be seen in Figure 6.34.

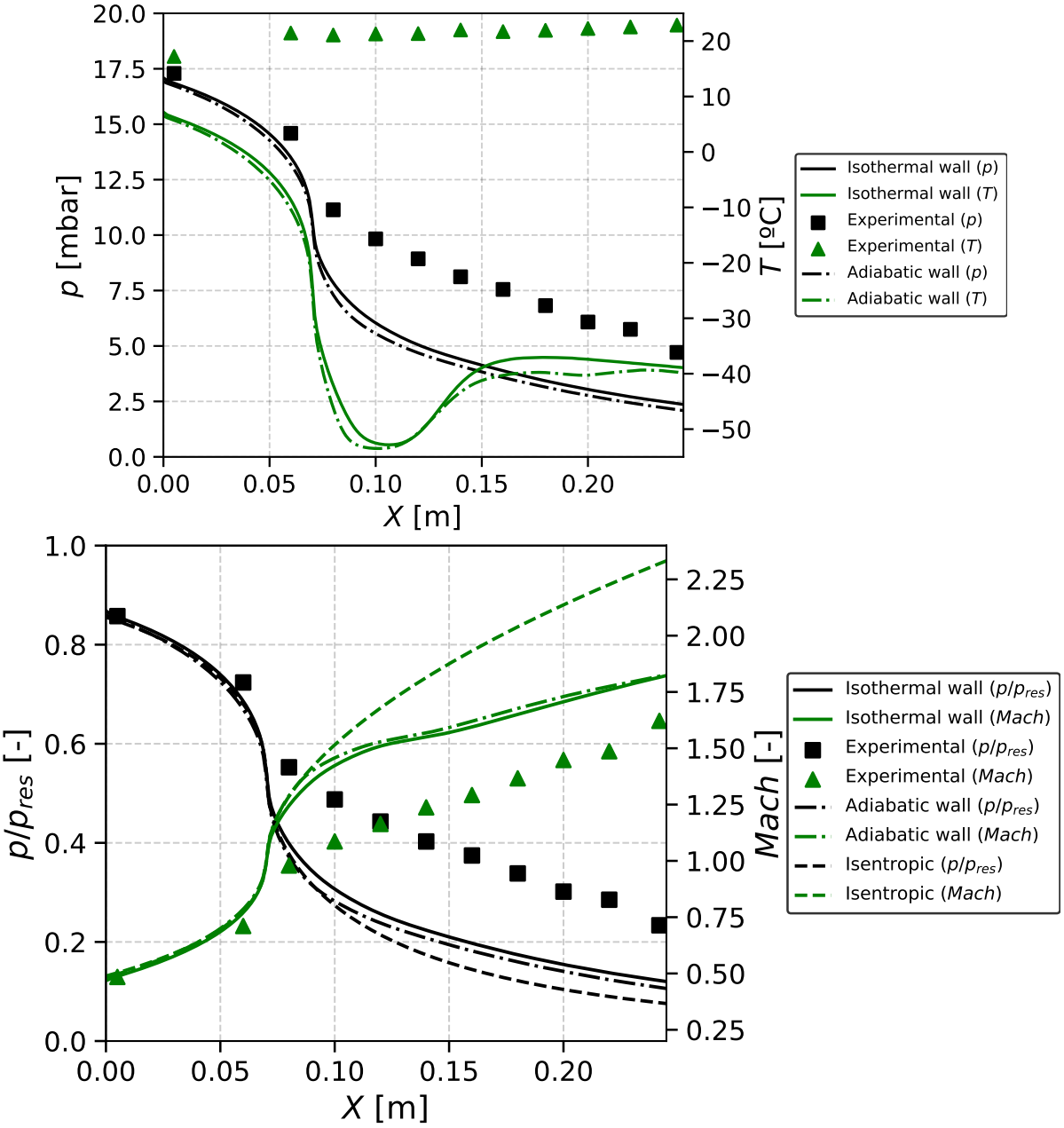

Figure 6.34: The results of the CFD model. The top figure shows the absolute pressure and temperature, and the bottom figure shows the pressure ratio and Mach number. The plots are made by T. Fontes.

The results are compared using the data from model 1, at the full power setting. The values of the simulation are the values from the center of the channel, where the values from the experiments are the measurements along the wall, so this location difference should be taken into account. The friction of the isothermal wall is modeled as a no-slip condition: the viscosity makes the flow velocity go towards zero relative to the wall, so together with the isothermal wall this causes a temperature, pressure and velocity gradient from the walls to the center of the flow. In the plots it can be seen that the isothermal wall slightly increases the absolute pressure and temperature, and slightly decreases the Mach number. It can also be seen that the pressure at the vent for the simulation is around 2.5 mbar, while it is nearly double that during the experiments. As a result, the acceleration of the flow after the throat is much less than the theoretical values. From the experimental data in the previous sections it became evident that a larger upstream pressure shifted the (isentropic) sonic point more towards the geometrical throat, and it can be seen here that a lower downstream pressure also has this effect. The predicted temperatures of the simulation are much higher than the isentropic temperatures, but still much lower than the measured values during the experiments. The lowest value is below -50°C, while the wall temperature is simulated at 22°C, meaning that over a (radial) distance of around 2.7 mm in the channel (from the wall to the center of the channel) the temperature drops over 72°C, which is a temperature gradient that is unlikely to be achieved in the lab. Because of the high flow velocity (and thus limited effects of conduction within the flow), the partially condensed vapor at the reservoir and the reduced flow acceleration after the throat (due to the higher P_{vent} of the experiments w.r.t. the simulation), it can be concluded that the assumptions made for the simulations are not sufficient to represent the thermodynamic properties of the experiments. It is likely that the largest contributor to this deviation is the fact that the experimental setup has the reservoir beneath the model, and the simulation assumes only an initial temperature and pressure. This means that the vapor in the reservoir was already supersaturated, so that condensation already occurred at and before the inlet of the model. The consequences of this for each specific model have already been discussed in the previous sections. Although the simulation does take condensation into account, it only occurs after the throat when the temperature dropped a lot, while in the experiments latent heat is already being released at the inlet.

6.9. Heat exchanges

In the previous sections it has become evident that besides the temperature of the flow and the reservoir water, there are multiple other sources of heat which affect the flow properties. All heat exchanges are discussed below.

The reservoir and model are placed on an aluminum, rectangular (160x130 mm) lifting table in the test section of the vacuum chamber. The table has a flat surface on the top and bottom, so the bottom is equal to the temperature of the vacuum chamber and the top conducts a small amount of heat to the plexiglass of the reservoir. The metal inside the test section of the vacuum chamber radiates heat onto the plexiglass of the reservoir, and the model placed on top. This metal slightly increases in temperature throughout an experiment, as the vacuum pumps generate heat and warm up the surrounding air. At the bottom of the reservoir water, the heating foils generate heat and warm up the water. The heat circulates in the water through convection. Because the water temperature becomes (much) lower than the room temperature, the radiation and conduction from the test section add heat to the model. The heat released by the plexiglass walls onto the reservoir water is assumed to be negligible, as this would be equal to the initial reservoir conditions. It is estimated that without heating power and with colder room temperatures (during winter), the average power received by external sources is 32 ± 10W [47]. With 100W of heating supply, this power becomes less: 19 ± 7W after 10.6 min of boiling, 14 ± 6W after 18.5 min and 11 ± 6W after 38.6 min. Even though this energy is 'absorbed' by the reservoir, if a similar amount of energy is radiated onto the model, and in turn conducted through the model to the flow, it is demonstrated in Section 6.5 that this would (theoretically) be sufficient to thermally choke the flow, depending on the power setting.

Because the boiling/evaporation is an endothermic process, the temperature of the water vapor just above the water surface is slightly lower than the liquid water. The results for all models have shown that in the upper reservoir all the way to either the inlet or the throat of the model, condensation occurs, which is exothermic and releases latent heat, warming up the flow again. Using Equation 6.2 (which is

Equation 3.16 where the parameters are described, repeated below for convenience) the solid fraction is determined for the plexiglass model, which can be seen in Figure 6.35.

$$f_x = \left(1 + \frac{\Delta h_{vap}}{\frac{1}{2} \cdot v_x^2 + c_{p,x} \cdot T_x - c_{p,res} \cdot T_{res}}\right)^{-1} \tag{6.2}$$

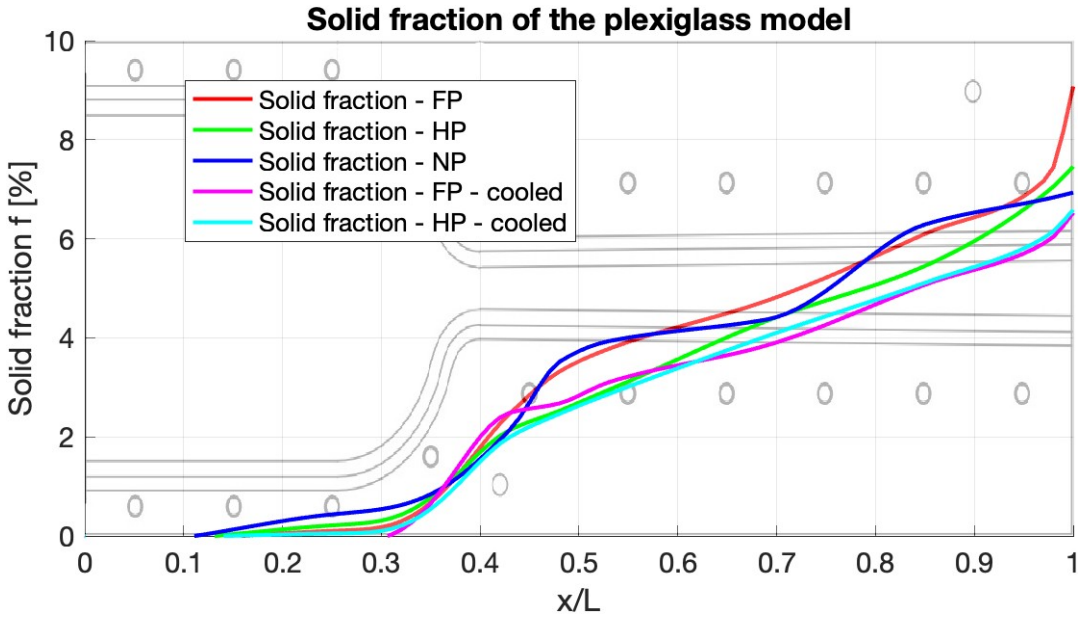

Figure 6.35: Solid fraction of the plexiglass model, for all power settings (at t = $\pm$ 25 min). Solid fractions are given as a percentage of the total flow.

It can be seen in the figure that the solid fraction does not really change when a different power setting is selected, but the cooled model does clearly lower the solid fraction curve. It makes sense from the used equation, but the increase in solid fraction indicates that there is still vapor condensing downstream the throat, or particle growth (nucleation). This contradicts the saturation degree curves from the previous sections, which have shown that the saturation degree is well below 1 for all models from the inlet or throat on, implying that there is no more condensation occurring after this point. The temperature readings of the thermocouple do however increase further downstream the channel, but whether this is caused by condensing vapor and/or the measuring location and the influence of convection and radiation on the thermocouple cannot be determined by these readings alone. This would require an additional study on either the thermal radiation of the test section or on how to accurately measure the temperature of a high velocity flow.

7

Implications for Enceladus and discussion

This chapter focuses on determining the 'bigger picture' of the experiments: the implications for Enceladus. First, the results of the experiments are discussed and the implications for Enceladus based on these results are described in Section 7.1. Then, the additional thermal processes that occur on Enceladus and not in the laboratory are modeled and described in Section 7.2. In the last section, the outcome of the first two sections are linked to Enceladus, to determine whether the plume characteristics of Enceladus can be recreated.

7.1. Implications based on the experimental results

On Enceladus, the tides play an important role in the intensity of the plumes, as described in Chapter 2. The compressing ice shell causes the water level to rise inside the channel, pushing the vapor inside the channel upwards towards the vent. The back pressure - the force working against the flow direction - is caused by friction on the walls, and controls the water evaporation rate. This would require a straight channel, and no reservoir present. Although the experimental setup does not recreate the tides, and has a reservoir present, the effects of friction are noticeable. Because of the natural formation of the crevasse, it is unlikely that 'perfect' straight channel shapes are formed, implying that the vapor will cover a larger distance from the liquid-gas interface to the vent as it is not a straight line. This increases the area where friction occurs and where heat is generated by condensing and nucleating vapor. The longer friction area increases the pressure of the flow, increasing the subsonic flow velocity and decreasing the supersonic flow velocity. The generated heat from the condensing vapor is absorbed by the icy walls and radiated into space. From the experiments it could be seen that the reservoir conditions played an important role on the vent temperature and the mass flow rate. The estimated heat loss and mass flow rate based on Cassini's measurements could therefore put constraints on the minimum or maximum reservoir (if present) pressure and temperature, and the throat area, similar to the experiments in this study.

Besides the tides, the low gravity on Enceladus is also a factor that cannot be reproduced in a laboratory, although the effects are negligible on the scale of a model used in a vacuum chamber. However, the throat to vent ratio or expansion angle of a model can be easily changed, while on Enceladus it would require either a very small throat or a very large vent when using similar ratios, because of the much larger crevasse length. The icy wall conditions on Enceladus would also worsen the effects of an adverse pressure gradient if the flow separates from the channel walls, as discussed in Section 6.6. Because of the expected irregular crevasse shape, it is unlikely that larger throat to vent ratios are present on Enceladus. On Enceladus, the flow expands into a full vacuum, greatly increasing its velocity while in the lab the expansion is limited to the vacuum chamber pressure. The experiments conducted after the revision of the vacuum chamber pumps made most channels underexpanded and actually lowered the (isentropic) Mach number at the vent. This effect is thus expected to be more severe on Enceladus,

implying that the geometry of the crevasse would partially determine the vent velocity, but the crevasse will most likely be underexpanded because of the limited expansion angle. Cassini also determined the plume velocity based on the measurements when the plume already expanded into a vacuum, meaning that the velocity at the vent is lower than the velocity at a higher altitude [36], something that can also not be determined in the vacuum chamber.

In the lab, the extremely cold temperatures of Enceladus can also not be recreated, unless a setup can be made such that the walls are cooled by using liquid nitrogen, for example. This does however mean that there is no vapor condensed or deposited on the walls of the experimental setup, while this does happen on Enceladus. Where on the experimental setup heat is added to the flow, the velocity of the subsonic flow is increased, and the velocity of the supersonic flow is decreased. It is not possible in the lab to make supersonic flows with the straight channel if there is only heat addition. The extreme cold on Enceladus removes heat from the flow, greatly accelerating supersonic flow. The isentropic vent temperature (for the design Mach numbers discussed in the previous chapters) is around -100°C, and the temperatures on Enceladus are near this temperature when flowing towards the vent. Because of the relatively small differences in flow properties when the geometry of the experimental setup changed, it is plausible that the flow characteristics are dominated by the thermal effects rather than having a specific channel geometry in order to reach a certain vent/plume velocity.

In order to test the above statements, a hypothetical case is discussed in the next section. Here, the (thermal) processes that do not occur in the experimental setup but are present on Enceladus are included, to determine the implications for Enceladus.

7.2. Additional processes on Enceladus

In the results from Chapter 6 it became evident that a supersonic plume cannot be recreated in the laboratory with a straight channel, as it would require heat removal of the flow after the sonic point in the channel. In the laboratory, only heat is added to the flow, whereas on Enceladus, the walls draw heat from the flow and heat is generated only by the condensing vapor. On Enceladus, there is also more time in the channel to transfer heat from the flow to the walls, compared to the experimental setup. The wall interactions, condensation and friction play a large role in the formation of the plumes. In this section, these processes are taken into account to determine whether a straight channel with cold walls could recreate the plumes, and whether a high-pressure reservoir is necessary to recreate the plumes. The following hypotheses are therefore tested, by conducting a numerical simulation:

- Hypothesis A: Is a pressurized reservoir necessary to recreate the plumes?
- Hypothesis B: Is a geometrical throat required to recreate the plumes?

Following on from the implications from Section 7.1, a 1000 meter long straight channel is assumed. The channel diameter is 1 meter, and it has no pressurized chamber underneath. The channel dimensions are in the order of magnitude used in the controlled boiling model from Chapter 2. For the temperature of the channel, 272 K is assumed at the liquid-gas interface, and 200 K at the vent, equal to the channel in Figure 2.10, and depicted in Figure 7.1a for convenience. One of the processes that occurs on Enceladus but not in the laboratory, is wall accretion of the vapor. Because the vapor has more internal energy than the icy wall, the accretion reduces the energy of the flow, and releases latent heat. However, only a relatively small amount of energy is released compared to the energy of the flow, so it can be assumed that the heat is conducted through the ice [29]. There is also sublimation from the walls to the vapor, which should increase the energy of the flow and has a cooling effect. But because of the low temperatures, the effects of sublimation are expected to be negligible compared to the energy of the flow. It is assumed that there is a gradual decrease in temperature from the ocean to the vent, with the wall temperature being equal to the flow temperature, meaning that the convective heat transfer with the walls is already taken into account. For the linear temperature decrease from 272 K to 200 K, the local speed of sound and solid-gas equilibrium pressure is plotted in Figure 7.1b. The figure shows that the speed of sound reduces towards the vent, so if the flow velocity remains equal, the Mach number would increase. Because of the low equilibrium pressure at the low temperatures, the flow is supersaturated in a large part of the channel, and only consists of vapor and ice. The solid fraction on Enceladus is between 10% and 20% [34], and is assumed to be 10% for the simulation.

Enceladus' mass flow rate of 150-300 kg/s [11, 12] is assumed to be 150 kg/s for the simualtion. It should also be noted that the 10% solid fraction reduces the local speed of sound by approximately 8% [36]. The plume velocity is in the range of 350-950 m/s [3, 4], which is what should be achieved with the simulation.

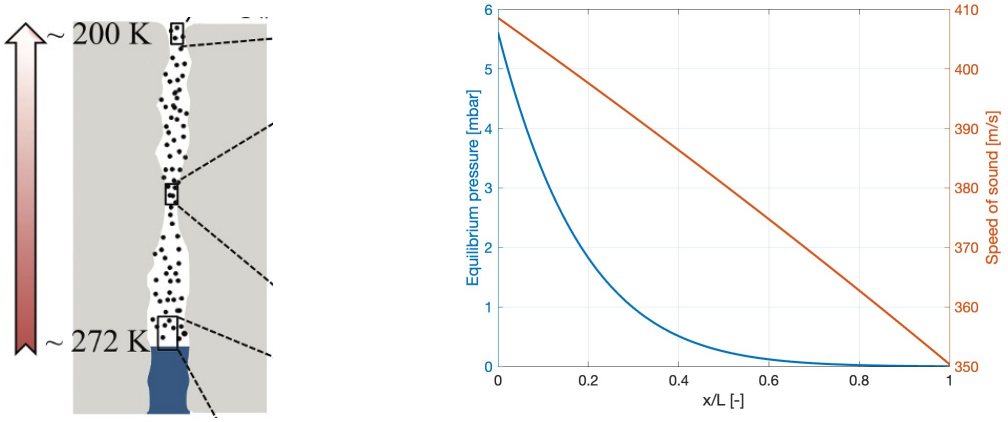

(a) The assumed gradual temperature decrease in the channel [31].

(b) The speed of sound and the solid-gas equilibrium pressure for the assumed temperatures in the channel.

Figure 7.1: In the left figure, a sketch of the channel with the gradual temperature decrease is depicted, with the speed of sound and the solid-gas equilibrium pressure at those temperatures depicted in the right figure.

The flow is expected to have a subsonic and supersonic region, where a formed throat separates the two. The throat is created by the combined effects of the latent heat release of condensation, and wall friction. The subsonic region is thus from the liquid-gas interface to the (thermal) throat. In this region, it is assumed that there is only non-equilibrium condensation, meaning that the pressure increase due to condensation only occurs in this section. All the heat that is generated is converted into kinetic energy. For this region, the Rayleigh flow relations are used. The friction (for subsonic flow) decreases the pressure, and increases the velocity. For this, the Fanno relations are used. In the supersonic region, so from the (thermal) throat to the vent, it is assumed that there is only equilibrium condensation, i.e., grain growth. In this region, there is no increase in pressure or heat. It is therefore assumed that this region is adiabatic, or that q = 0. Usually in the supersonic flow region, friction increases the pressure and reduces the flow velocity. But because the flow is nearing the vacuum of space, it is assumed that this effect is cancelled out in this region. In the supersonic region, the Rayleigh flow relations are used, without a change in stagnation temperature, so that only the decrease in temperature of the flow accelerates the flow in the supersonic region. The change in Mach number per change in channel distance is given by Equation 7.1, and is propagated using Euler's method.

$$\frac{dM^2}{dx} = M^2 \frac{1 + \frac{\gamma-1}{2}M^2}{1 - M^2} \left[\frac{1 + \gamma M^2}{T_0} \frac{dT_0}{dx} + \frac{4\gamma M^2 f}{D} \right] \tag{7.1}$$

Where γ = 1.33 and D, the channel diameter, is 1 m. The stagnation temperature T_0 at x = 0 (the liquid-gas interface) is 272 K. The initial Mach number is assumed to be 0.1 (compared to the M = 0.2 used by Schmidt et al. [40]). f is the friction coefficient, which increases with lower temperatures. f = 0.1 at -40°C, which is the value assumed in this simulation [55]. This value is about 3 times higher than the value found for the 'no power setting' during the experiments - which best represents the pressure distribution in the simulation. dT_0/dx is the change in stagnation temperature along the channel (in K/m), and the change itself is defined as $T_{0,2} = T_{0,1} + q/c_p$, with c_p assumed to be 1.86 kJ/kgK. The specific heat addition q is defined as Q/m, the heat addition per unit mass. q can be written as (dQ/dt)/(dm/dt), where dQ/dt is defined by multiplying the total latent heat release from vapor to solid (2835 kJ/kg) with the 0.15 kg/s of solid particles leaving the vent (from the 150 kg/s divided over 101 identified jets, with a 10% solid fraction). The dm/dt is thus the total mass flow of an individual jet, assumed to be 1.5 kg/s. $T_{0,2}$ can then be calculated, being 424.42 K at the (thermal) throat. dT_0 is thus 424.42 - 272 = 152.42 K. Using an iterative scheme where the choking point of a previous iteration is the 'dx' term of the new iteration, the scheme converged after 5 iterations at a dT_0/dx value of 1.212 K/m, and a choking location at 125.75 m in the channel. The supersonic region is then modeled using Equation 7.2.

$$\frac{T}{T^*} = M^2 \left(\frac{1+\gamma}{1+\gamma M^2} \right)^2 \tag{7.2}$$

Where the initial Mach number is 1, and the wall and flow temperature at x = 125.75 m is 263 K, which is T^*. The resulting Mach number throughout the channel is plotted in Figure 7.2.

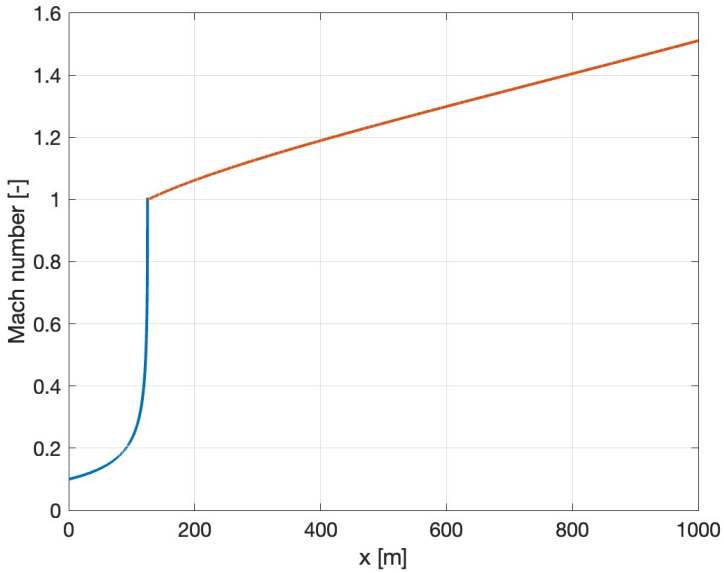

Figure 7.2: The simulated Mach number throughout the channel.

The calculated Mach number at the vent is 1.511. The speed of sound at the vent is 350.4 m/s (as seen in Figure 7.1b), which becomes 322.37 m/s with the aforementioned 8% reduction in local speed of sound due to the solid particles. The flow velocity at the vent is thus approximately 487 m/s, within the 350-950 m/s range. The Mach curve in the figure has a sharp edge because of the assumptions made, while in practice, it would have a more fluent, 'S'-like shape. What this means for Enceladus, and for the tested hypotheses, is discussed in the next section.

7.3. Implications considering the additional processes

The results of the experiments showed the effects of having a reservoir below the channel. When more heating power is supplied, the water temperature increases, which in turn increases the pressure in the reservoir. The higher reservoir pressure resulted in a higher mass flow rate, and a higher Mach number at the vent. Whether a reservoir is required or not depends on if the flow can reach the critical pressure ratio and create supersonic plumes without a reservoir. The results from the experiments and the simulation suggest that the effects of condensing vapor and friction are sufficient to choke the flow, and reach supersonic velocities when heat is removed from the flow in the supersonic region. It is therefore not necessary to have a pressurized reservoir to recreate the plumes, and hypothesis A is rejected. It does however not rule out the presence of a reservoir, because once the flow becomes choked, an increase in upstream pressure (in case of a reservoir) will not affect the downstream flow conditions. The experiments showed that the sonic point is downstream the geometrical throat, and with a higher upstream pressure (when more power is supplied), the sonic point shifts more towards the throat. In the absence of a geometrical throat, the effect of a higher upstream pressure on the sonic point is not clear. The larger pressure difference between the ocean and the vent would increase the initial acceleration of the flow, but the increase in velocity comes with a lower flow temperature and thus a higher saturation degree of the flow, so that condensation starts earlier in the channel. It is however certain that with a wide range of initial conditions for the simulation, the flow will become choked without a geometrical throat, with the condensing vapor being the main contributor to the increase in flow velocity. For that reason, hypothesis B is also rejected. But because of the natural formation of the channel, it would be inevitable that with a 1000 meter long channel, one or more narrower sections would be present. These narrow sections would assist in creating supersonic plumes, but are not required.

8

Conclusion and recommendations

This chapter is divided into two sections: the first being the conclusion of the results of the experiments and of the implications for Enceladus, answering the research questions (Section 8.1). And the second being the recommendations for future work, which are given in Section 8.2.

8.1. Conclusion

Now that the results of the experiments are analyzed in Chapter 6, and the implications for Enceladus are determined in Chapter 7, the research questions can be answered. The main research question is repeated below:

How can the thermodynamic processes and physical properties of an experimental setup be linked to the plumes of Enceladus?

The main research question is supported by subquestions, which are listed and answered below:

- **What is the effect of the geometry of a channel on plume formation?**

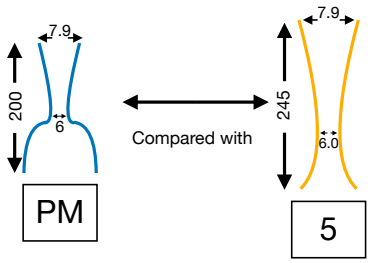

Figure 8.1: The tested models to determine the effects of an increase in channel length - plexiglass model and model 5.

First, the effect of an increase in channel length is considered. When model 5 is compared with the plexiglass model (see Figure 8.1), the throat to vent length increased by 45.8% and the total model length increased by 22.5%. It can be concluded that the increase in channel length resulted in a higher mass flow rate, and a higher (isentropic) Mach number. The increase in heating power results in an increase in reservoir temperature and pressure, and the increase in mass flow rate and Mach number becomes relatively larger when more heating power is supplied to the reservoir water. The cause of the difference in mass flow rate and (isentropic) Mach number at the vent between the models is likely because the channel has a longer expanding section where the flow can accelerate towards the vent, and that more heat is convected to the flow of model 5, as the reservoir and channel conditions show a behavior similar to having a narrower throat due to the heat addition. Also, when more heating power is supplied, the sonic point is shifted upstream, but is still downstream the geometrical throat. With more heating power, the increase in reservoir pressure is relatively larger than the increase in vacuum chamber pressure, as the latter also becomes slightly higher due to the increased mass flow rate. This larger relative difference in pressure results in a more steep decline in pressure (ratio) through the channel, which means that the critical pressure ratio is reached more upstream in the channel, and is the reason for the upstream shift in sonic point with increasing pressure.

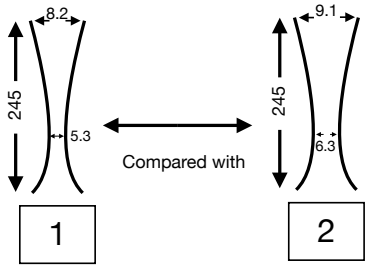

Figure 8.2: The tested models to determine the effects of an increase in channel diameter - model 1 and 2.

The effects of an increase in channel diameter is tested with a model with a 5.3 mm throat and a model with a 6.3 mm throat (see Figure 8.2), meaning an increase in throat area by 41.3%. The expansion angles are kept equal at approximately 0.9 deg, so the vent diameter increased proportionally. The increase in channel diameter decreases the (isentropic) Mach number, and increases the mass flow rate, where the magnitude of the increase and decrease becomes less when more heating power is supplied. Also here, the sonic point shifts upstream when more heating power is supplied, and even further upstream with a narrower channel but still downstream the geometrical throat. The described behavior of the mass flow rate, Mach number and sonic point, can be attributed to the higher reservoir pressure and temperature for the narrower channel, because the smaller throat area constricts the flow. The wider channel therefore has a more gradual decrease in pressure ratio, explaining the difference in results.

Figure 8.3: The tested straight channel - model 4.

The straight channel (see Figure 8.3) is used to measure the effects of friction (using the Fanno flow relations) and heat addition (using the Rayleigh flow relations). The influence of friction during the experiments is measurable. Although it is theoretically possible, it is unlikely that the flows of the experiments with the straight channel became choked due to friction alone. On the other hand, it is likely that the thermal heat radiated from the test section provides sufficient heat to thermally choke the flow when conducted through the model. The removal of the geometrical throat causes a large downstream shift in sonic point, so that the (theoretical) Mach number becomes exactly 1 at the exit (given sufficient upstream pressure, so that the flow becomes choked). The Mach number cannot exceed 1 in the vacuum chamber, as this would require heat removal from the flow while it is added during the experiments.

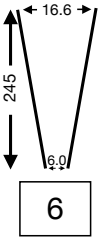

Figure 8.4: The tested diverging channel - model 6.

Lastly, when the expansion angle increases, flow separation occurs, which would require a large upstream pressure and low exit pressure to prevent this from occurring. Since the latter is fixed on Enceladus (a vacuum), it can be concluded that the reservoir conditions impose constraints on the maximum expansion angle of the channel. With an expansion angle of around 2.5 degrees (see Figure 8.4), flow separation occurs for all power settings used in this study, and all already within the first 6 cm of the channel. The flow separation causes an adverse pressure gradient at the channel walls, meaning that the local pressure is lower than the exit pressure, something that cannot occur on Enceladus. The largest possible throat-to-exit area ratio and expansion angle therefore depend mostly on the reservoir conditions, providing sufficient upstream pressure, and to a lesser extent the wall temperature.

- **Which heat exchanges occur along the flow and how do these affect the flow properties?**

  Starting from the reservoir water, heat is added by the heating foils, and to a small extent through convection from the plexiglass walls of the reservoir. When the pressure in the reservoir is sufficiently reduced, the reservoir water starts boiling and evaporating. This causes a temperature gradient inside the reservoir: the endothermic evaporation decreases the temperature above the water, and because of the lower temperature, the vapor becomes supersaturated and starts condensing in the upper reservoir, increasing the temperature there. The vapor then enters the inlet of the channel. The flow experiences the friction from the walls of the model, which generates negligible heat, and reduces the flow velocity in the vicinity of the wall, thereby creating a radial velocity gradient towards the center of the channel. When no heating power is supplied, relatively more heat is added to the flow from the environment since the flow acceleration is less after the channel expansion downstream the throat, giving more time to transfer. It is expected that heat is added to the flow due to a combination of two causes: first, the thermal radiation of the test section onto the model adds significant heat to the flow through conduction through the model

and convection at the walls. Second, it possible that the condensed vapor from the upper reservoir tends to evaporate again as the flow is unsaturated - the local pressure and temperature conditions imply a gaseous phase of the water molecules. The evaporation would locally (on a microscopic scale) cool the surface of the liquid particles, making them solid and releasing the remaining internal energy as heat. Given the local temperature and pressure conditions, the solid particles tend to sublimate, but the sublimation rate is too slow to have a noticeable effect in the channel. It is also demonstrated that when more heating power is added, the vent temperature decreases: the increase in mass flow actively cools the model, causing colder readings at the vent, also seen in Sklavenitis' study. Due to the heat increment in the channel, none of the models come close to reaching their design isentropic Mach number, and the deviations from the isentropic solutions are large.

- **What are the effects on the flow properties when the experimental setup is cooled?**

  First, cooling the model did not result in any significant changes in the reservoir conditions. There is also no consistent result on the effect on the sonic point, the isentropic Mach number and the mass flow rate. The pressure in the channel also did not change significantly. Cooling the model did however increase the saturation degree in the channel, because the saturation degree increases with decreasing temperature. The vapor will reach a metastable supersaturated state (only) in the reservoir. If the metastable limit is reached, condensation in the reservoir is instigated. For the plexiglass model, the section where condensation occurs becomes slightly extended, because the inlet of the plexiglass model is much wider than the other models, and basically acts as a small extension of the reservoir. This would theoretically shift the sonic point more downstream due to more latent heat release, but this could not be confirmed with the measurements. Since the saturation degree is well below 1 in the channel, cooling the model to the temperatures used in this study did not have an effect on condensation, nor the flow properties. To have a noticeable effect on the flow properties, the setup would have to be cooled to much lower temperatures, so that the flow starts condensing in the channel instead of the reservoir. For the plexiglass model, a decrease in temperature of around 10°C results in an increase in saturation degree of approximately 0.2, and the highest achieved saturation degree in the channel is 0.8. The experiments with the cooled model did query the method of measuring the temperature of the flow, as it is indicated that the temperature of the model and the environment has a significant effect on the temperature readings.

There would be many possible combinations of physical and thermodynamic properties that could recreate most of the plume characteristics of Enceladus inside a vacuum chamber. The model geometry and environmental conditions (including the vacuum chamber pressure) determine the flow properties, but the flow properties on Enceladus have so far only been estimated by CFD models involving assumptions. It is however not expected that a pressurized reservoir is necessary to create the plumes on Enceladus, nor is the presence of a geometrical throat. But despite them not being a necessity to recreate the plume characteristics, their presence or absence on Enceladus cannot be confirmed with these results alone. A follow-up study could shed a light on the problems encountered in this study, and will be detailed in the recommendations section (Section 8.2).

8.2. Recommendations for future work

Based on the results of the experiments in this study, the recommendations for future research on this topic would include:

- A new design for a long, straight channel where the water level is inside the channel (without a reservoir). This has been attempted by using model 3 with the reservoir from Sklavenitis' study, but a separate design with an integrated water supply in the model might be required. A possible solution for the setup used in this study (model 3 and the reservoir) would be: a wider channel for more airflow during evacuation, or a hole in the reservoir with also a (one-way) check valve to get rid of the excess reservoir pressure. It seems that an additional hole in the reservoir with a check valve is a requirement for when the pressure is reduced to the point where the water starts boiling and pressure starts increasing in the reservoir, or else the excess pressure will leave through the channel again making the measurements not accurate. The model with the

check valve connected to the channel has been designed such that no hole had to be made in the reservoir, but it turned out that this is necessary to get accurate measurements.

- Another interesting experiment would be where the entire reservoir is heated, so not just the water at the bottom of the reservoir. The heated reservoir would mitigate the effects of the evaporative cooling at the liquid-gas interface when boiling, and would prevent the vapor from already condensing in the reservoir. If the model on top of the reservoir is not cooled, it is likely that there would be no condensation at all, but the results would be more comparable to the results from the CFD model in Section 6.8, where vapor did not already partially condense at the inlet.
- Following on from the previous point, cooling the model walls to temperatures much lower than used in this study would give insight into nucleation and condensation processes inside the channel. To reach the extremely low temperatures on Enceladus, a custom made model could be cooled by using liquid nitrogen. This would make the flow supersaturated in the channel, something that is also expected on Enceladus. Measuring the temperatures and pressure of the flow would be more difficult with these temperatures.
- Since the measuring location of the temperature sensor significantly affects the readings, it is recommended to review the measurement method. There are signs of large radial temperature gradients in the flow, so it is difficult to find a way to accurately measure the flow temperature. Measuring the temperature close to the wall would increase the influence of the heat from the wall itself, and measuring the temperature in the center of the channel would obstruct the flow and produce more inconsistent results.
- It is expected that the heat radiated from the test section is sufficient to thermally choke the flow. To verify this, one could measure the magnitude of the radiation by conducting experiments in an empty chamber, under varying conditions (mainly room temperature). Or to insulate the model, so that it is shielded from the thermal radiation. If this influence can be quantified, the heat increase in the channel could be attributed to only the heat generated inside the channel due to thermodynamic processes.
- Lastly, it would be interesting to observe the flow properties and the exit Mach number in a vacuum chamber with a lower pressure. In the current setup, the flow expansion is limited by the relatively high pressure in the chamber. A lower chamber pressure would shift the sonic point upstream, closer to the geometrical throat. Simulations with the CFD model showed that with a 'free expansion' - or when the far-field pressure is a full vacuum - the pressure at the vent is about half the pressure measured during the experiments. The lower exit pressure would shift the pressure (ratio) downwards after the throat, where it would then resemble the results for the pressure curves from the CFD simulation.

References

[1] NASA. *An Ice World...With an Ocean?* 2017. URL: https://www.nasa.gov/feature/jpl/an-ice-worldwith-an-ocean (visited on 01/03/2023).

[2] M.K. Dougherty et al. “Identification of a Dynamic Atmosphere at Enceladus with the Cassini Magnetometer”. In: *Science* 311 (2006), pp. 1406–1409. DOI: 10.1126/science.1120985.

[3] Valeriy Tenishev et al. “Effect of the Tiger Stripes on the water vapor distribution in Enceladus’ exosphere”. In: *Journal of Geophysical Research: Planets* 119.12 (2014), pp. 2658–2667. DOI: https://doi.org/10.1002/2014JE004700. eprint: https://agupubs.onlinelibrary.wiley.com/doi/pdf/10.1002/2014JE004700.

[4] M.K. Dougherty and L.J. Spilker. “Review of Saturn’s icy moons following the Cassini mission.” In: *Reports on Progress in Physics* 81.6 (2018). DOI: 10.1088/1361-6633/aabdfb.

[5] David Deamer and Bruce Damer. “Can Life Begin on Enceladus? A Perspective from Hydrothermal Chemistry”. In: *Astrobiology* 17.9 (2017). PMID: 28682665, pp. 834–839. DOI: 10.1089/ast.2016.1610.

[6] The Messier Catalog. *Friedrich Wilhelm (William) Herschel (November 15, 1738 - August 25, 1822)*. URL: http://www.messier.seds.org/xtra/Bios/wherschel.html (visited on 01/03/2023).

[7] Paul M. Schenk et al. *Enceladus and the Icy Moons of Saturn*. The University of Arizona Press, 2018.

[8] NASA. *Cassini mission*. URL: https://solarsystem.nasa.gov/missions/cassini/overview/ (visited on 01/03/2023).

[9] Jack J. Lissauer and Imke de Pater. *Fundamental Planetary Science*. Updated edition. Cambridge University Press, 2019.

[10] Ali Sulaiman et al. “Enceladus and Titan: Emerging Worlds of the Solar System (ESA Voyage 2050 White Paper)”. In: (Aug. 2019).

[11] Candice J. Hansen et al. “Enceladus’ Water Vapor Plume”. In: *Science* 311 (2006), p. 1422. DOI: 10.1126/science.1121254.

[12] C. J. Hansen et al. “The composition and structure of Enceladus’ plume from the complete set of Cassini UVIS occultation observations.” In: *Icarus* 113461 (2019). DOI: 10.1016/j.icarus.2019.113461.

[13] John R. Spencer and Francis Nimmo. “Enceladus: An Active Ice World in the Saturn System”. In: *The Annual Review of Earth and Planetary Sciences* 41 (2013), pp. 693–717. DOI: 10.1146/annurev-earth-050212-124025.

[14] NASA. *Jet spots in tiger stripes*. 2008. URL: https://solarsystem.nasa.gov/resources/14013/jet-spots-in-tiger-stripes/ (visited on 01/03/2023).

[15] Robert H. Brown et al. “Composition and Physical Properties of Enceladus’ Surface”. In: *Science* 311 (2006), p. 1425. DOI: 10.1126/science.1121031.

[16] F. Postberg et al. “Plume and Surface Composition of Enceladus”. In: *Enceladus and the Icy Moons of Saturn* (2018), pp. 129–162. DOI: 10.2458/azu_uapress_9780816537075-ch007.

[17] Gianrico Filacchione et al. “Saturn’s icy satellites investigated by Cassini-VIMS. IV. Daytime temperature maps”. In: *Icarus* 271 (June 2016), pp. 292–313. DOI: 10.1016/j.icarus.2016.02.019. arXiv: 1602.02890 [astro-ph.EP].

[18] F. Postberg et al. “The salty spray of Enceladus - Implications for the plume formation”. In: *EPSC-DPS Joint Meeting 2011*. Vol. 2011. Oct. 2011, p. 642.

[19] J. R. Spencer et al. “Plume Origins and Plumbing: From Ocean to Surface”. In: *Enceladus and the Icy Moons of Saturn*. Ed. by Paul M. Schenk et al. 2018, p. 163. DOI: 10.2458/azu_uapress_9780816537075-ch008.

[20] Edwin S. Kite and Allan M. Rubin. “Sustained eruptions on Enceladus explained by turbulent dissipation in tiger stripes”. In: *Proceedings of the National Academy of Science* 113.15 (Apr. 2016), pp. 3972–3975. DOI: 10.1073/pnas.1520507113. arXiv: 1606.00026 [astro-ph.EP].

[21] Carolyn Porco, Daiana DiNino, and Francis Nimmo. “How the Geysers, Tidal Stresses, and Thermal Emission across the South Polar Terrain of Enceladus are Related”. In: *The Astronomical Journal* 148.3, 45 (Sept. 2014), p. 45. DOI: 10.1088/0004-6256/148/3/45.

[22] Dennis L. Matson et al. “Enceladus: A hypothesis for bringing both heat and chemicals to the surface”. In: *Icarus* 221.1 (Sept. 2012), pp. 53–62. DOI: 10.1016/j.icarus.2012.05.031.

[23] G. D. Crawford and D. J. Stevenson. “Gas-driven water volcanism and the resurfacing of Europa”. In: *Icarus* 73.1 (Jan. 1988), pp. 66–79. DOI: 10.1016/0019-1035(88)90085-1.

[24] Adam P. Showman, Ignacio Mosqueira, and James W. Head. “On the resurfacing of Ganymede by liquid water volcanism”. In: *Icarus* 172.2 (Dec. 2004), pp. 625–640. DOI: 10.1016/j.icarus.2004.07.011.

[25] M. Manga and C. -Y. Wang. “Pressurized oceans and the eruption of liquid water on Europa and Enceladus”. In: *Geophysical Research Letters* 34.7, L07202 (Apr. 2007), p. L07202. DOI: 10.1029/2007GL029297.

[26] Dennis L. Matson et al. “Enceladus’ near-surface CO_2 gas pockets and surface frost deposits”. In: *Icarus* 302 (Mar. 2018), pp. 18–26. DOI: 10.1016/j.icarus.2017.10.025.

[27] F. Postberg et al. “Sodium salts in E-ring ice grains from an ocean below the surface of Enceladus.” In: *Nature* 459.7250 (2009), pp. 1098–1101. DOI: 10.1038/nature08046.

[28] F. Postberg et al. “A salt-water reservoir as the source of a compositionally stratified plume on Enceladus.” In: *Nature* 474.7353 (2011), pp. 620–622. DOI: 10.1038/nature10175.

[29] Miki Nakajima and Andrew P. Ingersoll. “Controlled boiling on Enceladus. 1. Model of the vapor-driven jets”. In: *Icarus* 272 (July 2016), pp. 309–318. DOI: 10.1016/j.icarus.2016.02.027.

[30] Andrew P. Ingersoll and Miki Nakajima. “Controlled boiling on Enceladus. 2. Model of the liquid-filled cracks”. In: *Icarus* 272 (July 2016), pp. 319–326. DOI: 10.1016/j.icarus.2015.12.040.

[31] N Khawaja et al. “Low-mass nitrogen-, oxygen-bearing, and aromatic compounds in Enceladean ice grains”. In: *Monthly Notices of the Royal Astronomical Society* 489.4 (Oct. 2019), pp. 5231–5243. ISSN: 0035-8711. DOI: 10.1093/mnras/stz2280. eprint: https://academic.oup.com/mnras/article-pdf/489/4/5231/32452195/stz2280.pdf. URL: https://doi.org/10.1093/mnras/stz2280.

[32] S. Colette Daubner and Paul F. Fitzpatrick. “Pteridines”. In: *Encyclopedia of Biological Chemistry*. Ed. by William J. Lennarz and M. Daniel Lane. New York: Elsevier, 2004, pp. 556–560. ISBN: 978-0-12-443710-4. DOI: https://doi.org/10.1016/B0-12-443710-9/00559-7. URL: https://www.sciencedirect.com/science/article/pii/B0124437109005597.

[33] W. B. McKinnon et al. “The Mysterious Origin of Enceladus: A Compositional Perspective”. In: *Enceladus and the Icy Moons of Saturn*. Ed. by Paul M. Schenk et al. 2018, pp. 17–38. DOI: 10.2458/azu_uapress_9780816537075-ch002.

[34] Susan Kieffer et al. “Ice/Vapor Ratio of Enceladus’ Plume: Implications for Sublimation”. In: *Icarus* 203 (Mar. 2009), pp. 238–241.

[35] Andrew P. Ingersoll, Shawn P. Ewald, and Samantha K. Trumbo. “Time variability of the Enceladus plumes: Orbital periods, decadal periods, and aperiodic change”. In: *Icarus* 344, 113345 (July 2020), p. 113345. DOI: 10.1016/j.icarus.2019.06.006.

[36] D. B. Goldstein et al. “Enceladus Plume Dynamics: From Surface to Space”. In: *Enceladus and the Icy Moons of Saturn*. Ed. by Paul M. Schenk et al. 2018, p. 175. DOI: 10.2458/azu_uapress_9780816537075-ch009.

[37] Ben D. Teolis et al. “Enceladus Plume Structure and Time Variability: Comparison of Cassini Observations”. In: *Astrobiology* 17.9 (2017), pp. 926–940. DOI: http://doi.org/10.1089/ast.2017.1647.

[38] W.J. Devenport. *Nozzle Applet*. 2001. URL: https://www.engapplets.vt.edu/fluids/CDnozzle/cdinfo.html (visited on 01/05/2023).

[39] Yunus A. Cengel and Michael A. Boles. *Thermodynamics - an engineering approach*. 5th ed. Tata McGraw-Hill, 2006.

[40] Jürgen Schmidt et al. “Slow dust in Enceladus’ plume from condensation and wall collisions in tiger stripe fractures”. In: *Nature* 451.7179 (Feb. 2008), pp. 685–688. DOI: 10.1038/nature06491.

[41] K. Matsuo et al. “Studies of Condensation Shock Waves: 2nd Report, Relation between Condensation Shock Wave and Condensation Zone.” In: *Bulletin of JSME* 29.248 (1986), pp. 439–443. DOI: 10.1299/jsme1958.29.439.

[42] P. P. Wegener. “Condensation Phenomena in Nozzles.” In: *Progress in Astronautics and Rocketry* (1964), pp. 701–724. DOI: 10.1016/b978-1-4832-2730-6.50033-6.

[43] John D. Anderson. *Fundamentals of Aerodynamics*. 6th ed. 2 Penn Plaza, New York, NY10121: McGraw-Hill, 2017.

[44] John D. Anderson Jr. *Modern Compressible Flow - With Historical Perspective*. 3rd ed. McGraw-Hill, 2003.

[45] N.J. van der Hijden, F.F.J Schrijer, and S.M. Cazaux. “Linking Enceladus’ plume characteristics to the crevasse properties”. MSc thesis. TU Delft Aerospace Engineering, Dec. 2021.

[46] E.M. Greitzer, C.S. Tan, and M.B. Graf. *Internal Flow - Concepts and Applications*. 1st ed. Cambridge University Press, 2004.

[47] S. Sklavenitis. “Experimental simulation and assessment of the geysers of icy moons in the laboratory”. MSc thesis. TU Delft Aerospace Engineering, Feb. 2022.

[48] J. Palmer, K. Ramsden, and E. Goodger. *Compressible Flow Tables for Engineers*. 1st ed. Macmillan Education Ltd, 1987.

[49] M.K. Goodrich et al. “Aeronautical wind tunnels - Europa and Asia”. In: *Federal Research Division - Library of Congress* (2006). https://apps.dtic.mil/sti/pdfs/ADA484099.pdf.

[50] T.J. Becx. “Icy moon plume simulator chamber”. MSc thesis. TU Delft Aerospace Engineering, Feb. 2019.

[51] Seng Keat Yeoh et al. “Constraining the Enceladus plume using numerical simulation and Cassini data”. In: *Icarus* 281 (Jan. 2017), pp. 357–378. DOI: 10.1016/j.icarus.2016.08.028.

[52] A.A. Pouring. “Thermal Choking and Condensation in Nozzles”. In: *Physics of Fluids* 8.10 (1965), p. 1802. DOI: 10.1063/1.1761112.

[53] V. Babu. *Fundamentals of Gas Dynamics*. 2nd ed. Springer, 2021.

[54] J.S. Hahn and R.G. Lutz. “Experimental Investigation Of Turbulent Boundary Layers With Pressure Gradient And Heat Transfer At Mach Number 4”. In: *Arnold Engineering Development Center* (1971).

[55] A. Mills. “The coefficient of friction, particularly of ice.” In: *Physics Education* 43.4 (2008), pp. 392–395. DOI: 10.1088/0031-9120/43/4/006.

Appendix A

Wiring diagram and documentation of measuring equipment

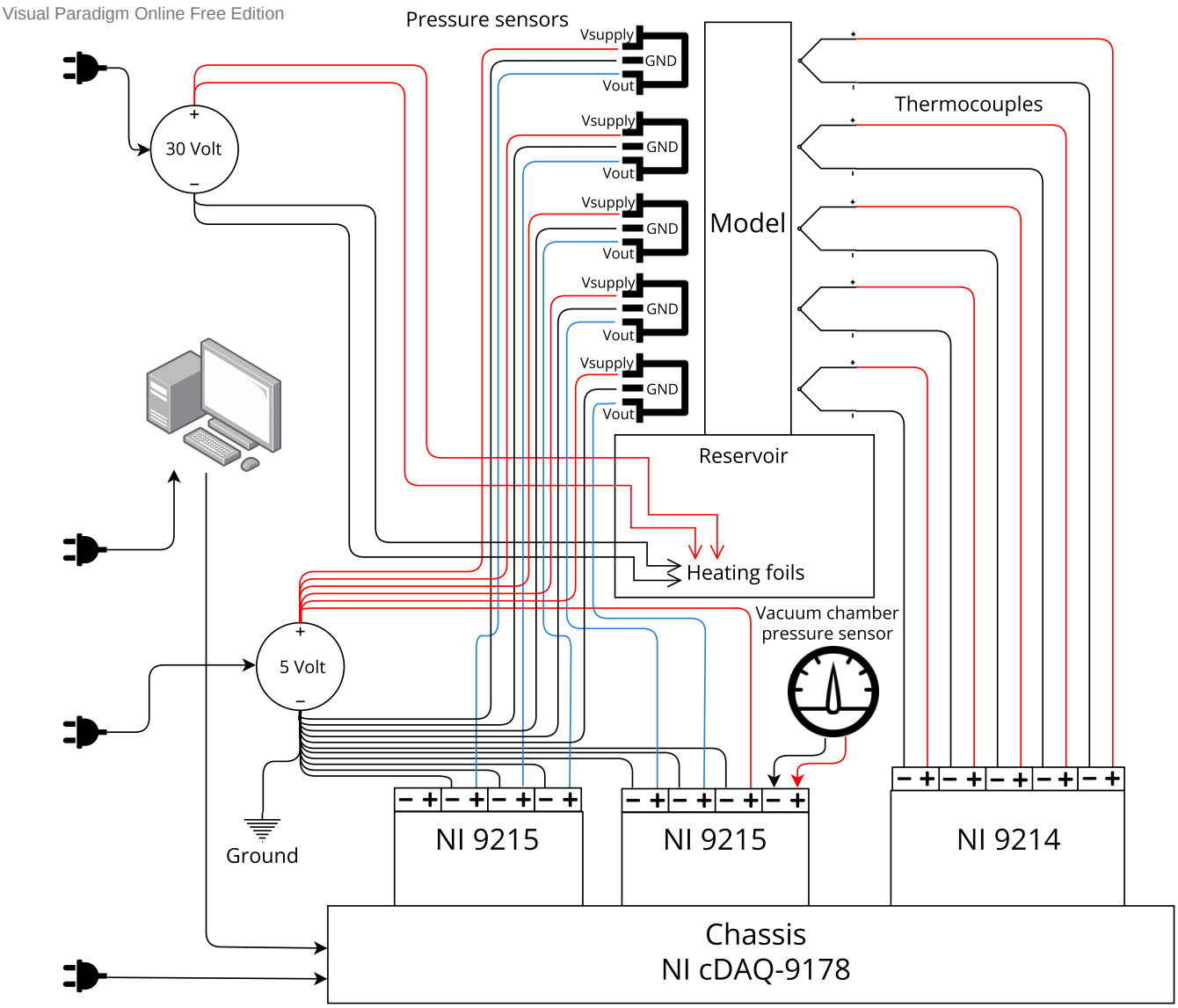

Chassis: National instruments cDAQ-9178

- Product page: `https://www.ni.com/nl-nl/support/model.cdaq-9178.html`
- Specs: `https://www.ni.com/docs/en-US/bundle/cdaq-9178-specs/page/specs.html`

Thermocouple module: National instruments 9214

- Product page: `https://www.ni.com/nl-nl/support/model.ni-9214.html`
- Specs:`https://www.ni.com/docs/en-US/bundle/ni-9214-specs/page/specifications.html`

Pressure sensor module(s): National instruments 9215 (analog input & BNC input)

- Product page: `https://www.ni.com/nl-nl/support/model.ni-9215.html`
- Specs: `https://www.ni.com/docs/en-US/bundle/ni-9215-specs/page/specs.html`

Appendix B

Technical drawing of the plexiglass model

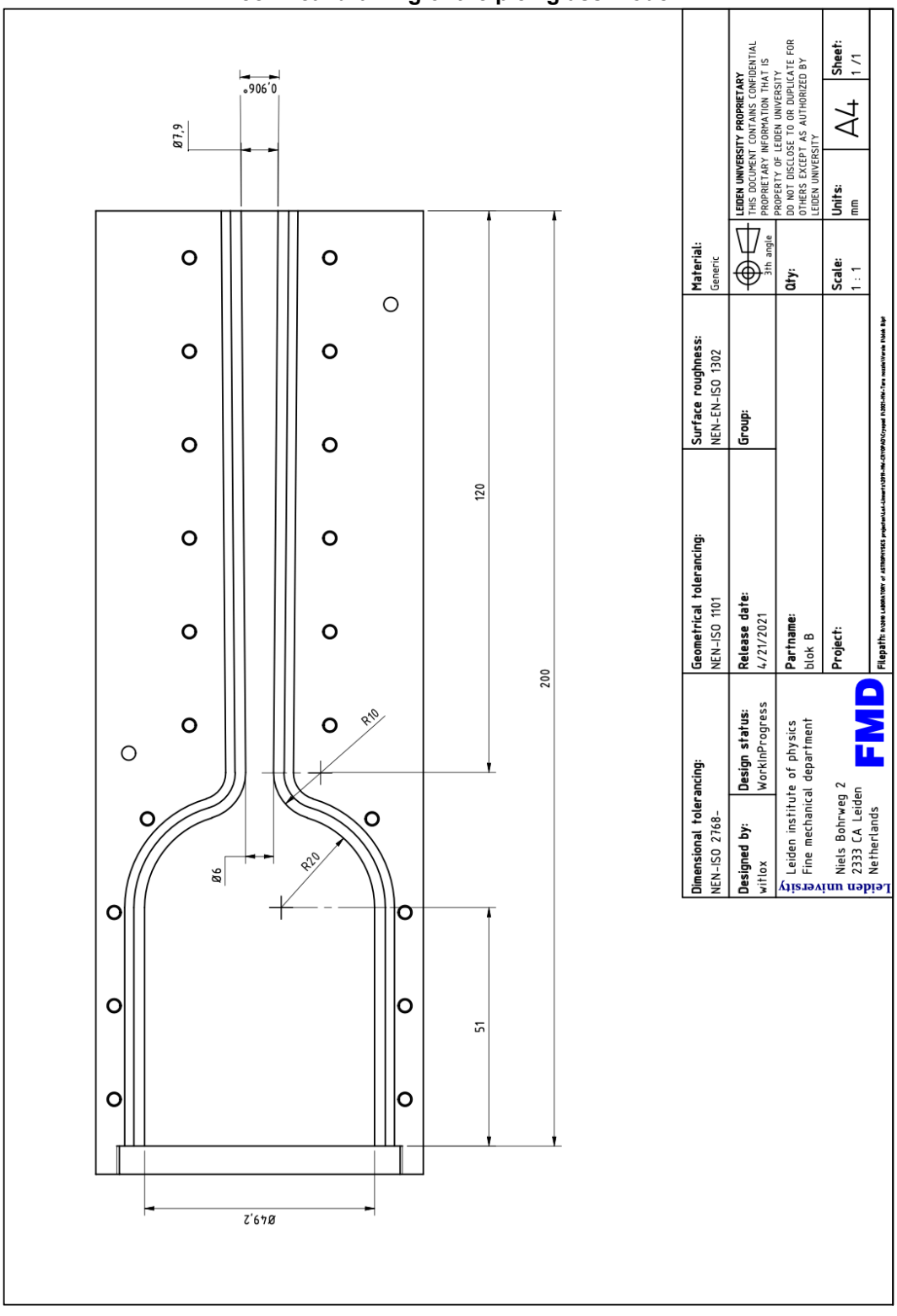

Appendix C

Technical drawing of model 4 - the channel differs per model

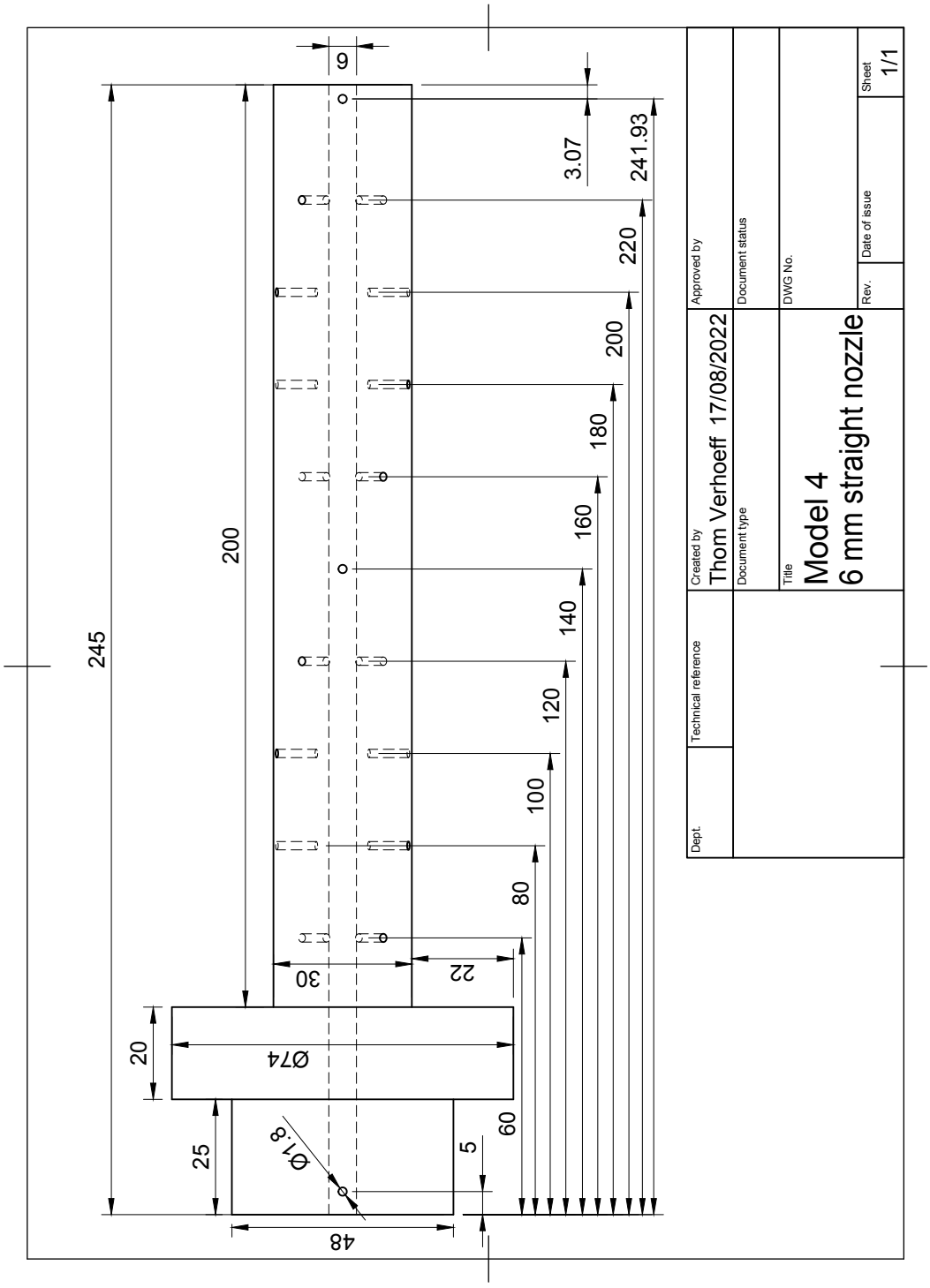

Appendix D

Technical drawing of the reservoir

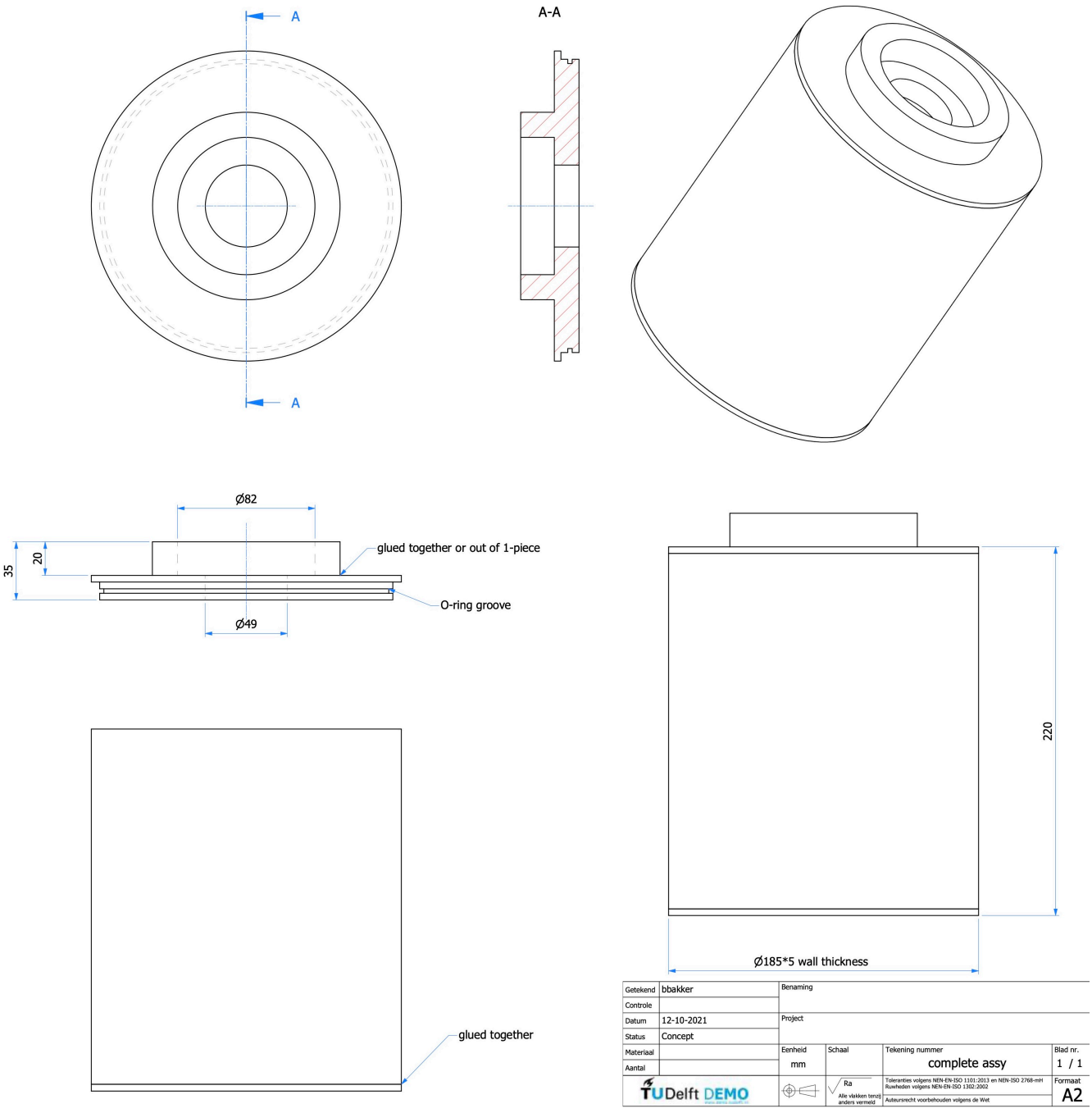

Appendix E

The temperature and pressure plots of the models can be seen on the pages below. These graphs are provided for each model, and are used to compare the models used in this study, together with the plots shown in the results section. This representation makes it easier to identify the proportions/ratios of the pressures and temperatures, and can be used to spot irregularities. The red numbers indicate the locations of the measurement points, and the dashed line indicates the location of the throat. The channels are all plotted as a straight channel to improve readability.

Plexiglass model. Full, half and no power settings at t = ± 25 min.

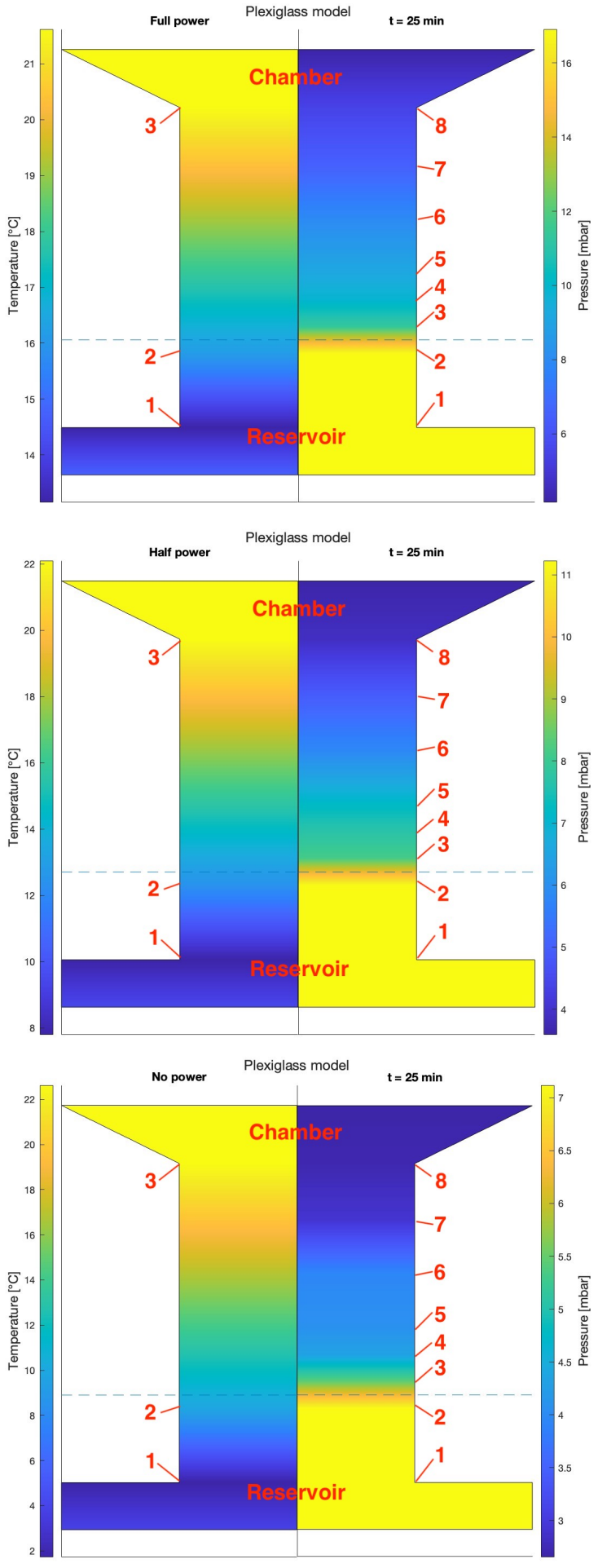

Cooled plexiglass model. Full and half power settings at t = ± 25 min.

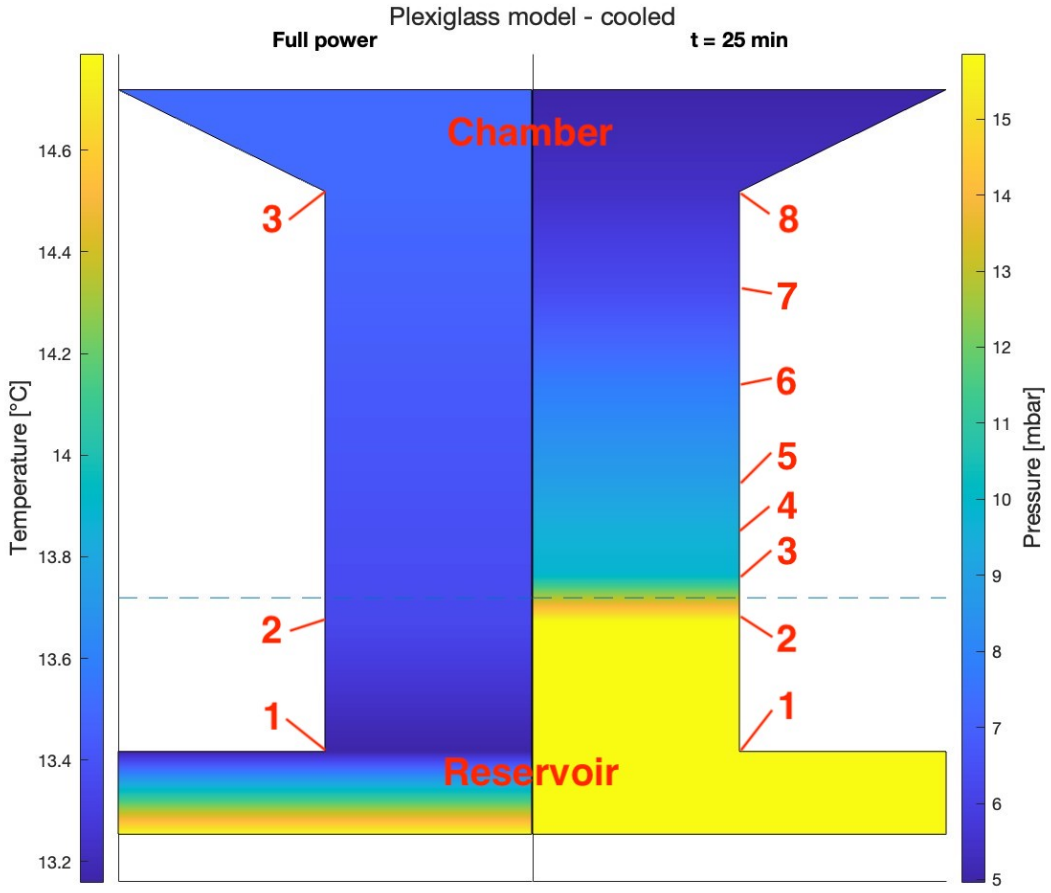

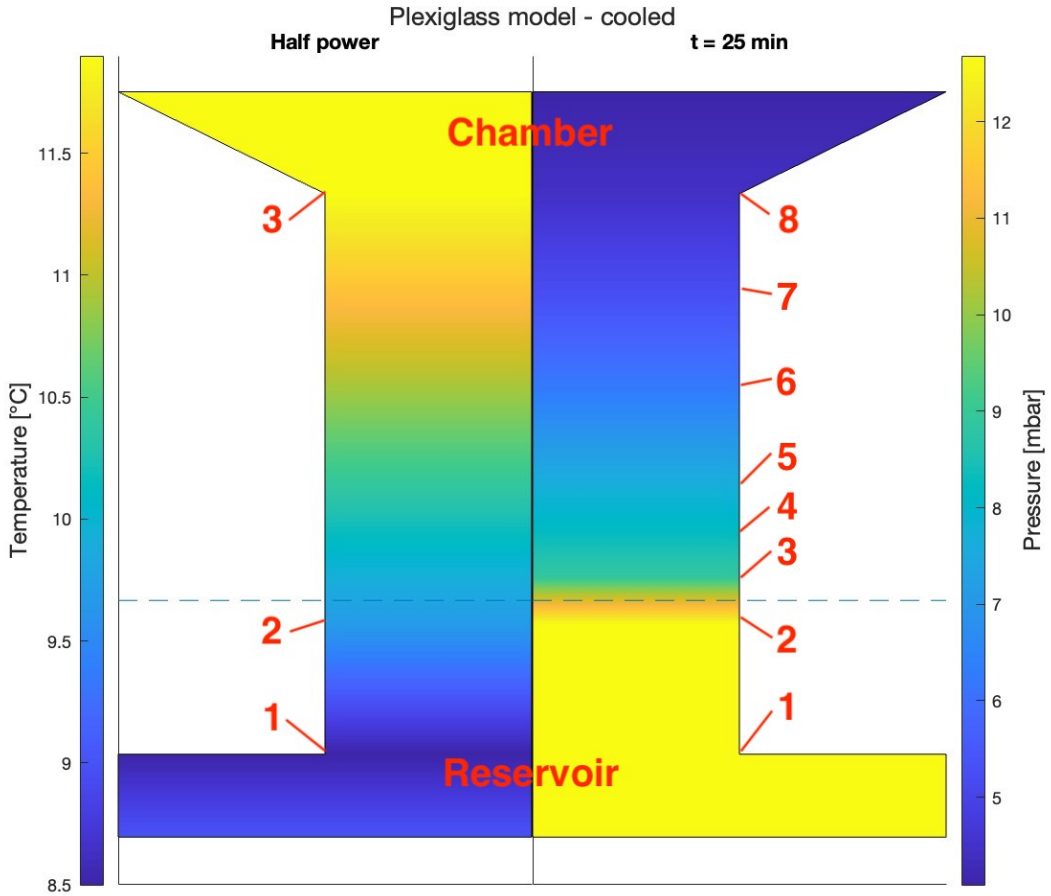

Model 1 - narrower converging-diverging channel.
Full, half and no power settings at t = ± 25 min.

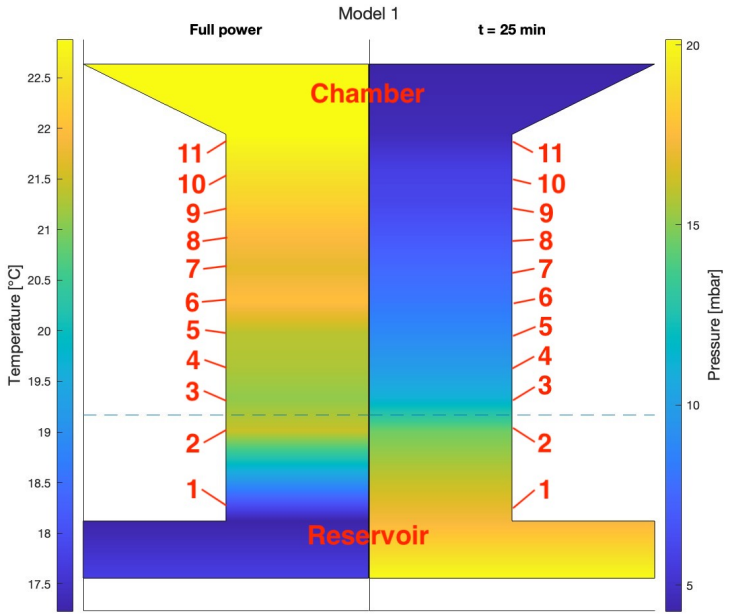

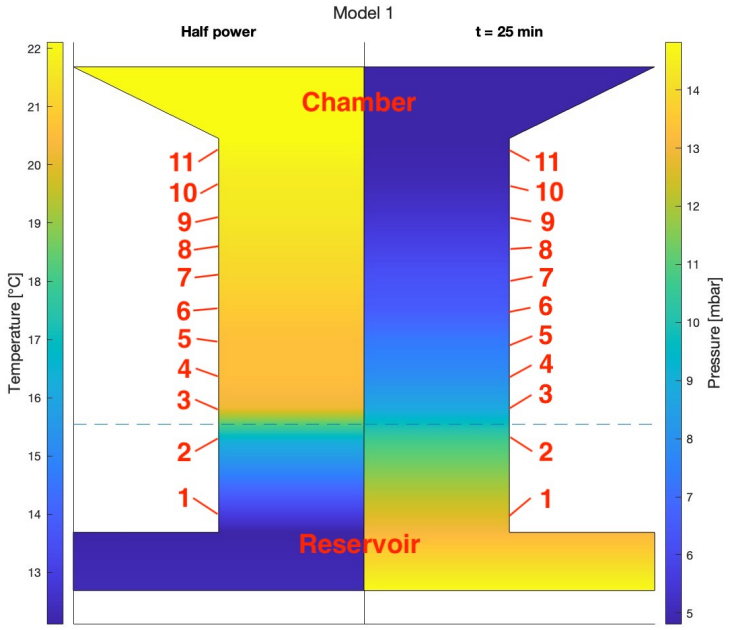

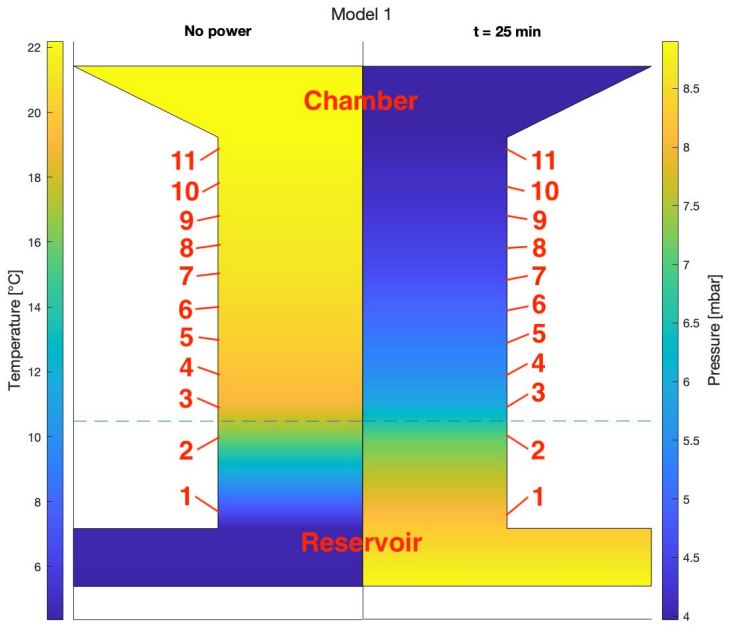

Model 2 - wider converging-diverging channel.
Full, half and no power settings at t = ± 25 min.

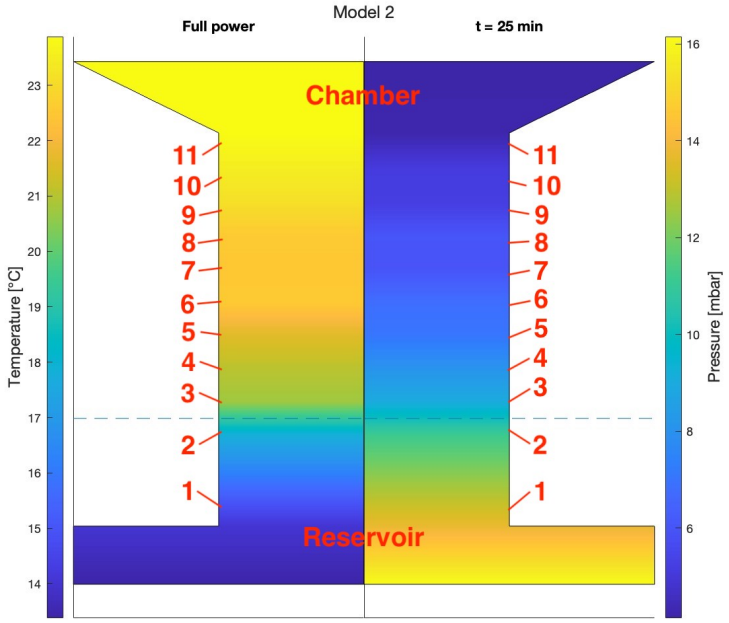

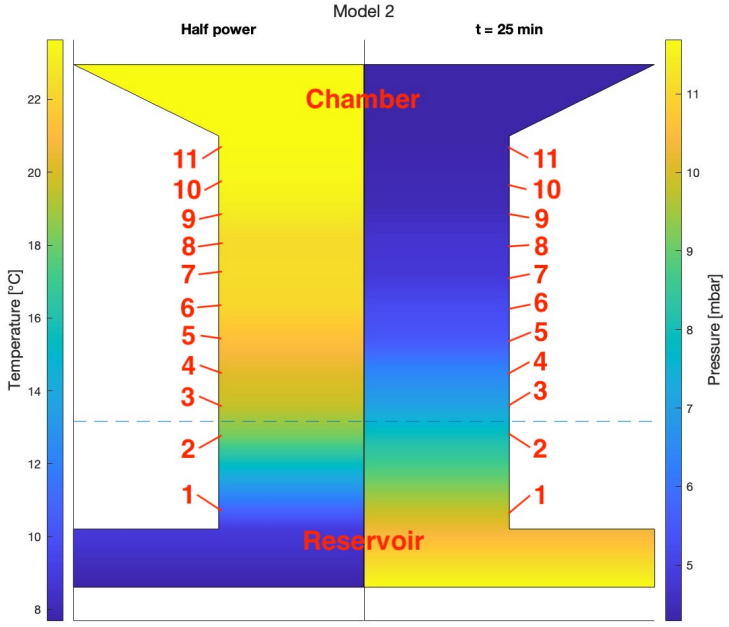

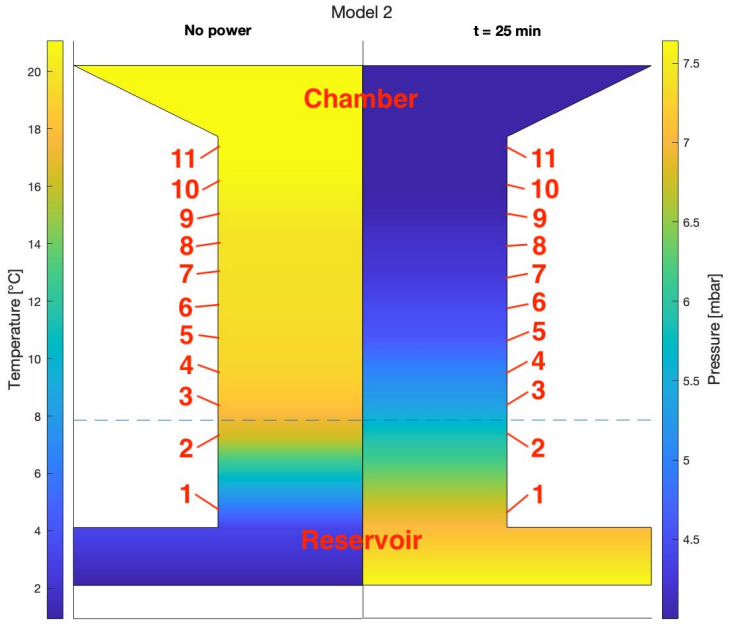

Model 4 - straight channel. Full, half and no power settings at t = ± 25 min.

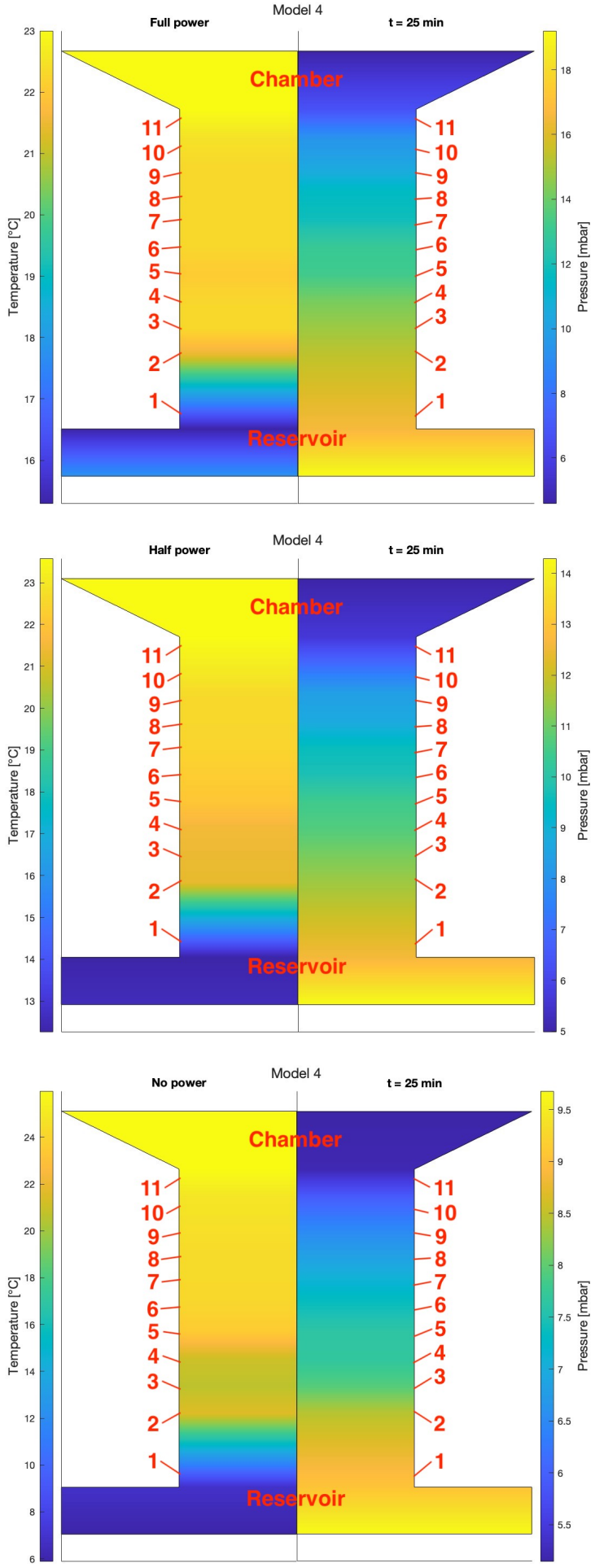

Model 5 - increased channel length, different material.
Full, half and no power settings at t = ± 25 min.

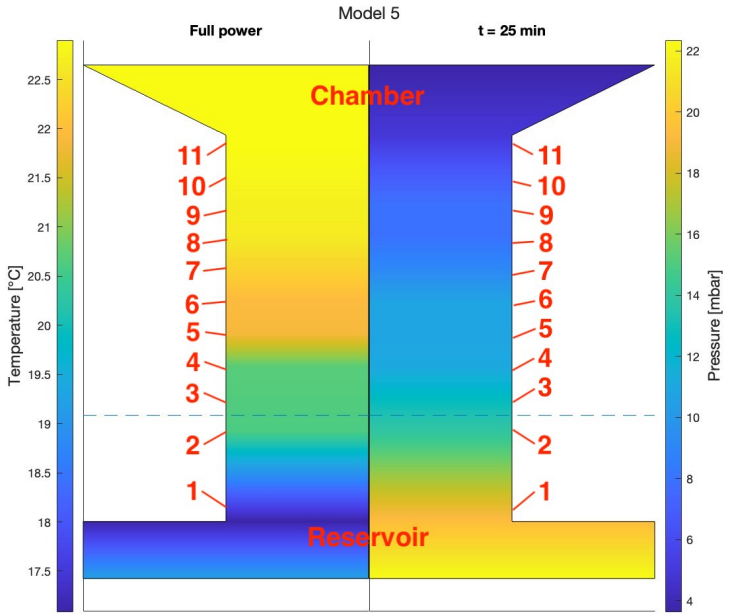

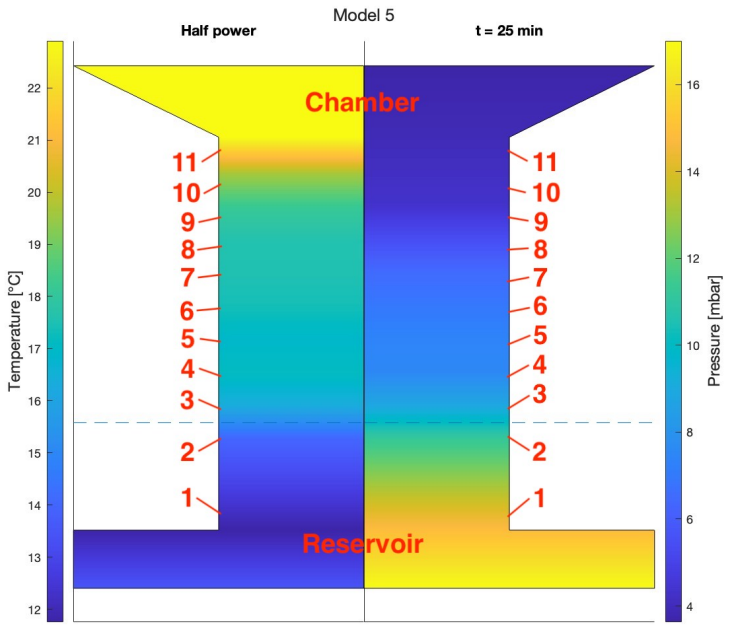

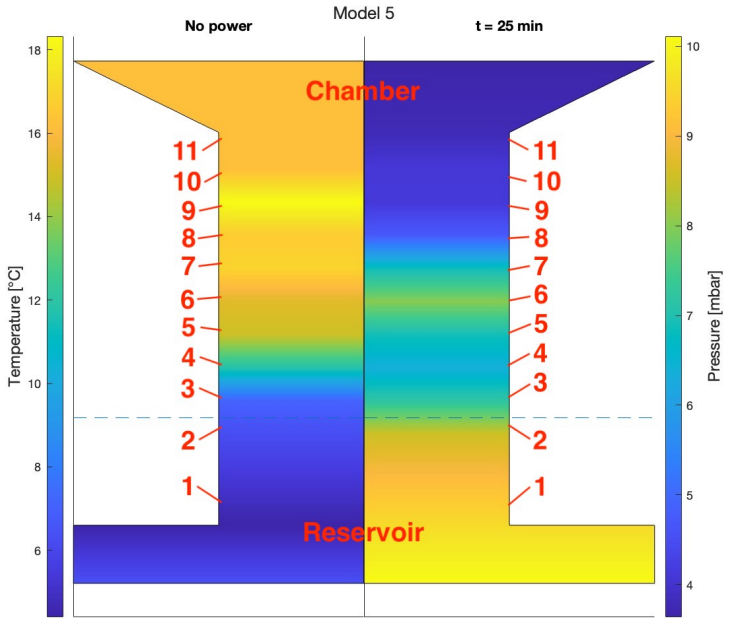

Cooled model 5 - increased channel length, different material. Half power setting at t = ± 25 min.

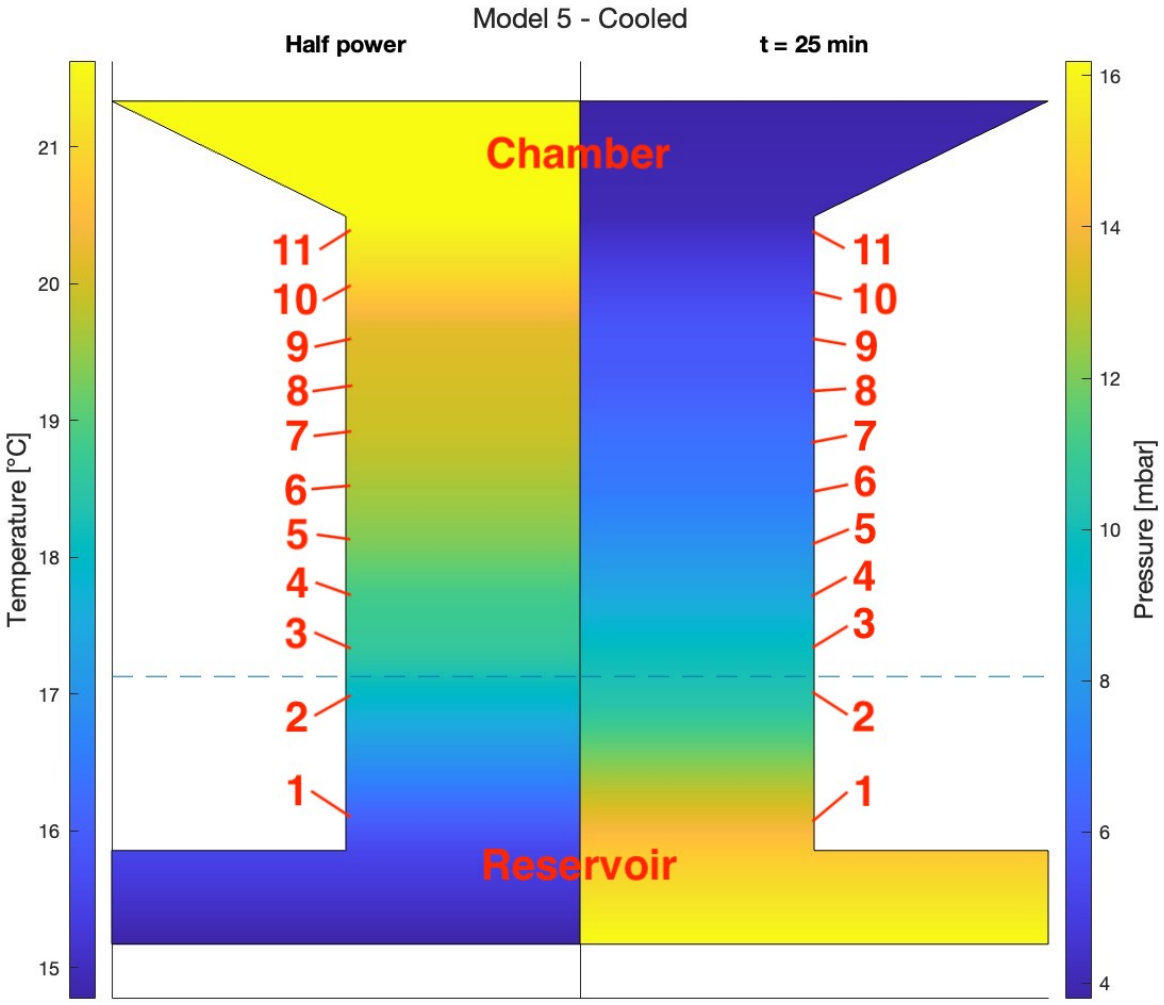

Model 6 - diverging channel.
Full, half and no power settings at t = ± 25 min.